Dissertation

submitted to the

Combined Faculties for the Natural Sciences and for

Mathematics

of the Ruperto-Carola University of Heidelberg, Germany

for the degree of

Doctor of Natural Sciences

presented by

Dipl.-Phys. Svenja Carrigan

born in Dortmund, Germany

Oral examination: 25 July 2007

Pulsar Wind Nebulae with H.E.S.S.:

Establishing a Connection between high-power Pulsars and very-high-energy gamma-ray Sources

Referees: Prof. Dr. Werner Hofmann

Prof. Dr. Thomas Lohse

Abstract

Pulsars energise particles into lighthouse pencil beams and create extended relativistic outflows, pulsar wind nebulae (PWNe). In the very-high-energy (VHE) gamma-ray wave band, these PWNe represent to date the most populous class of Galactic sources. Nevertheless, the details of the energy conversion mechanisms in the vicinity of pulsars are not well understood, nor is it known which pulsars are able to drive PWNe and emit high-energy radiation. Due to its large field of view and unprecedented sensitivity, H.E.S.S. is the first instrument to allow for deep surveys of the Galactic plane in VHE gamma rays. This work presents the first ever systematic investigation of the connection of VHE gamma-ray sources and PWNe. Besides presenting two new candidate PWNe detected in this search, it is shown that pulsars with large spin-down energy flux are indeed with high probability associated with VHE gamma-ray sources, implying the existence of an efficient mechanism by which a large fraction of pulsar spin-down energy is converted into kinetic energy of particles. The results presented here make it very likely that future more sensitive VHE gamma-ray instruments will detect a rapidly increasing number of lower-luminosity PWNe.

Kurzfassung

Wie kosmische Leuchttürme strahlen Pulsare energiegeladene Teilchen entlang ihrer Magnetfeldachsen ab und erzeugen ausgedehnte relativistische Pulsar-Wind-Nebel (PWN). Im Wellenlängenbereich der sehr hochenergetischen Gamma-Strahlung sind PWN momentan die zahlenmäßig dominante Klasse galaktischer Quellen. Trotzdem sind die Mechanismen der Energieumwandlung in Pulsaren schlecht verstanden und es ist nicht bekannt, welche Pulsare PWN und sehr hochenergetische Strahlung erzeugen können. Aufgrund des großen Gesichtsfelds und der beispiellosen Sensitivität ist H.E.S.S. das erste Experiment, für welches eine Durchmusterung über große Bereiche der galaktischen Ebene im Bereich sehr hochenergetischer Gamma-Strahlung möglich ist. Diese Arbeit berichtet von der ersten systematischen Erforschung des Zusammenhangs zwischen Quellen sehr hochenergetischer Gamma-Strahlung und PWN. Neben der Präsentation zweier neuer PWN Kandidaten, die im Rahmen dieser Suche gefunden wurden, wird gezeigt, daß Pulsare mit hohem Spin-Down-Energiefluß tatsächlich mit hoher Wahrscheinlichkeit mit Quellen sehr hochenergetischer Gamma-Strahlung verbunden sind. Das setzt die Existenz eines effizienten Mechanismus voraus, der einen großen Teil der Spin-Down-Energie des Pulsars in kinetische Energie von Teilchen umwandelt. Diese Ergebnisse suggerieren, daß zukünftige, sensitivere Instrumente zur Detektion sehr hochenergetischer Gamma-Strahlung eine rasch anwachsende Zahl PWN niedrigerer Luminosität entdecken werden.

Contents

List of Figures

List of Tables

Chapter 1

Introduction

Very-high-energy (VHE, above 10^{11} eV) γ-rays provide a unique view of the "non-thermal" universe, tracing the most violent and energetic phenomena at work inside our galaxy and beyond. They offer information about objects such as active galaxies, pulsars and supernova remnants, which act like giant particle accelerators in space, accelerating charged particles that are the progenitors of the VHE γ-rays to energies beyond those achievable in man-made accelerators. VHE γ-rays are also an important tool in the search for the origin of cosmic rays, as they are secondary products of cosmic-ray interactions with ambient matter. Being of neutral charge, VHE γ-rays do not get deflected by the galactic and extra-galactic magnetic fields and thus allow to trace back to their source. VHE γ-rays therefore offer insight into some of the most extreme regions of our universe.

As VHE γ-rays are rare – on the order of one γ-ray a year in an area of 1 m^2 – a satellite built to detect such VHE γ-rays would have to be very large indeed to detect any at all (and would be extremely expensive). The great advantage of the ground-based Imaging Atmospheric Cherenkov Technique is that the atmosphere forms an integral part of the detector, which makes the detection area of a Cherenkov telescope very large.

The High Energy Stereoscopic System (H.E.S.S.) is to date the most sensitive instrument for VHE γ-ray astronomy and is at the forefront of research in this area. Due to its large field of view in combination with its unprecedented sensitivity, it is the first instrument to allow for deep surveys of the Galactic plane in VHE γ-rays. Before these surveys, only few VHE γ-ray sources had been known in our Galaxy.

H.E.S.S. has discovered a large number of VHE γ-ray sources in these surveys. Of these, a significant quantity can be identified as pulsar wind nebulae (PWNe), the extended relativistic outflows of pulsars. These PWNe are seen across the electromagnetic spectrum in synchrotron and inverse-Compton emission. Due to the formation of strong shocks, particles can be accelerated to $\sim$PeV (10^{15} eV) energies within these nebulae.

Discovered in 1989 as the first celestial source of VHE γ-radiation, the best studied example of a PWN is the Crab nebula, which exhibits strong non-thermal emission across most of the electromagnetic spectrum from radio to >50 TeV γ-rays (Hillas et al., 1998; Tanimori et al., 1998; Aharonian et al., 2004a, 2006c). Prominent examples of recently discovered PWNe are the PWN of the energetic pulsar PSR B1509−58 in the supernova remnant MSH 15−52 (Aharonian et al., 2005a), and HESS J0835−455 (Aharonian et al., 2006f), associated with Vela X, the nebula of the Vela pulsar. In both cases, the morphology in X-rays, where a diffuse nebula extends from the pulsar, is reflected in the morphology observed in γ-rays. These two γ-ray PWNe, as well as others, are extended objects with an angular size of a fraction of a degree, translating into a size of some 10 pc for typical distances of a few kpc. The PWN associated with the γ-ray source HESS J1825−137 (Aharonian et al., 2005c, 2006a) appears much brighter and more extended in VHE γ-rays than in keV X-rays. This suggests that searches in the VHE γ-ray wave band are a powerful tool for detecting PWNe.

Though PWNe represent to date the most populous class of Galactic sources in the VHE γ-ray wave band, the details of the energy conversion mechanisms in the vicinity of pulsars are not well understood, nor is it known which pulsars are able to drive PWNe and produce VHE radiation.

This work presents the first systematic study of a connection between high-power pulsars and VHE γ-ray sources based on a deep survey of the inner Galactic plane conducted with the H.E.S.S. telescopes. It is investigated how the probability to detect in VHE γ-rays PWNe surrounding known pulsars varies with the spin-down energy loss of the pulsar, testing the plausible assumption that the VHE γ-ray output of a PWN correlates in some fashion with the power of the pulsar feeding it. It is shown that pulsars with large spin-down energy flux are indeed with high probability associated with VHE γ-ray sources, implying the existence of an efficient mechanism by which a large fraction of pulsar spin-down energy is converted into kinetic energy of particles. The results presented here make it very likely that future more sensitive γ-ray instruments will detect a rapidly increasing number of lower-luminosity PWNe.

In Chapter 2, neutron stars, the properties of pulsars and the emission mechanisms for pulsed emission are briefly introduced. Further, the formation of PWNe is discussed, along with particle acceleration processes within the nebula and radiation processes for VHE γ-rays. Simulations of the evolution of PWNe within supernova remnants are introduced and a few selected examples of PWN detected in the VHE γ-ray regime by H.E.S.S. are presented.

An overview of the H.E.S.S. experiment and the Imaging Atmospheric Cherenkov Technique and a summary of the standard H.E.S.S. analysis is given in Chapter 3.

The H.E.S.S. data set for the search for a connection between high-power pulsars and VHE γ-ray sources is presented in Chapter 4, along with the pulsar sample used in the search and first results from the search.

Two new PWN candidates were detected in the search. These are discussed in Chapters 5 and 6.

In Chapter 7 the systematic search for a connection between high-power pulsars and VHE γ-ray sources is presented.

Chapter 2

Pulsars and Pulsar Wind Nebulae

Pulsars, highly magnetised neutron stars, are created in the collapse of massive stars. This collapse takes place when the nuclear fusion in the star's core ceases – it explodes in a *supernova*, which may out-shine its entire host galaxy before fading from view over several weeks or months. The explosion expels most of a star's material at velocities up to a few percent of the speed of light, making supernovae the origin for most of the heavy elements in our Galaxy. Figure 2.1 shows an optical image of the Crab Nebula, which is the remnant of the supernova SN1054.

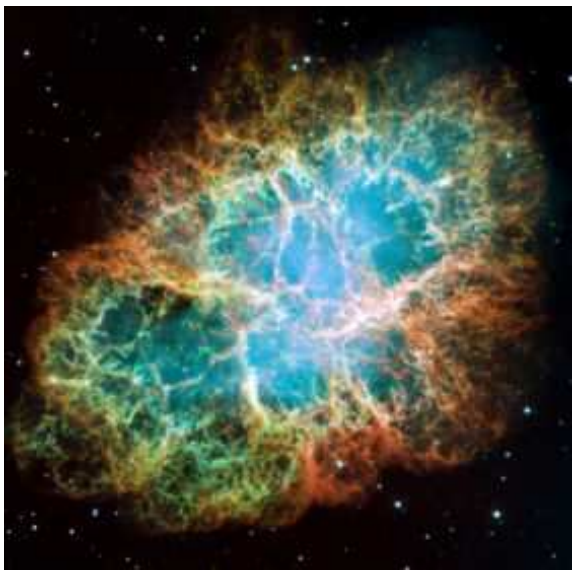

FIGURE 2.1: A mosaic image of the Crab Nebula in optical frequencies, taken by NASA's Hubble Space Telescope.

Highly magnetised neutron stars are end products of type II supernovae. The densities in the inner regions of neutron stars are presumed to exceed the density of normal nuclear matter. Neutron stars rotate rapidly, generating coherent beams of radiation along their magnetic poles, which sweep past the observer like a cosmic lighthouse. This was first observed as pulsed emission in radio frequencies and so named the object pulsar.

After the discovery of the neutron by James Chadwick in 1932, the existence of neutron stars was proposed already in 1934 by Baade and Zwicky (Baade and Zwicky, 1934). The first pulsar was discovered by Jocelyn Bell and Antony Hewish in 1967 (Hewish et al., 1968), the origin of its signal causing the scientists some puzzlement at first:

"The remarkable nature of these signals at first suggested an origin in terms of man-made transmissions which might arise from deep space probes, planetary radar or the reflexion of terrestrial signals from the Moon. None of these interpretations can, however, be accepted because the absence of any parallax shows that the source lies far outside the solar system. ... A tentative explanation of these unusual sources in terms of the stable oscillations of white dwarf or neutron stars is proposed."

In 1974, Hewish was awarded the Nobel Prize in Physics for his "pioneering research in radio astrophysics" and "his decisive role in the discovery of pulsars".

The impact of this discovery on the astronomical community was enormous and led to a flood of both theoretical and observational publications, as most of the larger radio telescopes were immediately directed towards these new objects. In 1968 alone, more than 100 papers reported about observations of pulsars or their interpretation.

Both the Crab and the Vela pulsar were detected in radio wavelength in 1968 (Staelin and Reifenstein, 1968; Large et al., 1968) and it was discovered that the pulse period of the Crab was lengthening with time. Soon, the first basic lighthouse models were proposed, suggesting that pulsars could be rapidly rotating neutron stars spinning at the observed pulse frequency (Gold, 1968, 1969). It is noteworthy that even before the discovery of the first pulsar, Pacini (1968) had suggested that rotating magnetised neutron stars should be able to power supernova remnants like the Crab Nebula and predicted that they might be observable at radio frequencies. In 1969, the Crab pulsar was also discovered in both optical and X-ray wavelength (Cocke et al., 1969; Bradt et al., 1969; Fritz et al., 1969) and the pulsar – supernova correlation was confirmed.

The discovery of the first pulsar in a binary system, in orbit with another star around a common center of mass, was made in 1974 by Russell Hulse and Joseph Taylor (Hulse and Taylor (1975)), and in 1993 they received the Nobel Prize in Physics for this achievement. The first millisecond pulsar ('millisecond' referring to the rotation period of the neutron star) was discovered in 1982 (Backer et al., 1982).

To date, more than 1700 pulsars are known (Manchester et al., 2005), with

pulse periods ranging from 1.4 ms – 11.8 s, masses on the order of 0.1 – 2 $M_\odot$ and radii of about 10 km. Most of these pulsars are *rotation-powered* pulsars with amazingly stable periods that increase slowly with time, on the order of 10^{-15} s/s. This increase is attributed to the energy required for the acceleration of relativistic particles and the electromagnetic radiation at the rotation frequency caused by the strong magnetic field.

Ever since their discovery, pulsars have proven to be invaluable for the study of a wide variety of astrophysical problems, not least because they are the only astrophysical sources that are observable in every astronomical window. Pulsars can e.g. be used as probes for the interstellar medium as they emit pulsed, highly polarised radiation and are found in great abundance everywhere in our Galaxy. On the theoretical side, their coherent radiation processes and the electrodynamics of these rotating magnetised stars have stimulated the work on numerous models and these incredibly dense objects are ideal for exploring the behaviour of matter under extreme conditions of temperature and pressure.

In VHE γ-rays, pulsed emission from pulsars has not been observed yet. However, there have been numerous detections of their extended relativistic outflows, their *pulsar wind nebulae*. The emission processes in pulsars are still poorly understood and it is not known if all pulsars emit VHE γ-rays and form pulsar wind nebulae. Therefore an attempt of a statistical assessment of VHE γ-ray sources with pulsars has been performed. This first population study in the VHE γ-ray regime is presented in this work.

To sketch the phenomenon of a pulsar as a whole, in Section 2.1 neutron stars are introduced and in Section 2.2 an overview of the properties of pulsars and the emission mechanisms for pulsed emission is given. In Section 2.3 the formation of pulsar wind nebulae is discussed, along with the acceleration processes within the nebula and radiation processes for VHE γ-rays. Simulations of the evolution of pulsar wind nebulae within supernova remnants are introduced. Finally, in Section 2.4 a few selected examples of pulsar wind nebulae detected in the VHE γ-ray regime by H.E.S.S. are presented.

2.1 Neutron Stars

During the collapse of a massive star to a neutron star of radius $\sim$ 10 km, the star's extension is reduced by about five orders of magnitude. Inside the neutron star densities prevail of up to ten times the density of normal nuclear matter and the degeneracy pressure of the neutrons keeps the neutron star from collapsing. Stars have generally a very high conductivity and thus strong magnetic fields. The contraction of the progenitor star together with the conservation of the magnetic flux ('magnetic field freezing') leads to very high values for the magnetic field within the neutron star. Since the magnetic flux is $\phi \propto R^2 B = \text{const.}$, with radius R and magnetic field B, it follows that $B \propto R^{-2}$ and therefore the

magnetic field reaches values of up to 10^{12} G. Further, due to the conservation of angular momentum, the contraction increases the rotation velocity of the star by a factor of $\sim 10^{10}$, resulting in rotation periods on the order of a second. Only the extremely strong gravitational force within the neutron star keeps it from being ripped apart – the force is so strong that a free falling body would be accelerated to more than half of the speed of light towards the neutron star.

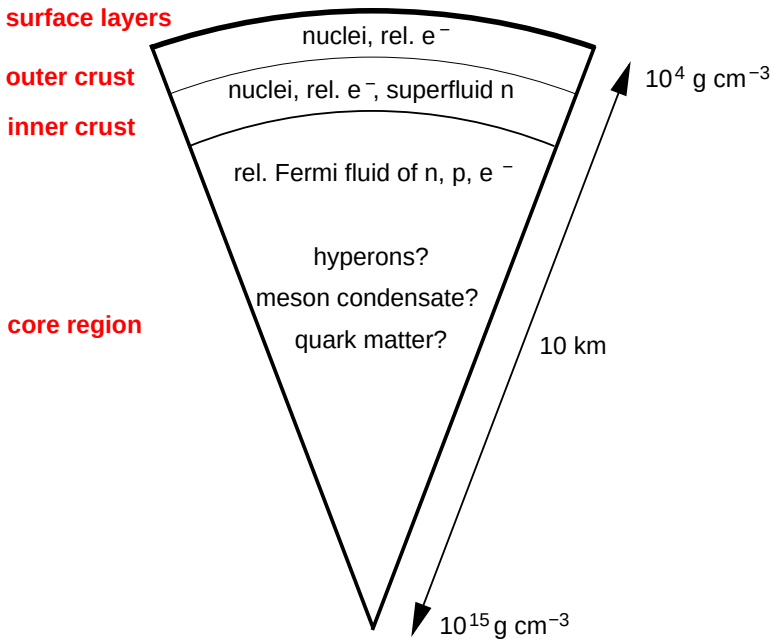

FIGURE 2.2: Internal structure of a $1.4\,M_\odot$ neutron star (after Weber (1999)).

Figure 2.2 shows a schematic of the internal structure of a $1.4\,M_\odot$ neutron star, following Weber (1999):

- *Surface layers*: Consist of normal nuclei and non-relativistic electrons at mass densities between 10^3 g cm^{-3} and 10^6 g cm^{-3}.
- *Outer crust*: The atomic nuclei become neutron rich since the density and therefore the pressure is great enough for inverse $-\beta$ decay to set in. The nuclei form a solid Coulomb lattice. Here, densities range between 7×10^6 g cm^{-3} and 4.3×10^{11} g cm^{-3}, making the electrons become relativistic. The presence of this degenerate relativistic electron gas ensures that the magnetic field exists in the inner regions of the star.
- *Inner crust*: At the *neutron drip* density, 4.3×10^{11} g cm^{-3}, neutrons begin to escape from the neutron-saturated nuclei, become unbound and populate free states. Up to densities of 2×10^{14} g cm^{-3}, the matter clusters

into extremely neutron-rich nuclei that are immersed in a gas of superfluid neutrons and relativistic electrons.

- *Core region*: At densities $> 2 \times 10^{14}$ g cm^{-3} the clusters begin to dissolve and neutrons, protons and electrons form a relativistic Fermi fluid. The composition of the interior of neutron stars is unclear; hyperon production might set in at densities of about twice the nuclear matter density, meson condensates might form and/or a transition of confined hadronic matter into quark matter might take place.

At birth, neutron stars are expected to be very hot, as they have to dispose of their gravitational binding energy and as the collapse heats the core to extremely high temperatures. They cool mainly by neutrino emission from their interior and by thermal radiation from their surface. The predicted surface temperature of neutron stars is on the order of 10^6 K throughout most of their active life as pulsars.

2.2 Pulsars

Figure 2.3 shows a schematic model of a pulsar as a magnetised rotating neutron star with its rotation axis tilted with respect to the magnetic axis. As the star rotates, its magnetic axis precesses around the rotation axis, causing the emission beam from the magnetic poles to sweep past an observer situated within the light field, which makes the emission appear to be pulsed. How this emission is produced is up to today, 40 years after the discovery of the first pulsar, not fully understood. Currently there are two main concurrent emission models for high-energy emission from pulsars, which are briefly introduced in Section 2.2. See Kramer (2005) for a general review about pulsars.

The pulse periods of pulsars can be measured to great accuracy. The periods as well as the increase of the periods with time are of great interest, as they can be used e.g. for estimating the rotational power output of a pulsar and to provide an age estimate for the pulsar. A measure for the rotational power output of a pulsar is its *spin-down luminosity*, $\dot{E}$. The spin-down luminosity is given by the loss in rotational energy, which can be measured from the pulsar spin period, P, and the period derivative, $\dot{P}$:

$$\dot{E} = 4\pi^2 I \dot{P} P^{-3} = I \dot{\Omega} \Omega, \tag{2.1}$$

where I is the neutron star moment of inertia with typical values of $I = 10^{45}$ g cm^2 and Ω is the angular frequency of the rotation ($\Omega = 2\pi/P$). $\dot{E}$ represents the energy output across the whole energy spectrum. With knowledge of the distance d of a pulsar, one can estimate the *spin-down energy flux*, $\dot{E}/(4\pi d^2)$.

The slow down of the pulsar can be written as:

$$\dot{\Omega} = k\Omega^n, \tag{2.2}$$

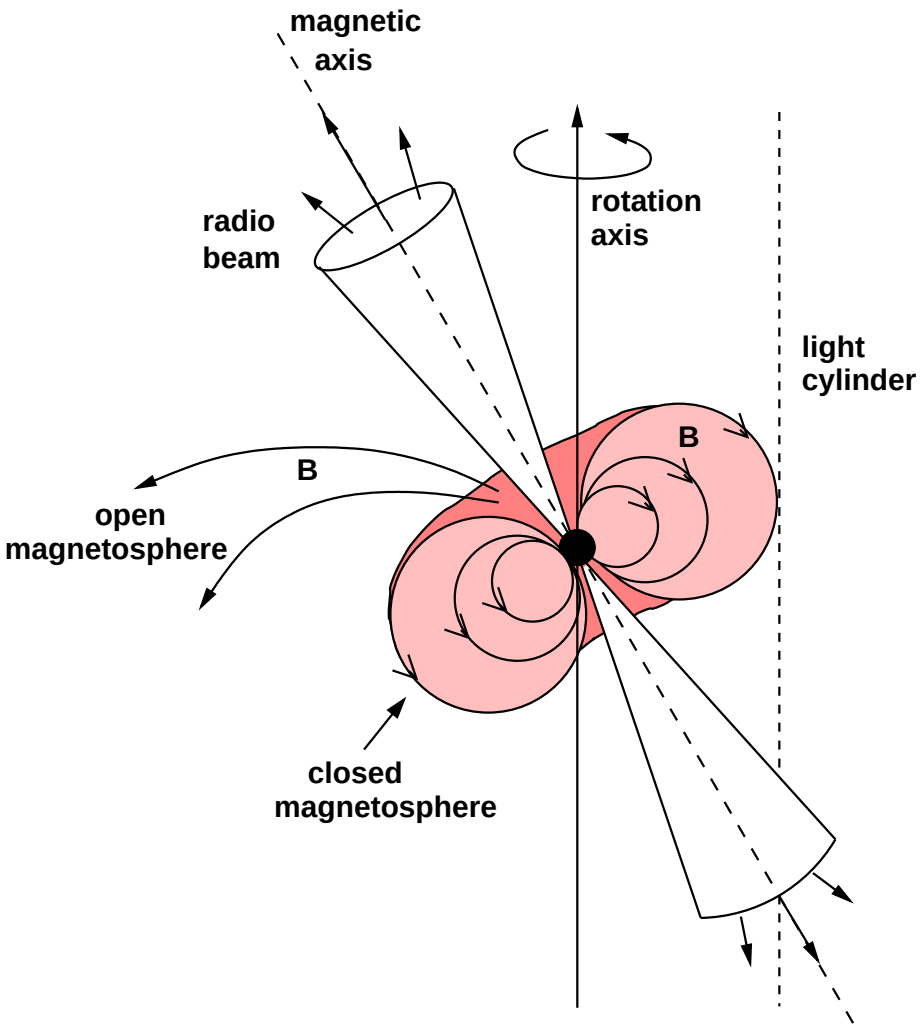

FIGURE 2.3: Schematic model of a pulsar (i.e. a magnetised rotating neutron star): the rotation and magnetic axis are misaligned, leading to the radio beam to sweep past the observer and thus create the pulsed emission.

where k is a constant and n is the *braking index*. The braking index depends on the energy loss mechanism responsible for the slow down of the pulsar. In case of pure *magnetic braking*, i.e. that all energy is lost due to magnetic dipole radiation, the braking index is $n = 3$. The braking index can be directly evaluated if a measurement of the second derivative of Ω, is possible ($\ddot{\Omega} = nk\dot{\Omega}^{(n-1)}$). Most pulsars show a value for n significantly smaller than 3, indicating that magnetic braking is not in all cases the only relevant cause for the deceleration of the pulsar. Some of the slow down might e.g. be caused by out flowing particles, which remove angular momentum from the star.

Assuming pure magnetic braking, $n = 3$, and integrating equation 2.2, the *characteristic age* of a pulsar can be estimated to:

$$\tau_c = \frac{P}{2\dot{P}}. \tag{2.3}$$

While this relation gives a good estimate for the age of most pulsars, it can overestimate the true age of young pulsars, as it only holds true for initial spin periods that are much smaller than the current spin period (i.e. $\Omega_0 \gg \Omega$), which is generally not the case for young pulsars.

Finally, to find an estimate for the distance for a pulsar one can make use of the slightly dispersive nature of the interstellar medium, causing light of lower frequencies to arrive later at the observer than light of higher frequencies. By measuring this *dispersion*, i.e. the pulse arrival times at different frequencies, one measures the accumulated time difference caused by the difference in group velocity over the path length. With knowledge of the average electron density, $\langle \rho_e \rangle$, in the direction of the pulsar, one can directly determine the distance of the pulsar to the observer, L, from the dispersion measure DM:

$$\mathrm{DM} = \int \mathrm{d}l \, \rho_e(l) \approx L \, \langle \rho_e \rangle. \tag{2.4}$$

Pulsed high-energy Emission from Pulsars

Pulsed non-thermal radiation originates from particle acceleration in the magnetic field within the light cylinder of the pulsar, the *magnetosphere* (see Figure 2.3). Goldreich and Julian (1969) first proposed a model for the pulsar as a rotating magnet, with the magnetic axis aligned with the rotation axis. The basic idea is that the charges within the neutron star rearrange due to a Lorentz force acting upon them, and thus induce an electric field in the star. This leads to a large electric field component parallel to the magnetic field above the star's surface, which exceeds even the huge gravitational force and is strong enough to pull charges out of the surface. Therefore a particle plasma surrounds the neutron star, which will co-rotate with the star within the light cylinder, at which the velocity of the co-rotating charges bound to the closed magnetic field lines becomes equal to the speed of light and the co-rotation cannot be maintained. The plasma is believed to escape the magnetosphere along the open field lines that are torn beyond the light cylinder due to the inertia of the plasma at these high velocities, resulting in a wind flow of magnetic and particle energy into a surrounding nebula (see Section 2.3). How the wind connects with the magnetosphere remains an unsolved theoretical problem.

Kaspi et al. (2004) give a general review on isolated neutron stars and a summary about emission models and Harding (2001) offers a more detailed review on emission models. The two concurrent models to date for high-energy emission

from pulsars are the *polar cap* models and the *outer gap* models, their main distinction being the emission region. As they also predict different spectral shapes, detailed spectrometric γ-ray measurements should help to distinguish between these models. The geometry of polar caps and outer gaps is schematically shown in Figure 2.4.

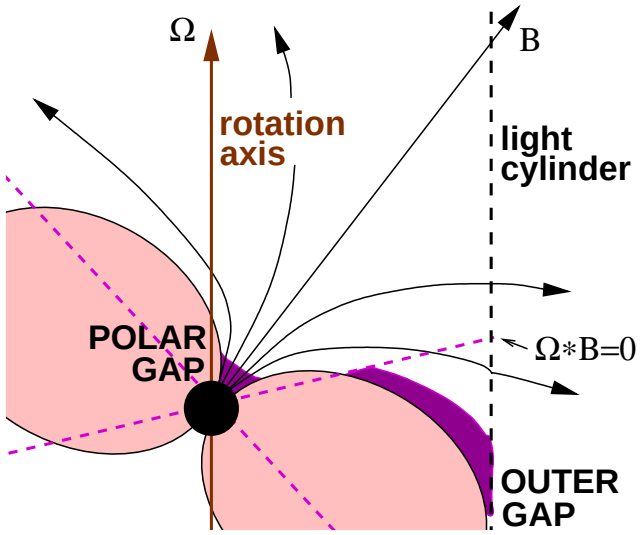

FIGURE 2.4: Schematic geometry of polar caps and outer gaps, indicated in magenta (following Harding (2001)).

Both models assume that primary γ-rays are produced by ultra-relativistic electrons accelerated in quasi-static electric fields. A strong $E_{\parallel}$ may develop to accelerate particles at two possible sites within the magnetosphere, where the outflow of particles will open a gap, i.e. a charge-depleted region: at the *polar caps*, where the acceleration and radiation occur near the magnetic poles and thus in the inner magnetosphere or in *outer gaps*, where these processes occur in the outer magnetosphere.

In polar-cap models, particle acceleration is assumed to occur near the neutron star surface and high-energy emission results from curvature radiation or inverse-Compton induced pair cascades in the strong magnetic field. These models predict spectra with sharp (super-exponential) cutoffs at energies typically below 10 GeV.

Outer-gap models assume that acceleration occurs in vacuum gaps that develop in the outer magnetosphere, along the last open field line above the *null charge surface*, i.e. the place where the co-rotation charge density changes sign

(indicated as $\Omega \cdot B = 0$ in Figure 2.4), and that high-energy emission results from photon-photon pair production induced cascades. In these models, the cutoff energy is not as restricted as in the polar cap models, and the spectrum drops more slowly.

2.3 Pulsar Wind Nebulae

Pulsars are generally presumed to drive powerful winds of highly relativistic particles (see e.g. Gaensler and Slane (2006) for a review). As the pulsar is embedded in slowly moving un-shocked ejecta from the supernova (SN) explosion, these winds can drive strong shocks into the ejecta, at which particles (electrons, positrons and maybe hadrons) may be accelerated to ∼PeV energies. Evidence for high-energy electrons and positrons[1] in these pulsar wind nebulae (PWNe) is provided by the observation of both synchrotron emission in the radio through high-energy γ-ray regimes, and by inverse-Compton (IC) radiation from their interaction with ambient photon fields in the high-energy and VHE γ-ray range. Additionally, in the interaction of relativistic protons and nuclei with ambient gas, proton - proton collisions can produce VHE γ-rays through the decay of neutral pions. In Section 2.3.1 the formation of PWNe and the acceleration and radiation mechanisms for particles within the nebula are discussed. In Section 2.3.2 hydrodynamical simulations of the evolution of the system PWN – supernova remnant (SNR) are shown.

2.3.1 Formation of PWNe, Acceleration and Radiation Processes

The formation of pulsar winds is not yet completely understood. The basic idea, outlined partially already in Section 2.2, is that a charge-filled magnetosphere surrounds the pulsar and that particles are accelerated in the collapse of charge-separated gaps, either at the polar caps or in outer gaps of the pulsar. Along open field lines (see Figure 2.3) the plasma flows from the light cylinder and forms the pulsar wind.

Figure 2.5 shows a sketch of the PWN – SNR system. Following e.g. Reynolds and Chevalier (1984), a pulsar within an SNR inflates a roughly homogeneous bubble of relativistic particles and magnetic field amidst the freely expanding supernova ejecta. The particle wind is initially relativistic, therefore a wind shock will form within the bubble, even though the dominant energy flux is thought to be the Poynting flux of the magnetic dipole radiation at first. The bubble gains energy from the pulsar and loses it via synchrotron and IC radiation and while it sweeps up the surrounding material. The SNR shell expands much

[1] from here, electrons stands for both electrons and positrons

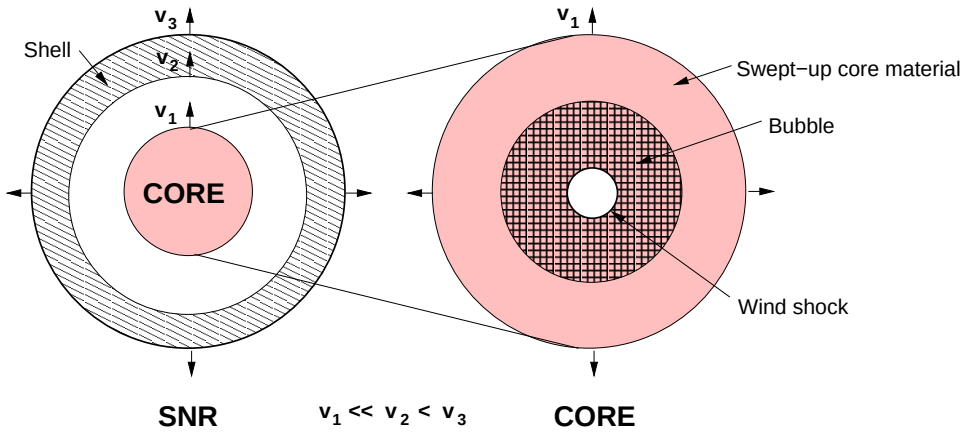

FIGURE 2.5: Schematic representation of the SNR – PWN system (after Reynolds and Chevalier (1984)). The expansion speeds of the outer and inner edges of the fast SNR shell are denoted with v_3 and v_2, respectively, and the speed of the outer edge of the core material with v_1. On the right side, a larger view of the core of the SNR is provided; note that the pulsar light cylinder is far inside the the wind shock.

faster than the core material until it has swept up roughly its own mass from the interstellar medium. Then it decelerates and sends a reverse shock through the SN ejecta and the bubble.

Acceleration Processes in PWNe

At the termination shock of the pulsar-driven wind particles can be accelerated to ultra-relativistic energies. This acceleration is thought to happen by the Fermi mechanism (Fermi, 1949) in *diffusive shock acceleration* but could also be linked to driven reconnection of the alternating magnetic field at the termination shock (see e.g. Lyubarsky (2003)).

In the paper by Achterberg et al. (2001), the acceleration process of diffusive shock acceleration and the comparison to semi-analytical simulations are presented. They show that the spectrum resulting from this ultra-relativistic equivalent to the Fermi acceleration at a shock is a power law $N(E) \propto E^{-s}$, with a nearly universal value for the spectral slope of $s \approx 2.2 - 2.3$.

Production Processes of VHE Gamma-rays

The particles of the pulsar wind interact with ambient photon fields, magnetic fields and matter, and can produce VHE γ-rays in these interactions. Aharonian (2004) gives an excellent overview of γ-ray production mechanisms and of VHE cosmic γ-radiation in general.

The interaction of relativistic particles with radiation fields through IC scattering is the dominant processes for the generation of VHE γ-rays in PWNe, as the cosmic microwave background radiation is found everywhere as a target field and additional photon fields are present in many of these objects. This process is mainly important for energetic electrons, as it is suppressed for protons in comparison to electrons by a factor of $(m_{\rm e}/m_{\rm p})^4$. The IC emission from PWNe is expected to peak in the high-energy to VHE γ-ray range, if the electrons are in the *Klein-Nishina* regime, i.e. ultra-relativistic, and therefore transfer nearly their total momentum to the up-scattered photons.

Synchrotron radiation is emitted in the radio through high-energy γ-ray regimes by VHE electrons gyrating in magnetic fields. The synchrotron emission from PWNe is expected to peak in the X-ray range.

Another process for the generation of VHE γ-rays is the interaction of relativistic protons and nuclei with ambient gas. In these inelastic collisions, pions, kaons and hyperons are produced. For the hadronic component of the cosmic rays, the decay of neutral pions provide the main channel for the conversion of kinetic energy of relativistic protons and nuclei into high-energy γ-rays ($pp \rightarrow \pi^0 \rightarrow 2\gamma$). It was shown that the γ-ray spectrum basically repeats the spectrum of the parent protons, thus high-energy γ-rays can provide direct information about the primary nucleonic cosmic rays. See e.g. Aharonian (2004) for more detail.

Figure 2.6 shows an example of modelling the spectral energy distribution from a PWN, by Aharonian et al. (1997). Assuming electrons as the radiating particles and the cosmic microwave background radiation as the dominant target photon field for the production of γ-radiation, the relation between the energies of the synchrotron photons ($E_{\rm S}$) and the IC photons ($E_{\rm IC}$) produced by the same electrons is

$$\frac{E_{\rm S}}{1\,{\rm keV}} \simeq 0.07\,(\frac{E_{\rm IC}}{1\,{\rm TeV}})\,(\frac{B}{10^{-5}\,{\rm G}}). \tag{2.5}$$

Depending on different values for the magnetic field (top panel of Figure 2.6), the cutoff energy for electrons due to radiative losses (middle panel of Figure 2.6) and the age of the pulsar (bottom panel of Figure 2.6), different curves are obtained. As can be seen in the top panel, in the case of a low magnetic field comparable with magnetic fields in the interstellar medium ($B_{\rm ISM} \sim (3-5) \times 10^{-6}$ G), both synchrotron and IC processes contribute equally to the total energy loss. However, for significantly higher magnetic fields, synchrotron losses become the main energy loss process. In the middle panel, the influence of the exponential cutoff in the injection spectrum of the electrons is shown, and Aharonian et al. (1997) conclude that for cutoffs beyond 10 TeV, the IC γ-ray luminosity peaks at TeV energies and the synchrotron luminosity peaks at keV energies. The influence of the pulsar age on the spectral energy distribution can be seen in the bottom panel – with age, the synchrotron and IC luminosities saturate at maximum levels

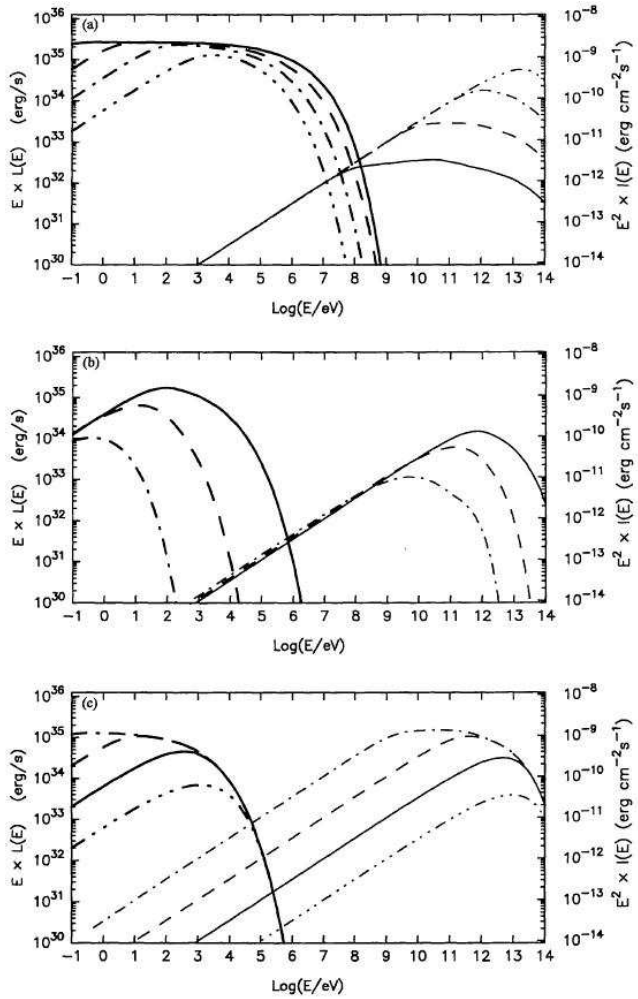

FIGURE 2.6: Aharonian et al. (1997): Synchrotron and IC radiation components from a nebula surrounding a pulsar injecting electrons with a power law spectrum with index 2 at a constant rate $L_e = 10^{37}$ erg s^{-1}. *Top panel*: Age of the pulsar ($T = 10^4$ yr) and cutoff energy of electrons ($E_0 = 1000$ TeV) are fixed. The curves correspond to $B = 10^{-4}$ G (solid lines), $B = 3 \times 10^{-5}$ G (dashed lines), $B = 10^{-5}$ G (dot-dashed lines) and $B = 3 \times 10^{-6}$ G (3dot-dashed lines). *Middle panel*: Age of the pulsar ($T = 10^4$ yr) and magnetic field ($B = 10^{-5}$ G) are fixed. The curves correspond to $E_0 = 100$ TeV (solid lines), $E_0 = 10$ TeV (dashed lines) and $E_0 = 1$ TeV (dot-dashed lines). *Bottom panel*: Magnetic field ($B = 10^{-5}$ G) and cutoff energy of electrons ($E_0 = 100$ TeV) are fixed. The curves correspond to $T = 10^3$ yr (3dot-dashed lines), $T = 10^4$ yr (solid lines), $T = 10^5$ yr (dashed lines) and $T = 10^6$ yr (dot-dashed lines). The left-hand-side axes indicate the γ-ray flux luminosities, the right-hand-side axes are scaled to the fluxes expected for pulsars at distance $d = 1$ kpc.

while the peaks get shifted to lower energies.

2.3.2 PWN in an evolving SNR

In this section a model of a PWN evolving in its associated SNR is discussed, following van der Swaluw et al. (2004). This example was chosen since, due to asymmetries in the supernova explosion, pulsars are generally expected to receive a *kick velocity* at birth. Simulations for the same system with a non-moving pulsar have been performed e.g. by van der Swaluw et al. (2001); Blondin et al. (2001) and Bucciantini et al. (2003). van der Swaluw et al. (2004) use second order hydrodynamics simulations to predict the dynamics of the interaction between the wind of the pulsar and the SNR, for the case of a pulsar with high velocity.

At first, the SNR is in its ballistic phase: with an initial velocity of up to $0.03c$ its ejecta expand almost freely and drive a strong shock into the ambient medium. The pressure of the shock-heated surroundings produces a weak reverse shock in the ejecta. The wind from the pulsar produces the PWN bubble, which expands supersonically and thus drives a shock into the ejecta (note that this is not the wind termination shock). Figure 2.7 shows the density distribution of the system at this early stage. When the mass swept-up by the SNR shell roughly equals the initial ejecta mass, the SNR enters the *Sedov-Taylor phase* and its reverse shock starts to move towards the centre of the SNR. The SNR forward and reverse shock are divided by a contact discontinuity, which can lead to instabilities and secondary shocks. The reverse SNR shock collides with the PWN shock after typically a few thousand years and subsequently crushes the PWN bubble (shown in Figure 2.8). This will lead to oscillations of the PWN for a time span of a few thousand years. Due to the crushing of the nebula, Rayleigh-Taylor instabilities can form, which can lead to the mixing of non-thermal and thermal material and to a significant increase of the magnetic field within the PWN. At the time of the collision between the SNR reverse shock and the PWN shock the pulsar might have already moved away from the centre of the SNR. In this case, the PWN produced by the pulsar is also offset and the reverse shock collides earlier at one side with the PWN shock than at the other. Therefore, the PWN can show a very asymmetrical morphology and might be displaced from the pulsar position. Afterwards, the PWN expands unsteadily due to the reverberations from the violent collision and the expansion of the PWN is subsonic because the surroundings of the PWN have been re-heated by the passage of the reverse shock. The original PWN shock has disappeared. After the interaction with the SNR reverse shock and after the oscillations of the PWN have faded, the pulsar will steadily build up its nebula within the hot, shocked ejecta of the SNR at subsonic speeds. This means that the pulsar can leave behind its original PWN (now a *relic*) and generate a new, smaller PWN around its current position. The PWN head and the relic PWN are indicated in Figure 2.9. As the pulsar moves to the edge of the SNR, the sound speed in the shocked ejecta decreases, which leads to

the pulsar moving supersonically and driving a cometary *bow shock*, with a Mach cone around it. The bow shock is shown in Figure 2.10. The pulsar wind is in pressure equilibrium with its surroundings, so the PWN does not expand further with time. In this simulation, after $\sim$ 40000 yrs, the pulsar will cross its SNR shell and might re-brighten the shell during its passage. After the pulsar has left its SNR it will move through the interstellar medium, often highly supersonic, and still show a bow shock. This shock might be seen in Hα emission and in radio and X-rays as synchrotron radiation. Finally, the pulsar moves away from the dense gas in the Galactic plane to low density regions, while its $\dot{E}$ drops, thus it is not anymore able to power a synchrotron nebula. It turns into a *ghost nebula*, which have yet to be detected. It could also be spun up by accreting mass from a companion in a binary system and become a millisecond pulsar, as which it would be able to produce a new bow shock.

van der Swaluw et al. (2004) divide their simulations into four stages: *supersonic expansion stage*, where the simulation shows a PWN off-centred with respect to the twofold shock structure of the SNR due to kick velocity of PSR (see Figure 2.7), the *reverse shock interaction stage*, where the timescale on which the reverse shock collides with the PWN can be a significant fraction of the total PWN lifetime and scales roughly with the pulsar velocity (see Figure 2.8), the *subsonic expansion stage*, where the PWN position is strongly off-centred after the passage of the reverse shock (see Figure 2.9) and as a final stage the *bow shock stage*, where the head of the PWN, containing the active pulsar, deforms into a bow shock due to the supersonic motion of the pulsar (see Figure 2.10).

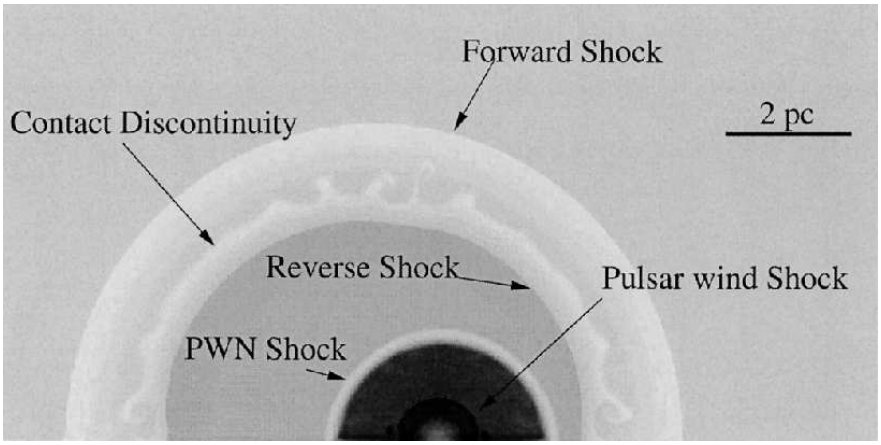

FIGURE 2.7: *Supersonic expansion stage*: Logarithmic gray-scale plot of the density distribution at an age $t_{\rm SNR} = 1000$ years (from van der Swaluw et al. (2004)).

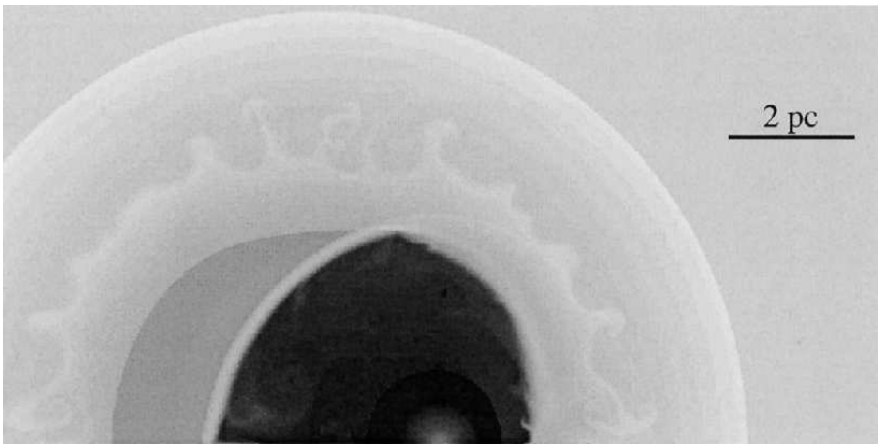

FIGURE 2.8: *Reverse shock interaction stage*: Logarithmic gray-scale plot of the density distribution at an age $t_{\rm SNR} = 1800$ years (from van der Swaluw et al. (2004)).

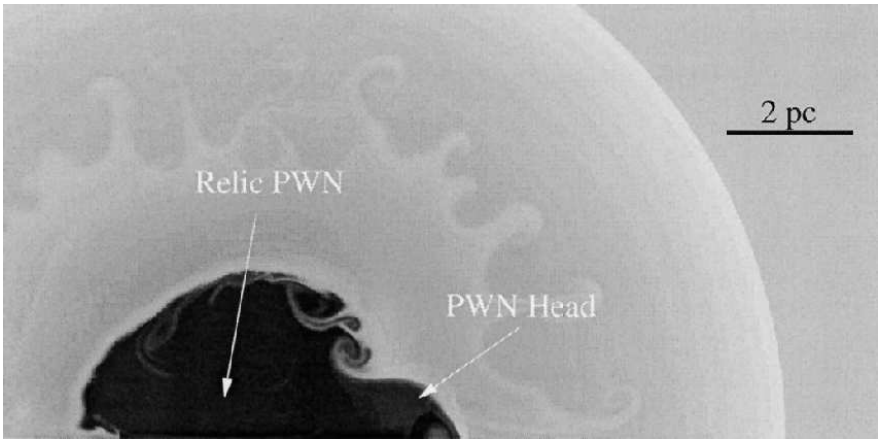

FIGURE 2.9: *Subsonic expansion stage*: Logarithmic gray-scale plot of the density distribution at an age $t_{\rm SNR} = 3000$ years (from van der Swaluw et al. (2004)).

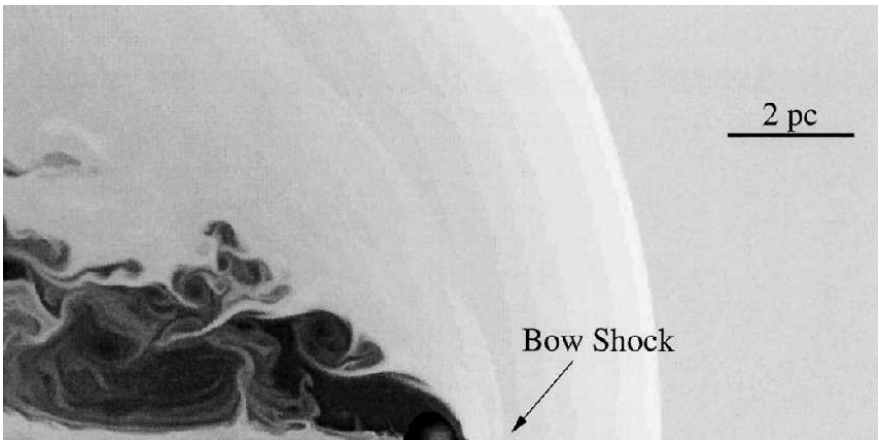

FIGURE 2.10: *Bow shock stage*: Logarithmic gray-scale plot of the density distribution at an age $t_{\rm SNR} = 11400$ years (from van der Swaluw et al. (2004)).

2.4 H.E.S.S. Observations of PWNe

Of the Galactic VHE emitters, a significant number can be identified as PWNe. Amongst others, VHE γ-rays have been detected by H.E.S.S. from the PWN located within the supernova remnant MSH 15−5*2*, for the PWN associated with the γ-ray source HESS J1825−137, for Vela X, associated with the Vela pulsar, and in the Kookaburra Complex. From the combined image in Figure 2.11 it can be seen that these PWNe are all extended sources for H.E.S.S. and that all are offset from their respective pulsar, possibly due to the motion of the pulsar causing it to leave the nebula behind or to a density gradient in the ambient medium.

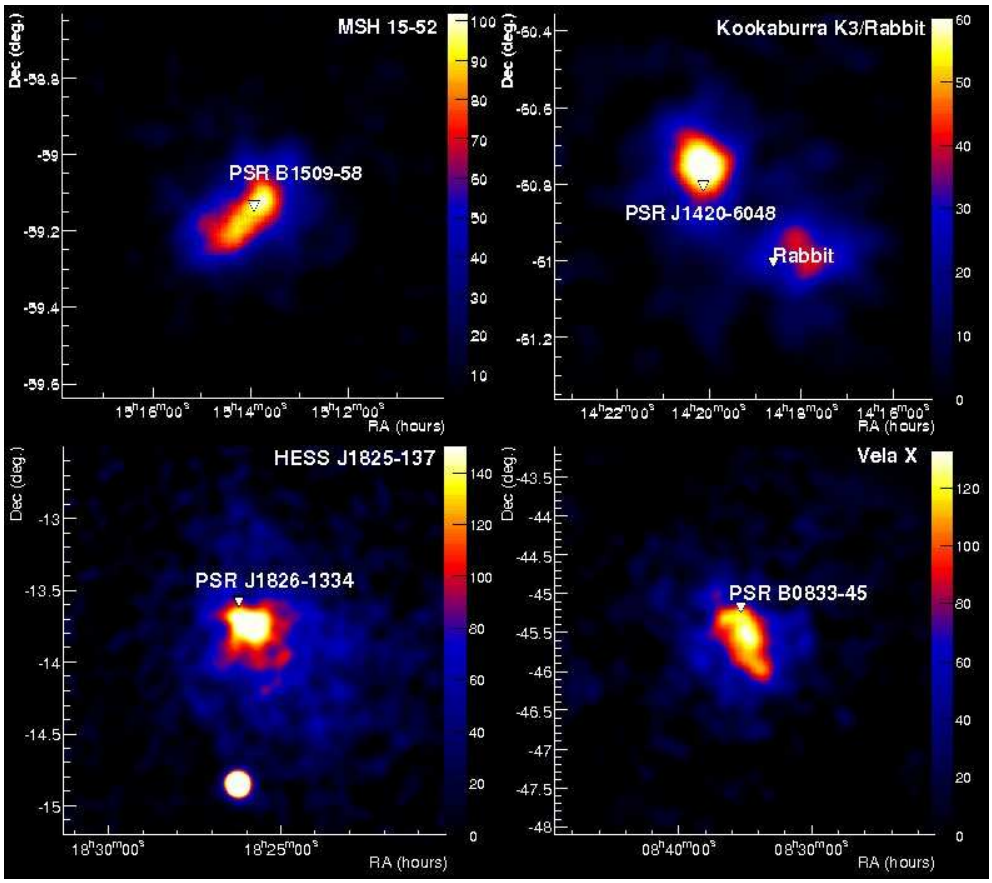

FIGURE 2.11: Image of VHE γ-ray excess counts of four VHE PWNe (from upper left counter-clockwise): MSH 15−5*2*, HESS J1825−137, Vela X and the Kookaburra region. The white triangles mark the pulsar positions (by courtesy of S. Funk).

MSH 15−52

The H.E.S.S. observations of the SNR MSH 15−52 provided the first image of an extended PWN in the VHE range (Aharonian et al., 2005a). The γ-ray signal is detected at a statistical significance of $\sim 25\sigma$ in ~ 22 hours of observations. Figure 2.12 shows the H.E.S.S. excess map in the left panel with overlaid ROSAT X-ray contours (Trussoni et al., 1996). In the right panel the Chandra X-ray map (Gaensler et al., 2002) of the vicinity of the pulsar PSR B1509−58 is shown (see axes scales). The VHE γ-ray emission region is clearly extended towards the South-East, which coincides with the diffuse PWN as observed at X-ray energies by the ROSAT and Chandra satellites. This suggests a leptonic origin of the VHE signal, since if the VHE γ-rays originate from IC scattering on target photons by electrons, these electrons should emit synchrotron radiation in the X-ray regime. The overall energy spectrum of the H.E.S.S. source ranges from 280 GeV up to 40 TeV and can be fitted by a power law with a photon index of ~ 2.3.

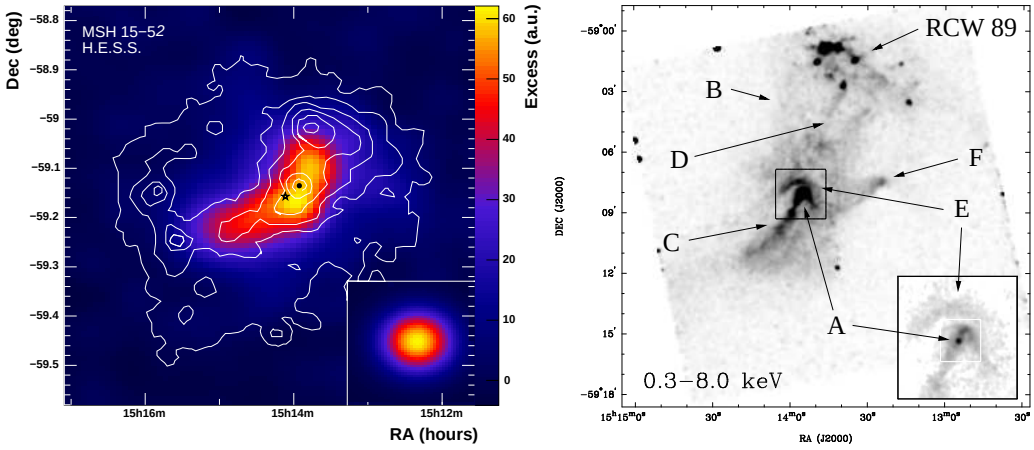

FIGURE 2.12: *Left:* H.E.S.S. smoothed excess map in arbitrary units. The black point denotes the pulsar position and the black star the best-fit position. ROSAT X-ray contours in the (0.6-2.1) keV band are overlaid in white (Trussoni et al., 1996). The inset shows the H.E.S.S. point-spread function. *Right:* Chandra X-ray map of the region around PSR B1509−58 in the (0.3-8.0) keV band. The pulsar is marked as feature A in both the main panel and the inset. The diffuse nebula can be seen extending ~ 6' North-West/South-East of the pulsar. Superimposed on the diffuse emission, a jet-like feature towards the South-East of the pulsar is visible, marked as feature C (Gaensler et al., 2002).

HESS J1825−137

HESS J1825−137 was detected with a significance of $\sim 8\sigma$ in the Galactic plane survey conducted by H.E.S.S. in 2004, and was re-observed in 2005 (Aharonian et al.,

2005c, 2006a). It is possibly associated with the PWN of the pulsar PSR J1826−1334. X-ray observations with the XMM-Newton satellite have revealed an asymmetric X-ray PWN extending to the south of the pulsar, on a much smaller scale than the VHE emission (Gaensler et al., 2003). Figure 2.13 compares the H.E.S.S. excess map in the left panel to the XMM-Newton map in the right panel, which displays a much smaller field of view. The larger VHE nebula can be explained by the supposedly longer lifetime of TeV emitting electrons compared to X-ray emitting electrons, thus electrons from earlier epochs contribute to the present VHE flux. A significant softening of the γ-ray spectrum away from the position of the pulsar has been found, providing the first direct evidence of an energy-dependent morphology in VHE γ-rays.

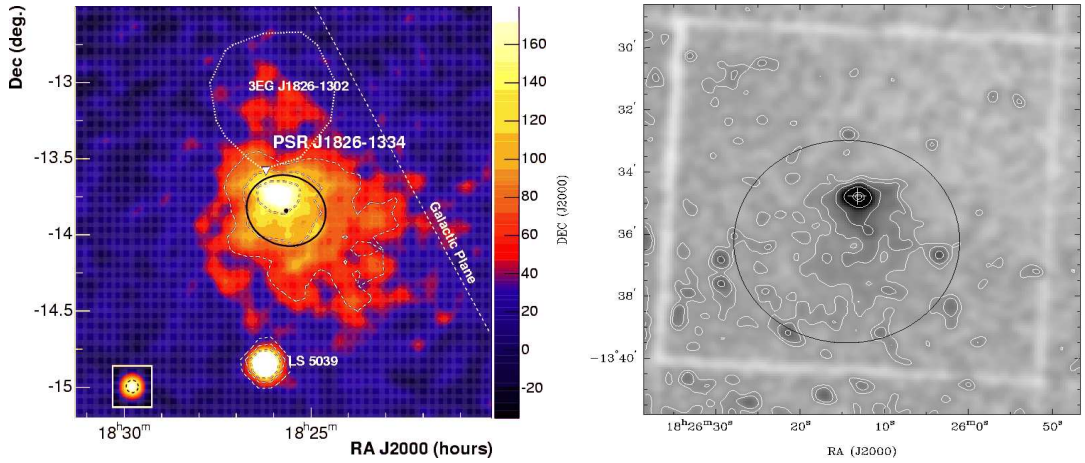

FIGURE 2.13: *Left:* H.E.S.S. smoothed excess map in units of integrated excess counts. The best-fit position is marked as a black dot and the best extension and orientation angle as a black ellipse. The position of the pulsar is marked with a white triangle and the inset shows the point-spread function. *Right:* XMM-Newton image in the (0.5-10.0) keV band of the field surrounding PSR J1826−1334 centred on the pulsar, which is marked by a white cross. The faint white contours denote levels of the peak intensity (Gaensler et al., 2003).

Vela X

The Vela SNR is a complex region containing a number of sources of non-thermal radiation. H.E.S.S. observed the inner section of Vela, within 2 degrees of the Vela pulsar, PSR B0833−45, for ∼16 hours live time in 2004 and 2005 (Aharonian et al., 2006f). A strong signal of $\sim 21\sigma$ is seen from an extended region to the south of the pulsar. The excess coincides with a region of hard X-ray emission seen by the ROSAT satellite (Markwardt and Ogelman, 1995). Figure 2.14 displays the H.E.S.S. excess map with overlaid ROSAT con-

tours in the left panel. In the right panel a Chandra X-ray close-up view of the region surrounding the Vela pulsar is shown, in which a toroidal structure and perpendicular jet can be seen, along with a faint halo of emission, which is likely associated with the post-shock pulsar wind (Helfand et al., 2001). The spectral energy distribution of the H.E.S.S. source shows the first clear measurement of a peak in the spectral energy distribution at TeV energies from a VHE γ-ray source, likely related to IC emission.

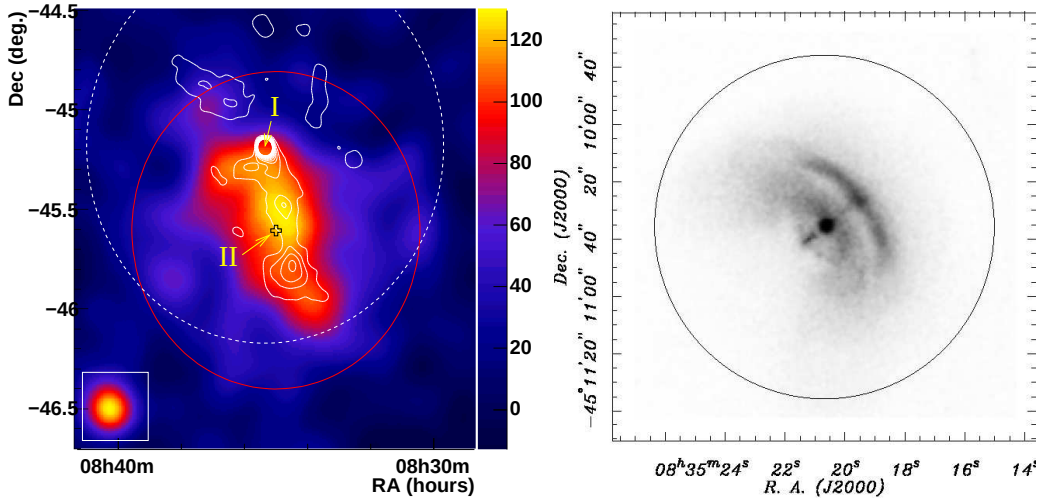

FIGURE 2.14: *Left:* H.E.S.S. smoothed excess map of the region around the Vela pulsar (Position I). The significant emission is coincident with a ROSAT X-ray feature, which is shown in white contours (Markwardt and Ogelman, 1995). Position II denotes the best-fit position and the inset indicates the size of a point source as seen by H.E.S.S., for an equivalent analysis. *Right:* A close-up view of the region surrounding the Vela pulsar (centred on the pulsar) taken by the Chandra satellite in the (0.1-10.0) keV band. A toroidal structure and perpendicular jet can be seen, along with a faint halo of emission likely associated with the post-shock pulsar wind (Helfand et al., 2001).

Kookaburra

The Kookaburra is a complex of about one square degree in size, consisting of compact as well as extended radio/X-ray sources. Radio images revealed a large circular shell with a broad wing to the North-East and a narrower wing to the South-West. Observations of ∼18 hours live time in 2005 resulted in the discovery of two VHE sources coinciding with the wings, HESS J1418−609 and HESS J1420−607 (Aharonian et al., 2006d). In Figure 2.15, the H.E.S.S. smoothed excess map is shown in the left panel and the right panel displays Chandra and XMM-Newton X-ray imaging data with ATCA radio contours overlaid

(Ng et al., 2005). The two dashed circles denote the K3 PWN, which is attributed to the energetic pulsar PSR J1420−6048 and coincides with the southern part of HESS J1420−607, and the 'Rabbit' PWN, which coincides with the eastern part of HESS J1418−609 and where no pulsar has been found yet. Both H.E.S.S. sources show similarly hard VHE spectra with photon indices of ~ 2.2 (for a pure power law) and are each most likely associated to a PWN.

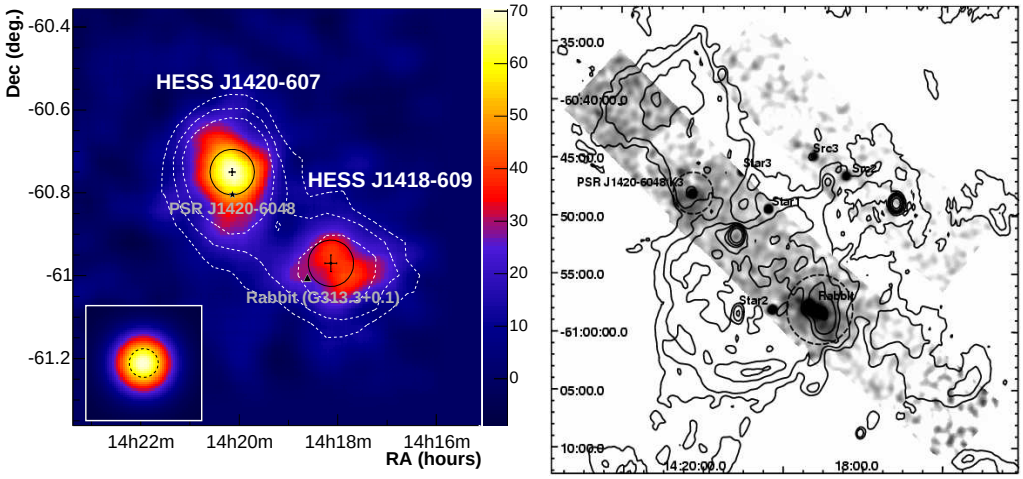

FIGURE 2.15: *Left:* H.E.S.S. smoothed excess map of the $1° \times 1°$ field of view of the Kookaburra region, with the H.E.S.S. point-spread function in the inset. The white contours denote the 5, 7 and 10σ significance levels. PSR J1420−6048 is marked by a black star and the position of the 'Rabbit' is marked by a black triangle. *Right:* Chandra and XMM-Newton X-ray imaging data (Ng et al., 2005) in the (1-7) keV band with ATCA radio contours overlaid. The two dashed circles denote the K3 PWN, which is attributed to the energetic pulsar PSR J1420−6048, and the 'Rabbit' PWN, where no pulsar has been found yet.

Chapter 3

H.E.S.S. and the Imaging Atmospheric Cherenkov Technique

The Earth is constantly bombarded with elementary particles and atomic nuclei over a large range of energies. These *cosmic rays* arrive isotropically and consist mainly of protons, some α-particles, few heavy atomic nuclei, electrons and positrons and very few photons and neutrinos. The energy spectrum of this radiation is measured to date over a range of ten decades up to energies of about 10^{20} eV and can be described by a power law with index -2.7 over most of its range.

To search for the sources of high-energy cosmic rays, the small fraction (0.2%) of neutral cosmic-ray messenger particles, neutrinos and photons (γ-rays) can be used. These are, unlike charged cosmic-ray particles, not deflected by the interstellar magnetic fields and thus provide the observer with directional information about their sources.

Up to energies of about 50 GeV, satellite instruments like INTEGRAL and EGRET are suitable for detecting γ-rays. GLAST, a satellite instrument to be launched in near future, will measure γ-rays with energies up to $\sim$100 GeV. To date, the ground-based Imaging Atmospheric Cherenkov Technique (IACT) is the most successful detection technique for VHE γ-rays above 100 GeV, since in this energy range the fluxes are too low for satellite instruments to achieve a significant detection within reasonably short timescales. The IACT makes use of the atmosphere as a detector by recording the Cherenkov light emitted by secondary particles that are generated in interactions of primary γ-rays with atmospheric particles.

Depending on the primary particle, *air showers* can be of different nature. For electrons and γ-rays, the interactions are purely electromagnetic (electromagnetic showers) while for hadrons, e.g. the cosmic-ray protons, showers initiated by strong interactions with additional electromagnetic sub-showers will occur

(hadronic showers). Before giving more information about the general detection technique in Section 3.2 and the H.E.S.S. experiment in Section 3.3, the next section summarises the interaction processes and their properties that lead to the emission of Cherenkov light in air showers in the atmosphere. In Section 3.4, an overview of the H.E.S.S. analysis is given.

3.1 Air Showers

When a primary cosmic-ray particle enters the atmosphere, it interacts with an atmospheric atomic nucleus and induce a cascade of secondary particles, a so-called air shower. As mentioned above, depending on the nature of the primary particle, the air shower develops in a different way and shows different characteristics. In case of an electron or a γ-ray inducing the shower, it is of purely electromagnetic nature. In case of a hadron, strong and weak processes will occur alongside with electromagnetic interactions. In both cases, the kinetic energy of the primary particle is partially converted into kinetic energy of the secondary electrons, which typically have velocities greater than the speed of light in air and emit Cherenkov radiation. The number of particles starts to increase rapidly as the air shower moves downwards in the atmosphere. In each subsequent interaction, the particles lose energy and they are eventually not able to create new particles anymore. Finally, the shower will die out.

Electromagnetic Showers

In case of an electron or γ-ray as primary particle, its interaction with the atmospheric nuclei will lead to an electromagnetic cascade. The main processes here are *bremsstrahlung* and *pair production*. A VHE γ-ray photon converts into electron-positron pairs in the Coulomb field of an atmospheric nucleus (pair production) and these electrons and positrons get deflected by nuclei and emit photons via the bremsstrahlung process. The characteristic length scale for these interactions is the mean free path length X_0, which is the radiation length in the case of bremsstrahlung (i.e. the mean distance after which an electron has lost $1/e$ of its initial energy) and the conversion length for pair production. These two processes dominate the evolution of a shower along its axis while the lateral spread of a shower is dominated by Coulomb scattering off atmospheric nuclei.

Figure 3.1 illustrates this process in a simple model according to Heitler (1954). It assumes the mean free paths of all particles to be the same (i.e. radiation length = conversion length) and also divides the energy equally between all secondary particles. This model predicts the number of particles to increase exponentially at early stages, while the maximum number of particles is proportional to the energy of the primary particle. The production of new particles stops when the mean particle energy drops below $\sim$80 MeV, whereafter

the electrons loose their energy mainly through ionisation of air molecules. For a 1 TeV γ-ray, the shower maximum is at a height of on average $\sim$10 km. In electromagnetic showers, the secondary particles are emitted at angles close to the direction of the primary particle and radiate in a narrow cone around the trajectory of the primary particle.

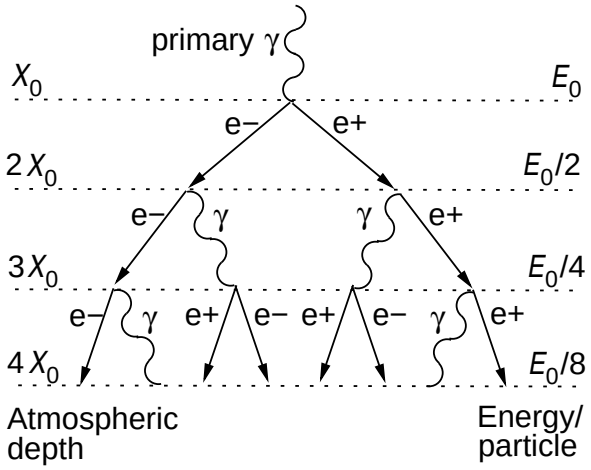

FIGURE 3.1: A simple model describing the evolution of an electromagnetic shower, according to Heitler (1954). Only bremsstrahlung and pair production are considered, and the mean free paths X_0 for these processes are assumed to be equal.

Hadronic Showers

When a cosmic-ray hadron, e.g. a proton, hits the atmosphere it scatters inelastically off atmospheric nuclei. This strong interaction produces mainly mesons like pions and kaons (as well as some nucleons and hyperons). About 30% of the particles generated in this first interaction are neutral pions, which almost instantly decay into two photons that produce electromagnetic sub-showers (see previous section). Thus roughly one third of the energy of the primary hadron goes directly into the electromagnetic component of the hadronic shower. From the decay of charged pions another large fraction of the energy is converted to long-lived muons and neutrinos, which will escape from the shower. The rest of the energy goes into the hadronic component of the shower.

Since the mean free path length for a proton is more than twice the mean free path length for an electron, hadronic showers generally penetrate significantly deeper into the atmosphere than purely electromagnetic showers. Since the secondary particles involved in strong interactions receive higher transverse momenta in their production, hadronic showers are far more spread out than

electromagnetic showers, in which the mean scattering angle is rather small. Additionally, due to the large amount of different particles that can be created, hadronic showers show larger fluctuations than electromagnetic showers. Note that as a result of the composition of the cosmic rays, hadronic showers occur much more frequently than γ-ray induced, purely electromagnetic showers ($\sim$ 1000 times more often). These showers form the background for the detection of VHE γ-rays.

Emission of Cherenkov Light in the Atmosphere

As the primary cosmic-ray particles inducing the air shower have very high energies, the secondary electrons will have enough kinetic energy that they will move with velocities greater than the phase velocity of light in the atmospheric medium. Under these conditions, charged particles will emit Cherenkov radiation. For pure electromagnetic showers, the secondary particles are emitted at angles close to the direction of the primary particle and radiate in a narrow cone around the trajectory of the primary particle and within a few nanoseconds, the superimposed light cones of all emitting shower particles will reach the ground in a circle of radius 80 – 150 m. Coulomb scattering of secondary particles will smear out the light distribution to some extent. As mentioned before, hadronic showers are more widely spread, suffer from large fluctuations due to the electromagnetic sub-showers and thus show irregular patterns in their light distribution. The difference in the Cherenkov light distributions on the ground for photon-induced and hadron-induced showers can be seen in Figure 3.2.

Due to absorption and scattering processes, not all Cherenkov light reaches the ground – for a primary 1 TeV γ-ray, about 100 Cherenkov photons/m^2 reach the ground at $\sim$ 2000 m above sea level.

This picture gets somewhat more complicated for observations at larger zenith angles. With increasing zenith angle, the Cherenkov light must traverse more atmosphere. On the one hand, this widens the Cherenkov radius on the ground significantly and thus leads to a larger effective detection area of the detector. On the other hand, the flux of photons does decrease and hence showers with lower primary energies will not be detected.

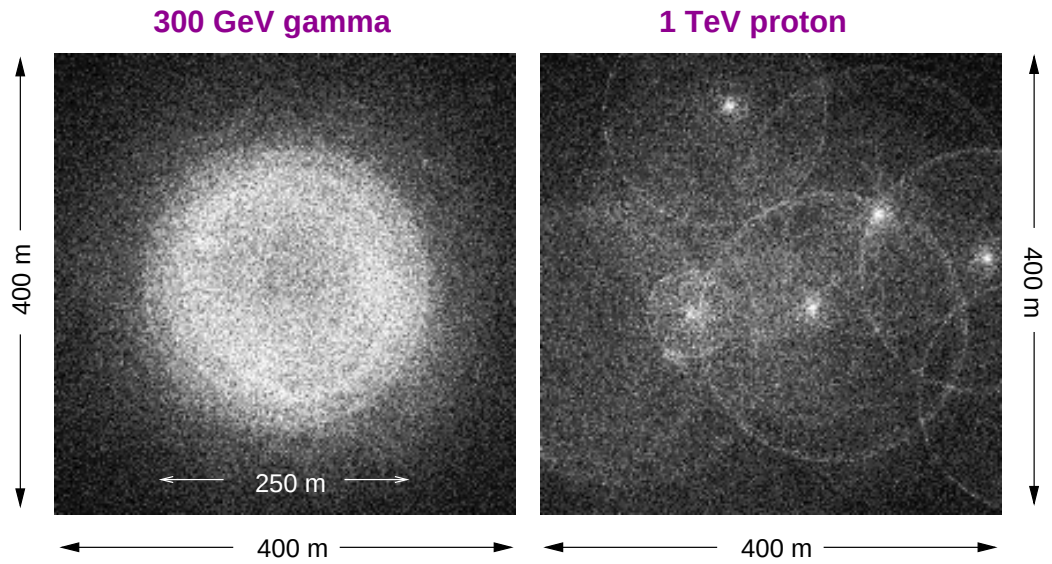

FIGURE 3.2: Simulated Cherenkov light distributions on the ground, with a 300 GeV γ-ray on the left and a 1 TeV proton on the right (by courtesy of K. Bernlöhr).

3.2 The Imaging Atmospheric Cherenkov Technique

The H.E.S.S. experiment is among the second generation instruments featuring the Imaging Atmospheric Cherenkov Technique (IACT).

The left panel of Figure 3.3 shows a schematic of the detection principle. An incident high-energy γ-ray interacts with particles high up in the atmosphere and generates an air shower of secondary particles which emit Cherenkov light. A telescope located within the light pool can detect the air shower, which gives an effective detection area of a Cherenkov telescope of about 50000 m^2, a huge number compared with the sub-m^2 detection areas of satellite instruments.

In the right panel of Figure 3.3, a schematic of the imaging of a shower onto the telescope camera is shown. As can be seen by the positions of the shower end points X and Y, the angle under which the elliptical emission region is observed determines the length of the image in the focal plane (i.e. the camera), while the distance on ground between the shower and the reflector determines the position of the image. The lateral extent of the shower determines the width of the image, which is the primary background rejection parameter as it allows to distinguish between electromagnetic and hadronic showers (which are more widespread).

Figure 3.4 shows in the left panel a schematic explaining some basic dependencies between showers and camera images. The image axis, the straight line connecting X and Y, points towards the direction of the primary γ-ray and can

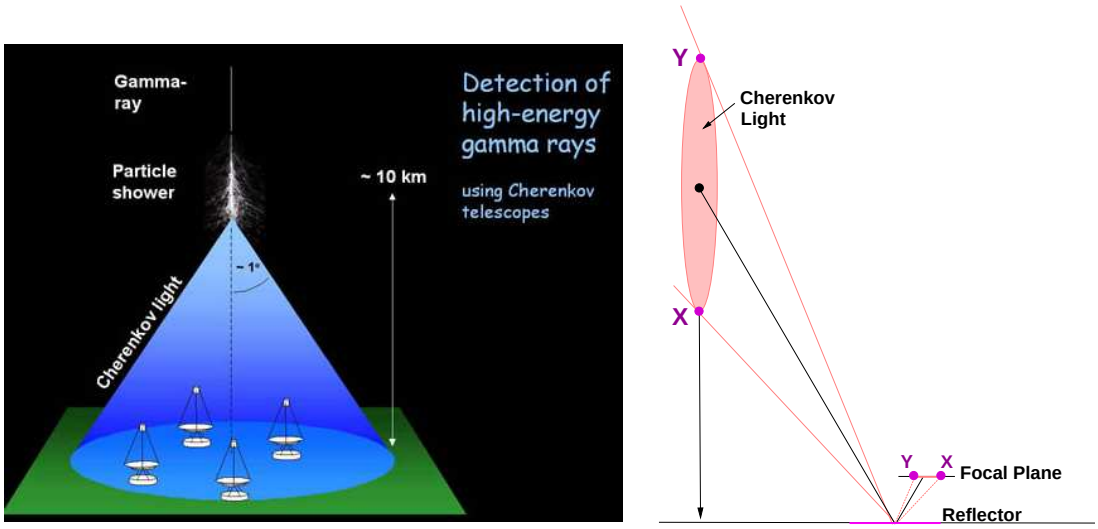

FIGURE 3.3: *Left*: The Imaging Atmospheric Cherenkov Technique used to detect Cherenkov light from air showers generated by very-high-energy particles in the atmosphere (picture by W. Hofmann). *Right*: Schematic showing the basics of the detection of a shower with a Cherenkov telescope. The mirrors reflect light that was emitted under same angles to same positions in the focal plane. The points X and Y are also used in Figure 3.4 to compare with camera pictures.

be used to reconstruct the impact point of the γ-ray on the ground. The right panel of Figure 3.4 displays an image obtained with the first H.E.S.S. telescope in 2002. The picture shows the track of the air shower (image axis), which points back to the celestial object where the incident γ-ray originated from (note that here the telescope was not pointing directly at the source, therefore the image axis does not cross the camera centre). The intensity of the image is a measure for the energy of the γ-ray.

From a single image of a shower it is difficult to distinguish whether the shower developed from X to Y or vice versa, though it is possible to estimate it from the image shape. Therefore, multiple telescopes are used which observe the shower from different directions and allow for a stereoscopic reconstruction of the shower geometry. This has the advantage in that the angular resolution improves significantly.

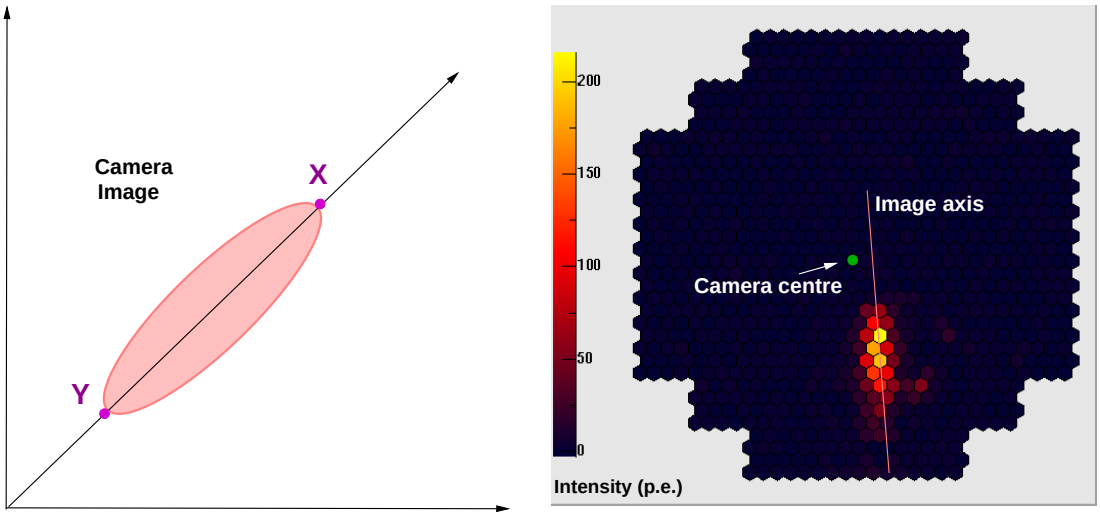

FIGURE 3.4: *Left*: Schematic of a camera image, points X and Y according to Figure 3.3. *Right*: H.E.S.S. camera image recorded with the first H.E.S.S. telescope in 2002. Note that the image axis does not cross the camera centre, thus the telescope was not pointing directly to the source.

3.3 The H.E.S.S. Experiment

H.E.S.S. is a system of Imaging Atmospheric Cherenkov Telescopes designed for the investigation of cosmic γ-rays in the VHE range (Figure 3.5). H.E.S.S. stands for **H**igh **E**nergy **S**tereoscopic **S**ystem, but is also intended to pay tribute to Victor Hess, who received the Nobel Prize in Physics in 1936 for his discovery of the cosmic radiation.

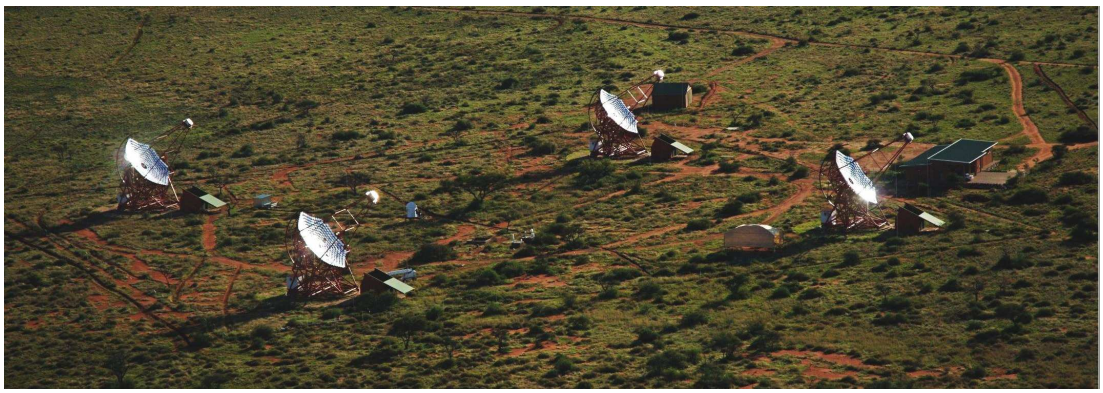

FIGURE 3.5: The H.E.S.S. Telescopes Array.

The H.E.S.S. system is currently the most sensitive instrument for γ-ray astronomy in its energy regime. The instrument is an array of four 13 m diameter telescopes located in the Khomas highland of Namibia (23°16′18″ South, 16°30′00″ North). The initial four H.E.S.S. telescopes (Phase I) are positioned at the edges of a square with 120 m side length to provide multiple stereoscopic views of air showers. The spacing of the telescopes was optimised for a maximum sensitivity at the planned threshold of 100 GeV. The system has an angular resolution better than 0.1° per single γ-ray, an energy resolution of ∼15 % and a point-source sensitivity of $< 2.0 \times 10^{-13}$ cm^{-2} s^{-1} (1 % of the flux from the Crab nebula) for a 5 σ detection in 25 hours of observation (Aharonian et al., 2006c).

The first of the four telescopes of Phase I of the H.E.S.S. project went into operation in summer 2002. Since December 2003, all four are operated routinely (see Hinton (2004) for an overview of the H.E.S.S. project). In Phase II of the H.E.S.S. project, scheduled to be completed in 2008, a single huge dish with about 600 m^2 mirror area will be added at the center of the array, further increasing the energy coverage, sensitivity and angular resolution of the instrument.

Telescopes

The H.E.S.S. telescopes (mount and dish) are steel structures with a weight of 60 tons each. The dishes have a Davies-Cotton style hexagonal arrangement of facets (Davies and Cotton, 1957), with a total diameter of ∼13 m (composed of 382 round mirrors with a diameter of ∼60 cm each) and a total mirror area of ∼107 m^2. The cameras recording the reflected Cherenkov light are located in the focal plane, at ∼15 m distance from the mirror dish.

Cameras

The H.E.S.S. cameras were designed to fulfill the following criteria: a small pixel size to resolve image details, a large field of view to allow observations of extended sources and surveys, and a triggering scheme which allows the identification of the very short (in time) and compact Cherenkov images over the optical background light from the night sky.

Each camera consists of a hexagonal array of 960 photo-multiplier tubes (PMTs). The PMTs are equipped with Winston cones to funnel the light into the PMTs, which gives an essentially gap-less focal plane. Each of the PMTs corresponds to an area of 0.16°, which gives a total field of view of the detector of 5° in diameter on the sky (∼10 times the diameter of the moon). Each camera is of modular design, using 60 *drawers* of 16 tubes each, which contain the trigger and readout electronics and the high voltage supply for the PMTs, as well as the monitoring of the electronics. The rear part of the camera houses power supplies and crates with interfaces to the digital readout bus, a CPU and to the trigger processors. Each camera weighs about 800 kg. For more details see Vincent et al.

(2003).

A prototype Cherenkov camera designed for the next generation of Imaging Atmospheric Cherenkov Telescopes was developed at the Max-Planck-Institute for Nuclear Physics (MPIK). In the scope of this work, parts of the driver and analysis software for the prototype was developed and tested, and first tests of the functionality of the prototype were performed to establish a basis for more detailed testing. As future systems will aim for lower energy thresholds on the order of a few GeV and an increase in sensitivity up to energies of about 100 TeV, these telescopes will need to have large mirrors. This will lead to significantly higher trigger rates and thus the amount of data to be processed will be much larger. As H.E.S.S. has shown the stereoscopic reconstruction of Cherenkov showers to be a very successful approach, it is likely that future systems will consist of several telescopes. Therefore the cameras have to be designed with regard to reduction of costs and easy maintenance. The camera developed at the MPIK was designed to fulfill these requirements. Details of the performance and design characteristics are given in Appendix A.4.

Trigger

The H.E.S.S. array trigger system consists of three levels: the first requirement is the detection of 4 photo-electrons within a time span of 1.5 nanoseconds in a single PMT. The second level requires 3 triggered PMTs within a *sector* (a square group of 64 PMTs) in order to trigger a telescope. Finally, since H.E.S.S. uses stereoscopic reconstruction of air showers to determine the direction as well as the type and the energy of the primary particle, the *central trigger system* receives trigger signals from the individual telescopes and searches for coincidences between telescopes, requiring a minimum coincidence of 2 telescopes to trigger at the same time. This requirement reduces the amount of data to be read out, therefore the trigger threshold can be lowered for a given dead time, leading to a lower energy threshold. The H.E.S.S. trigger system and its performance is described in Funk et al. (2004).

The unprecedented sensitivity of the H.E.S.S. telescopes combined with their large field of view allowed for the first time to image a large section of the Milky Way in VHE γ-rays (Aharonian et al., 2005b, 2006e), shown in Figure 3.6.

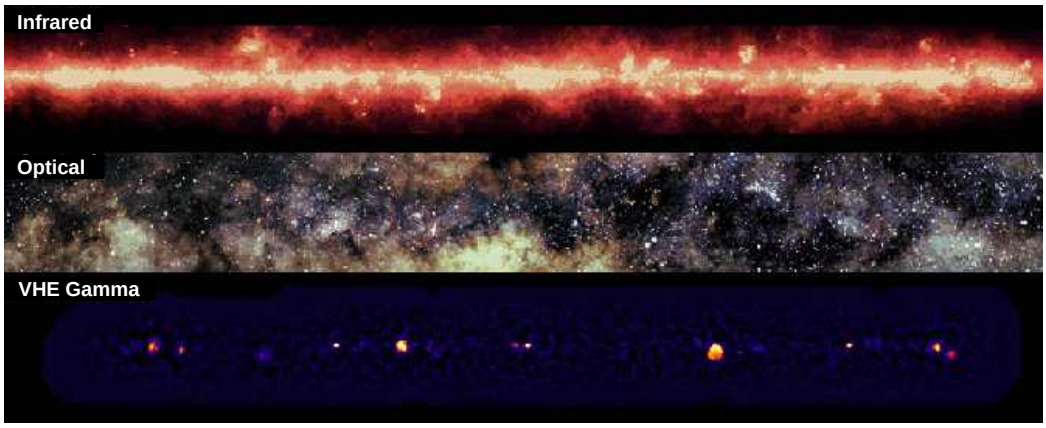

FIGURE 3.6: The central Milky Way in infrared, optical and VHE γ-ray wavelength (Infrared image: S.L. Wheelock et al.; Optical image: A. Mellinger).

3.4 The H.E.S.S. Analysis

This chapter gives an overview of the standard H.E.S.S. analysis. After a short discussion of H.E.S.S. data-quality selection criteria and systematic uncertainties the steps of the H.E.S.S. analysis are introduced, from image cleaning to the generation of energy spectra, following Aharonian et al. (2006c), in which a detailed account of the H.E.S.S. analysis is given and tested on the Crab nebula.

3.4.1 Data Quality and systematic Uncertainties

The connection between the energy of the primary particle and the image in the camera, i.e. the image of the Cherenkov light from the induced air-shower, has to be understood to ensure the correct measurement of the energy of the primary particle. For this purpose, Monte Carlo simulations of air showers are used to predict the sizes and shapes of the images of primary particles according to their energy and to the shower position relative to the observer. However, due to variations in the atmosphere, in the response of the cameras and in the optical response of the whole instrument, there remain uncertainties in the measured showers, particularly in the intensity of the images.

Data Quality Selection

The atmosphere is subject to changes in density, temperature, pressure and humidity. With variations in the atmosphere the detector response can change. Cherenkov light can be also absorbed due to dust and clouds. It has to be assured that observations are taken under good and stable conditions to avoid systematic effects on the measured flux. Variations in the atmospheric conditions

will mostly lead to fluctuations in the trigger rate of the system, and therefore the most important quality criterion is that the system trigger rate remains stable throughout the run. This is done by cutting on the absolute value and the RMS of the trigger rate. Figure 3.7 shows the difference between a run passing this selection (left) and a run failing (right), taken from Aharonian et al. (2006c).

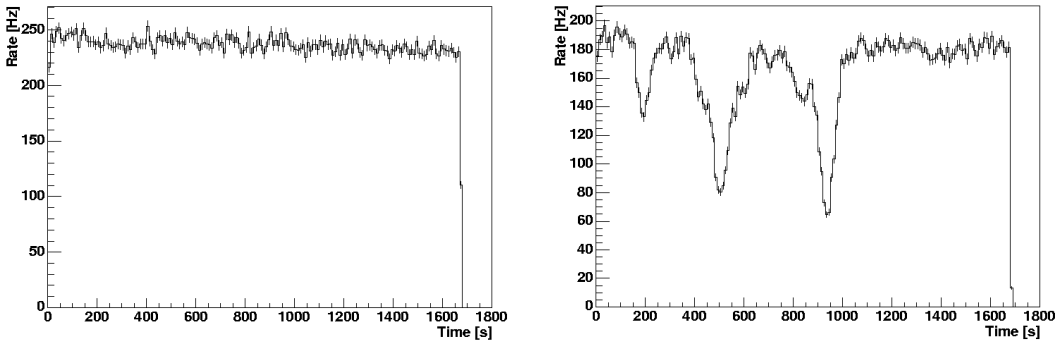

FIGURE 3.7: The system trigger rate versus time. *Left*: A 4 telescope run passing the selection. *Right*: A 3 telescope run failing the selection. The run fails due to clouds passing through the field of view, which result in drops in the trigger rate. The absolute value for the trigger rate is lower in the rejected run as less telescopes participated in this run and it was taken at larger zenith angles. Picture taken from Aharonian et al. (2006c).

Another important effect is that bright stars, meteorites, lightning etc. in the field of view will cause single PMTs to be turned off. Telescopes with more than $\sim$10% of the PMTs missing are excluded from the analysis. The tracking system of the array is also monitored to avoid possible errors in the reconstructed source position (and thus on the flux).

Camera Response

The camera response is given by the single photo-electron (p.e.) response and the quantum efficiency of each PMT as well as the reflectivity of the Winston cones (see Section 3.3). These and other effects are corrected for in the calibration of the H.E.S.S. telescopes, which is described in detail in Aharonian et al. (2004b).

Optical Response of the Instrument

The optical response of the system degrades continuously as, e.g., the reflectivity of the mirrors diminishes with time. This effect should be considered when dealing with fluxes from VHE γ-ray sources as it reduces the image intensity and hence

the estimated energy for each event, compared to the intensity expected from Monte Carlo simulations for a system with a better optical response.

This is corrected for by applying a scaling factor in the energy estimation for each event. The scaling factor is the ratio of the optical efficiency of a telescope for the run to the optical efficiency expected from Monte Carlo simulations. It was found in further studies that applying this factor to the image intensity, as it is stated in Aharonian et al. (2006c), leads to an overcorrection of the optical efficiency. Therefore the scaling factor is now applied directly to the energy of each event.

The optical efficiency of a telescope can be determined by measuring single muons, which are byproducts of hadronic showers and the main background for single telescopes. Muons produce ring-shaped images, which differ greatly from air-shower images and thus are easy to identify. It is possible to precisely calculate the number of Cherenkov photons a muon emitted based on a few geometrical parameters of its observed Cherenkov emission. These parameters are derived by fitting the theoretical intensity distribution to the observed intensity distribution in the image. Using this procedure, the number of photons that should have reached the camera can be reconstructed, and the efficiency can be given as the ratio of photo electrons in the camera to expected photons, $\epsilon = \mathrm{N_{p.e.}}/\mathrm{N_{\gamma}}$. See Bolz (2004) for detailed studies on the optical efficiency.

In Figure 3.8 an example of the influence of the optical efficiency correction on the photon spectrum is discussed by the example of the spectrum of the new source HESS J1809−193, which is discussed in Chapter 6.

The upper panel shows the spectrum with (black) and without (red) taking the degradation of the optical response of the system into account. Both spectra are well fit by a power law ($dN/dE = N_0(E/E_0)^{-\Gamma}$). For the corrected spectrum, a photon index $\Gamma = 2.2 \pm 0.1_{\mathrm{stat}} \pm 0.2_{\mathrm{sys}}$ and a differential flux normalisation at 1 TeV $N_0 = (4.6 \pm 0.6_{\mathrm{stat}} \pm 1.4_{\mathrm{sys}}) \times 10^{-12}\,\mathrm{TeV}^{-1}\,\mathrm{cm}^{-2}\,\mathrm{s}^{-1}$ is derived , and the fit has a $\chi^2/d.o.f. = 6.9/5$. The integral flux between $(1 - 10)$ TeV is about 14 % of the flux of the Crab nebula in the same energy range. Without this correction the energy of the events is underestimated, leading to the red spectrum. As expected, the correction leads to a shift in the energy without changing the index of the power law. Note that the uncorrected spectrum is also shifted to lower energies, however, for comparison the same binning is chosen for both spectra. The fit to the uncorrected red spectrum has a photon index $\Gamma = 2.2 \pm 0.1_{\mathrm{stat}} \pm 0.2_{\mathrm{sys}}$ and a differential flux normalisation at 1 TeV $N_0 = (2.4 \pm 0.4_{\mathrm{stat}} \pm 0.7_{\mathrm{sys}}) \times 10^{-12}\,\mathrm{TeV}^{-1}\,\mathrm{cm}^{-2}\,\mathrm{s}^{-1}$ and gives a $\chi^2/d.o.f. = 7.9/5$ [1]. Its integral flux between $(1 - 10)$ TeV is about 7 % of the flux of the Crab nebula in the same energy range. In the lower panel of Figure 3.8, the distribution of the scaling factors applied to the energy of the events is shown. The distribution

[1] Note the large systematic error on the flux normalisation – the overall effect on the flux may be exaggerated.

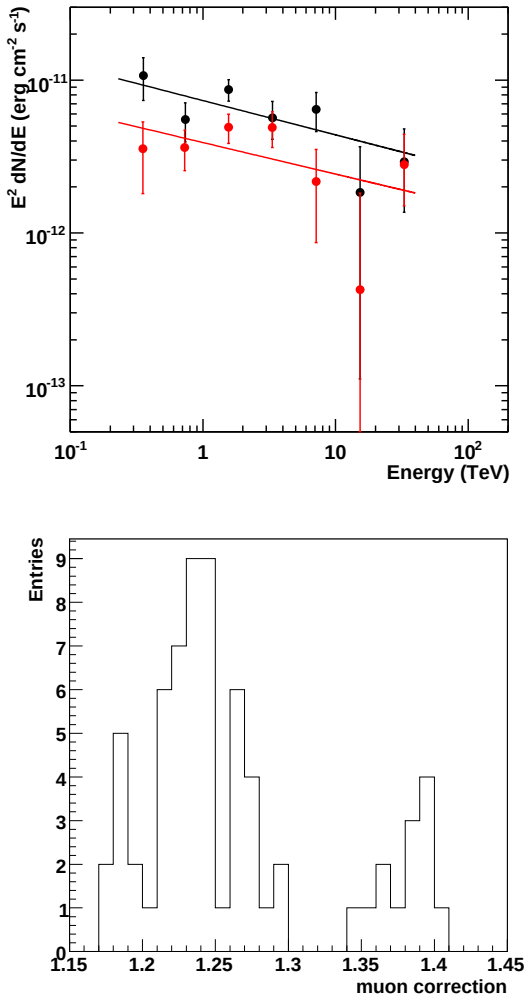

FIGURE 3.8: *Top:* The energy spectrum of HESS J1809−193 with (black) and without (red) correction for the degradation of the optical response of the system with time. *Bottom:* Distribution of the scaling factors applied to the energy of the events, with a mean of 1.26 and an RMS of 0.06.

ranges from 1.18 – 1.41, with a mean of 1.26 and an RMS of 0.06.

3.4.2 The standard H.E.S.S. Analysis

Image Cleaning, Moment Analysis & Stereo Reconstruction

After the run selection, the next step in the analysis is the *image cleaning* to remove noisy pixels containing mainly night sky background, and to select the pixels with Cherenkov light. For this purpose a two-level filter is used, requiring

pixels in the image to be above a threshold of 5 p.e. and to have a neighbour above 10 p.e., and vice versa. This results in a selection of spatially correlated features in an approximate ellipse shape in the case of a γ-ray and of more wide and uneven features in the case of a hadron. For each cleaned image, *Hillas* parameters are calculated, which are based on the second moments of the image (hence *moment analysis*) and which are the basis for selecting γ-ray like events (Hillas, 1985). Figure 3.9 illustrates these parameters (image taken from Aharonian et al. (2006c)).

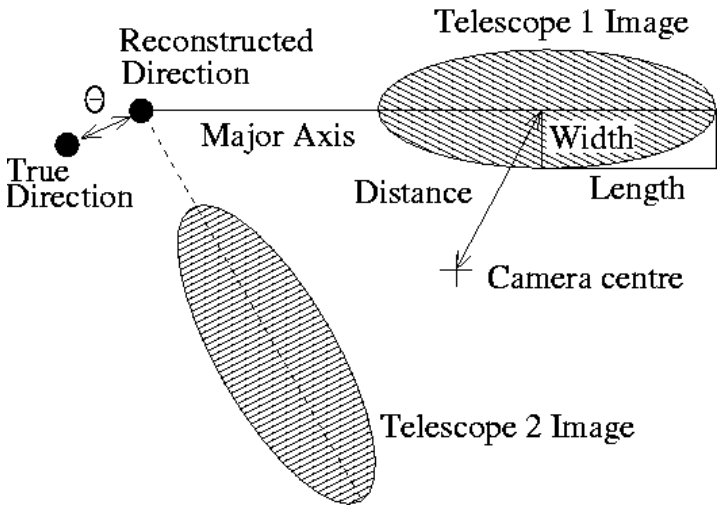

FIGURE 3.9: Hillas parameters for a γ-ray image, which can be approximated as an ellipse. The width and length of the ellipse and the distance of the centre of the ellipse from the camera centre are used for the event selection. With a second image of the event from another participating telescope, the direction of the event can be reconstructed. The angular offset from the reconstructed event (shower) position is θ. Image taken from Aharonian et al. (2006c).

Superimposing images from several telescopes in one field of view and intersecting the major axes of all images (see Figure 3.9), the direction of the primary particle can be found (*stereo reconstruction*). For this estimation, only images which are well inside the camera and which are of sufficient intensity are used. The accuracy in the reconstruction of arrival directions defines the *point spread function* of the instrument; at observation angles near zenith the H.E.S.S. point spread function is $\sim 0.1^\circ$. Finally, to allow for an accurate measurement of the total light yield in the shower and thus the energy of the primary particle, the impact point of the original particle track on the ground has to be reconstructed. The error on this reconstruction is currently less than 10 m for showers within 200 m of the centre of the array.

Scaled parameter analysis

To decide whether an event is γ-ray like or hadron-like and thus suppress the background, a cut on the *mean reduced scaled width / length* is applied. First, the *mean scaled width / length* of an image is calculated. The width w derived from the shower image as shown in Figure 3.9 is compared to the expected values from simulations of the mean width $\langle \mathrm{w} \rangle$, in units of the standard deviation σ_{w}. This is done for a real and simulated γ-ray with the same light yield (amplitude) in the camera, impact distance, zenith angle of the shower and offset of the shower from the pointing position:

$$\mathrm{w_{sc}} = (\mathrm{w} - \langle \mathrm{w} \rangle)/\sigma_{\mathrm{w}}. \tag{3.1}$$

By averaging over all participating telescopes, the mean reduced scaled width is derived. The same procedure is applied to the length derived from the shower image to calculate the mean reduced scaled length.

Selection cuts

For different sources with typical fluxes and energy spectra the selection cuts on the scaled parameters, image amplitude and squared angular distance to the camera centre (θ^2) have to be simultaneously optimised to maximise the detection significance. For example, *standard cuts* are optimised for point sources with a flux of 10% of the Crab flux and a similar spectrum (index $\sim$2.6). *Hard cuts* are optimised for point sources with 1% flux of the Crab flux and harder spectra (index $\sim$2.0). See Aharonian et al. (2006c) for details of the optimisation process and the different cuts.

3.4.3 Background Estimation

When trying to extract a signal from a certain position in the sky, it is essential to determine the underlying background level of non γ-ray events. Different approaches to background modelling are possible, each of which have different strengths and weaknesses. Once an estimate for the background is obtained, the significance of the excess can be calculated using the likelihood ratio method described by Li and Ma (1983).

For any approach, at first the reconstructed signal for all γ-ray like events is filled in a map, from which the *on* events for a position are calculated in a circle around that position with radius θ. To derive the background level for the same field of view several methods can be used; two of the widely used methods are illustrated in Figure 3.10 and the three methods used in this work are described in the following. For all methods it is important to avoid contamination of the background region by a γ-ray signal, which is why *exclusion regions* are

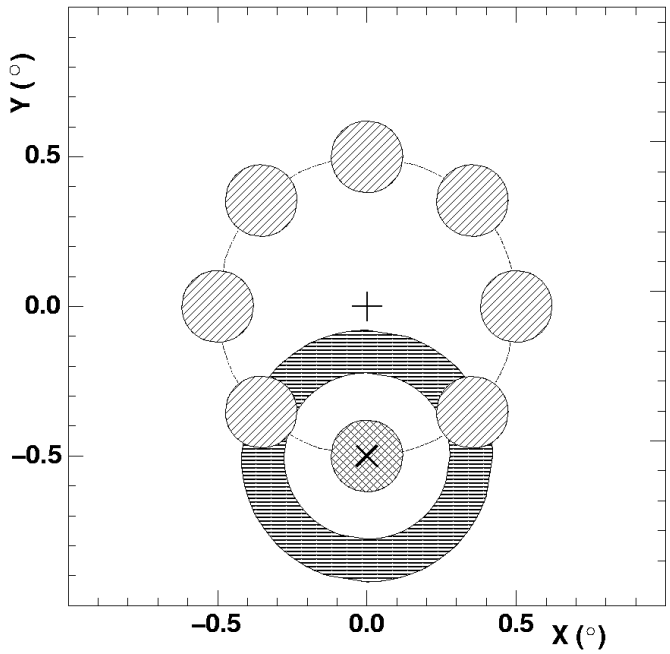

FIGURE 3.10: The background regions for two different methods: the *reflected-background* regions filled by diagonal lines, the *ring-background* region filled by horizontal lines and the *on* region filled cross hatched. The cross marks the observation position. Image taken from Aharonian et al. (2006c)

defined around all known γ-ray sources so that they are henceforth excluded in the estimation of the background level.

The *reflected background* method uses regions equidistant from the observation position, at the same distance as the *on* region. These regions are shown as circles filled with diagonal lines in Figure 3.10. Summing up the events from these regions and scaling for the difference in areas used for the background and signal determination, the background at the *on* position can be estimated. As all regions are at the same distance from the centre of the field of view, all have the same radial background acceptance. This method is ideal for flux measurements and for deriving spectra.

The *ring background* method calculates the background for each position in the field of view by determining the background rate in a ring surrounding that position, shown as the region filled with horizontal lines in Figure 3.10. The width of the ring is chosen so that the area in the ring is $\sim$7 times larger than the area of the *on* region. Here, the change of the radial background acceptance in the camera has to be taken into account by adding a weight factor to the normalisation of the *on* and background region areas. As the background acceptance might change with energy, it cannot be ensured that the background level is correctly

determined for the whole energy range of the spectral analysis and thus this method is not used to derived spectra.

Instead of the *reflected background* method, the *on/off background* method is used for the spectral analysis of sources where the observation position is within the *on* region or for very large sources, as in both cases the background regions cannot be taken from the same field of view. In the case of many sources in the field of view, the background regions may all end up at one side of the source, leading to systematically different zenith angle distributions for the *on* and *off* regions. This method has a powerful advantage in that no assumption is made for the system acceptance (except it being the same for both). As some fields observed by H.E.S.S. contain no significant γ-ray signal, these data can be used as *off* runs. For a given set of *on* runs, a set of *off* runs matching in zenith angle is selected. The normalisation between *on* and *off* runs is derived from the number of events in the runs, excluding the nominal γ-ray source.

A detailed description of the above-mentioned methods for background estimation and more can be found in Berge et al. (2007).

3.4.4 Energy Reconstruction, Flux Measurements and Spectrum

From lookup tables generated from Monte Carlo simulations, the estimate of the energy of the primary particle inducing a γ-ray shower can be obtained from its integrated image amplitude and the impact parameter on the ground.

To estimate the γ-ray flux from a source, the excess events and the *effective area* of the instrument have to be known. The effective area depends on zenith angle, offset, energy and selection cuts and is modelled from Monte Carlo simulations. It can be either estimated as a function of the energy of Monte Carlo events, which does not depend on the spectrum of the simulated γ-rays, or as a function of the energy of reconstructed events, which due to finite energy resolution does depend on the spectral index of the simulation. See Aharonian et al. (2006c) for more details.

When deriving an energy spectrum, the energy bin size is set depending on the overall significance of the signal. The differential flux in each energy bin is derived by summing over the events from the *on* region, N_{on}, weighted by the inverse of the effective area A (which is a function of the reconstructed energy). From this, the normalised sum of all events from the background regions, N_{off}, is subtracted. This difference is then weighted by the live time T for that bin and by the bin width in energy, $\Delta \mathrm{E_i}$:

$$\frac{dF_i}{dE} = (\mathrm{T}\Delta\mathrm{E_i})^{-1} \cdot \Big\{ \sum_{j=0}^{Non} (\mathrm{A}_j)^{-1} - \alpha \sum_{k=0}^{Noff} (\mathrm{A}_k)^{-1} \Big\}. \tag{3.2}$$

The systematic error on the absolute flux depends on various contributing factors

and adds up to 20%. For more details on sources of errors and the H.E.S.S. analysis in general see Aharonian et al. (2006c).

Chapter 4

Data Set, Pulsar Sample and First Results

H.E.S.S. was the first instrument to allow for deep surveys of the Galactic plane in VHE γ-rays and has discovered a large number of VHE γ-ray sources in these surveys. Of the new sources a significant quantity can be identified as pulsar wind nebulae (PWNe), the extended relativistic outflows of pulsars. Though PWNe represent to date the most populous class of Galactic sources in VHE γ-rays, the details of the energy conversion mechanisms in the vicinity of pulsars are not well understood and it is not known which pulsars are able to drive PWNe and produce VHE radiation. This motivates the systematic study of a connection between pulsars and VHE γ-ray sources. It is investigated how the probability to detect in VHE γ-rays PWNe surrounding known pulsars varies with the spin-down energy flux $\dot{E}/d^2$ of the pulsar, testing the plausible assumption that the VHE γ-ray output of a PWN somehow correlates with the power of the pulsar feeding it.

A large data set in VHE γ-rays is provided to search for a connection between pulsars and VHE γ-ray sources, which is described in Section 4.1, along with some tools used in the search. In Section 4.2 the pulsar survey is introduced, from which the pulsar sample for the search is taken, as well as the pulsar sample itself. In Section 4.3 first results from the search are presented.

4.1 H.E.S.S. Data Set

The VHE γ-ray data set used to search for γ-ray emission near the location of known radio pulsars comprises all data used in the H.E.S.S. Galactic plane survey (Aharonian et al., 2005b, 2006e), including an extension of the survey to Galactic longitudes -60 deg $< l < -30$ deg, dedicated observations of Galactic targets and re-observations of H.E.S.S. survey sources. The search covers a range in Galactic longitude from -60 deg to 30 deg while the range in Galactic latitude is

restricted to ±2 deg, a region well covered in the survey. In total, 1436 runs with a live time of ∼658 hours were used, which were taken at a mean zenith angle of 30.1 deg.

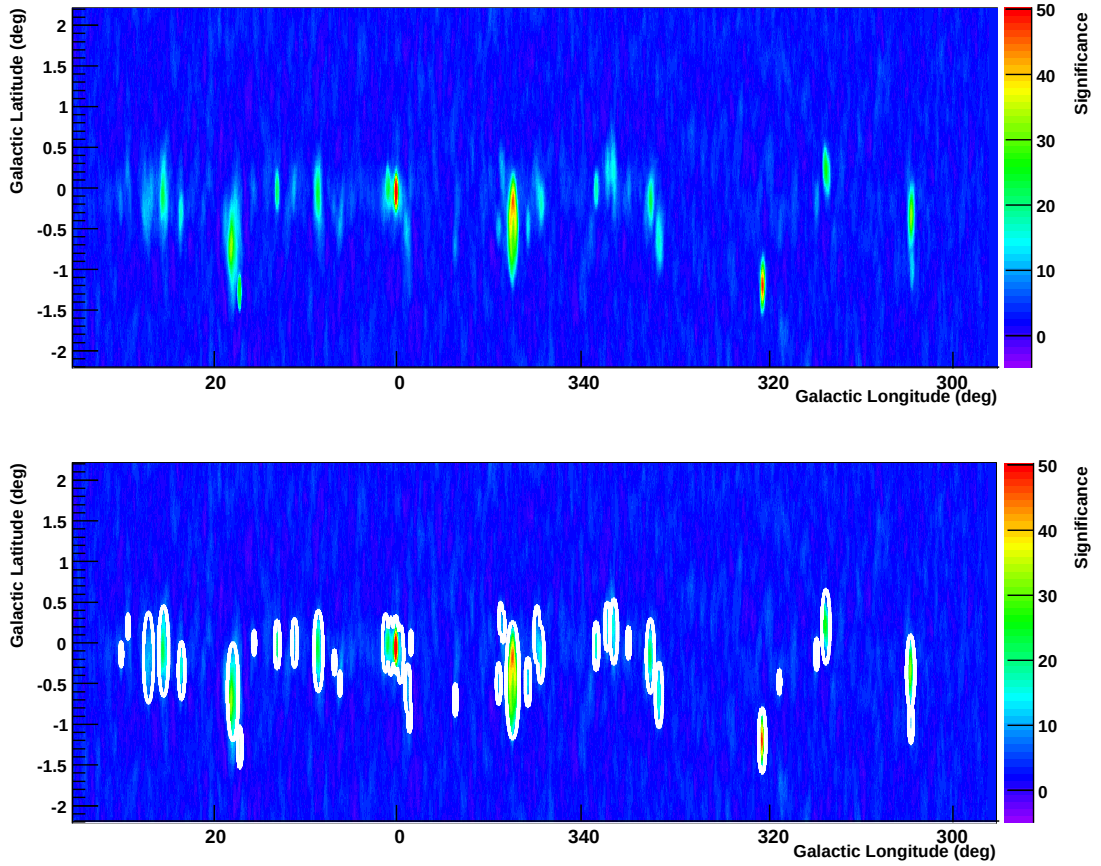

FIGURE 4.1: *Top:* H.E.S.S. significance map of the search region. *Bottom:* Exclusion regions overlaid as contours on the H.E.S.S. significance map.

The analysis of the γ-ray data follows the standard H.E.S.S. analysis (see Section 3.4). To provide the significance of a γ-ray signal at any position in the search region, a sky map for the whole search region has to be generated. This map is shown in Figure 4.1. The signal for each position in the map is obtained by counting the number of events N_{on} in the circular *on* region centred on this position with radius θ and comparing it to the number of background events αN_{off} in a ring around this position. α is a normalisation factor, which accounts among others for the difference in solid angle for N_{on} and N_{off} and for the variation of the acceptance for γ-ray showers within the field of view as well as with zenith angle and exposure time. It is important to avoid contamination of the background region by a γ-ray signal, which is why exclusion regions are

defined around all known γ-ray sources and these regions are excluded in the estimation of the background level. The exclusion regions are drawn as contours on top of the sky map in the lower panel of Figure 4.1. Knowing N_{on}, α and N_{off}, one can determine the significance of a signal above background for each position, using the approach by Li and Ma (1983). For a more detailed description of the production of big sky maps used in the analysis of the surveys of the Galactic plane see Funk (2005).

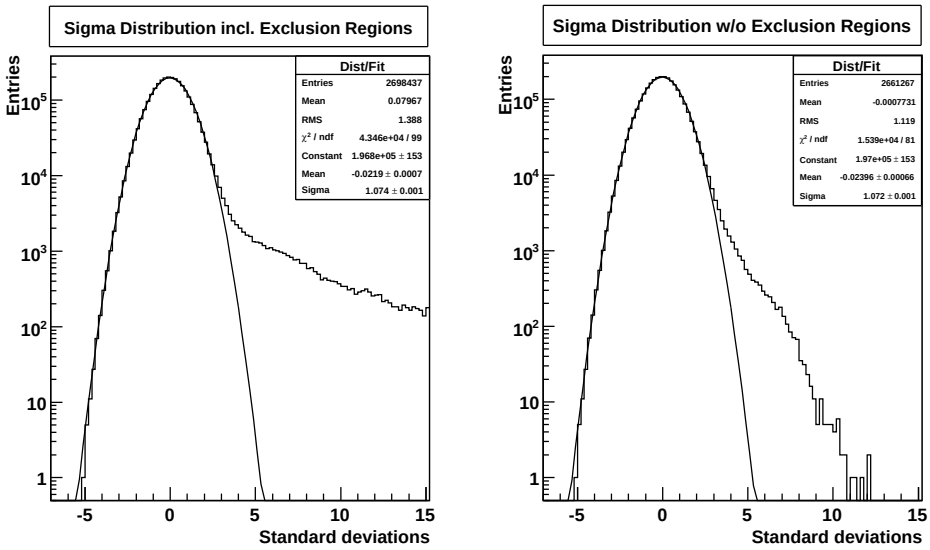

FIGURE 4.2: H.E.S.S. significance distributions including significances from exclusion regions (*left*) and without significances from exclusion regions (*right*), both fit with a Gaussian. The negative sides of the distributions follow the expected Gaussian distribution, while even after defining exclusion regions (*right*), some excess can be seen on the positive side, indicating that the exclusion regions were chosen too small.

In Figure 4.2, significance distributions for the sky map shown in Figure 4.1 are displayed. In the left panel, significances from exclusion regions (i.e. known γ-ray sources) are included, leading to a clear excess on the positive side of the distribution, while the negative side follows the expected Gaussian distribution. In the right panel, the significance distribution without significances from exclusion regions is shown. There is still some excess on the positive side, however, in comparison to the distribution in the left panel, where $\sim$1% of all entries lie above 5 standard deviations, here there are only $\sim$0.1% of all entries left above 5 standard deviations. The leftover excess indicates that some of the exclusion regions were chosen too small. There might be also other emission in the field of view that is not excluded. The contamination of the background with some signal may lead to lower significance estimates in the sky map. However, the pos-

sible underestimation of the significances should have no significant effect on the results of the analysis, as the same sky map is used to look up the significances for both the real pulsars and the simulated sample (see Chapter 7).

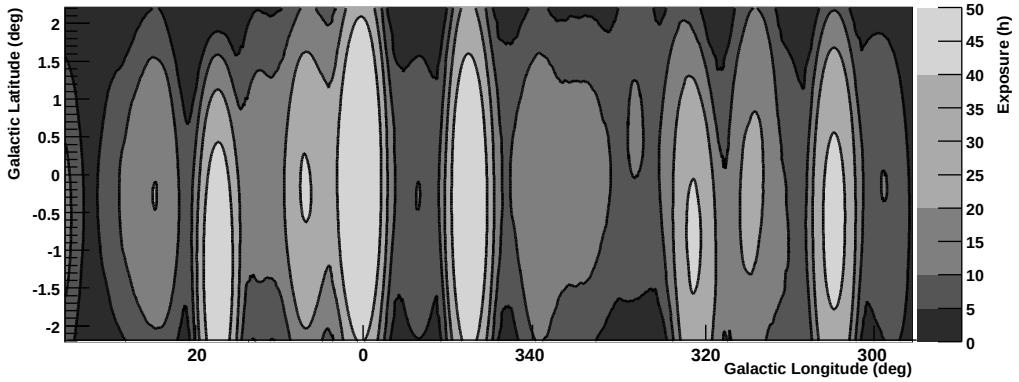

FIGURE 4.3: H.E.S.S. exposure map of the search region. The exposure is given in equivalent on-axis hours, accounting for the decrease of detection rate at larger distances from the telescope axis.

Taking into account the properties of known γ-ray PWNe, for the sky maps used in this work the search for emission is optimised for slightly extended sources – on the scale of the angular resolution (≈ 0.1 deg) of the H.E.S.S. telescopes – and allows for small offsets of the VHE emission from the pulsar positions. Each excess is determined by counting γ-ray candidate events ($N_{\rm on}$) within $\theta \leq 0.22$ deg ($\theta^2 \leq 0.05$ deg^2) of a given position and subtracting a background estimated from a ring surrounding this position with a mean radius 0.6 deg and a width scaled to provide a background area $\sim$7 times larger than the area of the on-source region. The size of the *on* region is the standard size when searching for extended sources in H.E.S.S. data (see Aharonian et al. (2005b)). Figure 4.3 shows the exposure map for the search region. The exposure is given in equivalent on-axis hours, accounting for the decrease of detection rate at larger distances from the telescope axis; note that the scale is truncated at 50 hours of exposure. All positions in the search have exposures of at least one hour and it can be seen from Figure 4.3 that most parts of the search region have been observed for at least five hours.

4.2 Pulsar Data Set: ATNF & PMPS

The Australia Telescope National Facility (ATNF) operates the Australia Telescope, a set of eight individual radio telescopes, located at three sites in New South Wales. The Australia Telescope also includes the Parkes 64-metre radio

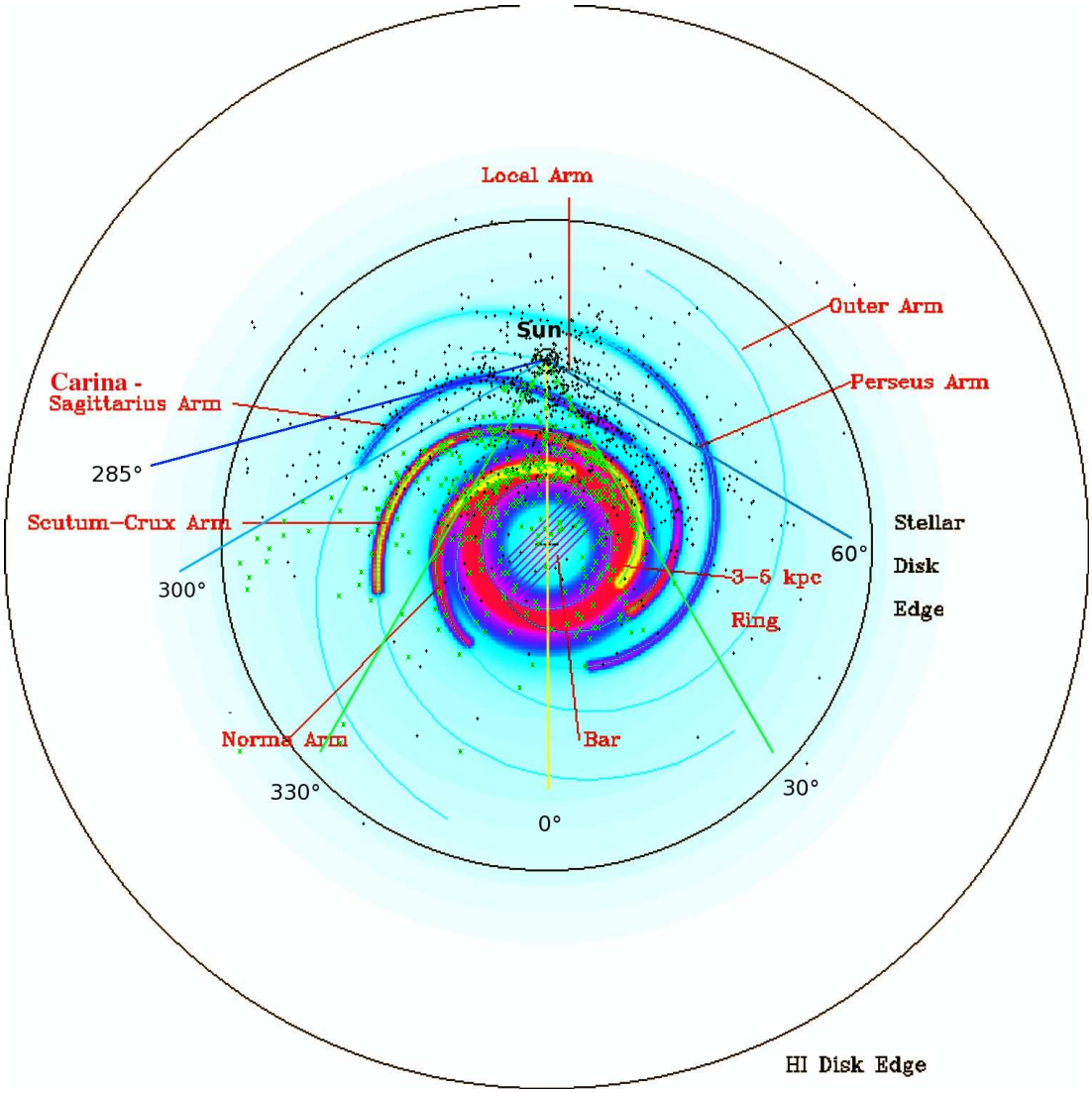

FIGURE 4.4: Schematic plan view of the Milky Way with all ATNF pulsars (black crosses) and the selected PMPS search sample (green crosses) (by courtesy of K. Bernlöhr, based on an artwork of the Canadian Galactic Plane Survey).

telescope, which has been successfully operated since 1961.

The pulsar locations to be tested were taken from the Parkes Multibeam Pulsar Survey (PMPS, see Hobbs et al. (2004) and references therein), as recorded in the ATNF pulsar catalogue[1] (Manchester et al., 2005). Figure 4.4 shows a schematic plan view of the Milky Way based on artwork of the Canadian Galactic Plane Survey[2]. The positions of all ATNF pulsars are overlaid as black crosses,

[1] http://www.atnf.csiro.au/research/pulsar/psrcat/
[2] http://www.ras.ucalgary.ca/CGPS/

while the positions of the selected PMPS pulsars for the search (see below for the selection criteria) are indicated as green crosses. A large fraction of the selected PMPS pulsars seem to cluster around the Norma and the Scutum-Crux arm.

The PMPS uses a 13-element receiver operating at a frequency of 1400 MHz. This receiver allows 13 regions of the sky to be simultaneously observed, improving the speed of surveys by the same factor. To date, the PMPS has discovered 743 pulsars and detected 1030 pulsars in total. Figure 4.5 shows in the left panel the distribution in Galactic coordinates of all pulsars detected in the PMPS to date.

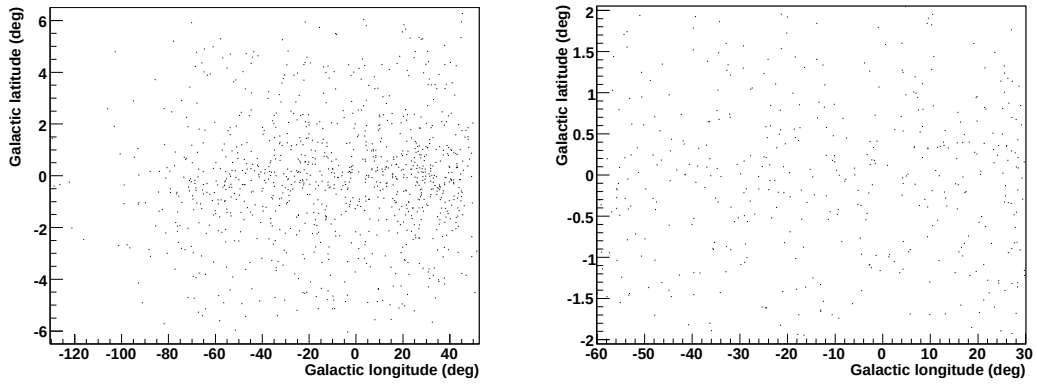

FIGURE 4.5: *Left:* Distribution of all pulsars detected in the PMPS to date. *Right:* Distribution of the PMPS search sample.

Of these pulsars, a total of 435 pulsar locations are tested within the search region of Galactic longitudes from -60 deg to 30 deg and Galactic latitudes of ± 2 deg, shown in the right panel of Figure 4.5. Pulsars without measured period derivatives are ignored. Over the range of the H.E.S.S. survey, the PMPS provides reasonably uniform sensitivity (Manchester et al., 2001), enabling a reliable estimate of the frequency of chance coincidences between a VHE γ-ray source and a pulsar. The pulsars in this sample have spin-down luminosities $\dot{E}$ of $(4.3 \times 10^{29} - 1.8 \times 10^{37})$ erg/s, and spin-down energy fluxes $\dot{E}/(4\pi d^2)$[3] of $(3.1 \times 10^{27} - 9.2 \times 10^{35})$ erg/s/kpc^2, the distribution of the latter is shown in the left panel of Figure 4.6. In the right panel, the spin-down energy fluxes $\dot{E}/d^2$ of the pulsars are plotted against their Galactic latitudes. An indication that pulsars with higher $\dot{E}/d^2$ are found closer to the Galactic plane can be seen. This seems reasonable, as pulsars are expected to be born with a kick velocity, which will often move them away from their birth place in the Galactic plane while they are getting older and thus losing some of their spin-down energy flux.

The pulsars have characteristic ages between 1550 years and 6×10^8 years.

[3]For simplicity, from now on $\dot{E}/(4\pi d^2)$ is denoted as $\dot{E}/d^2$.

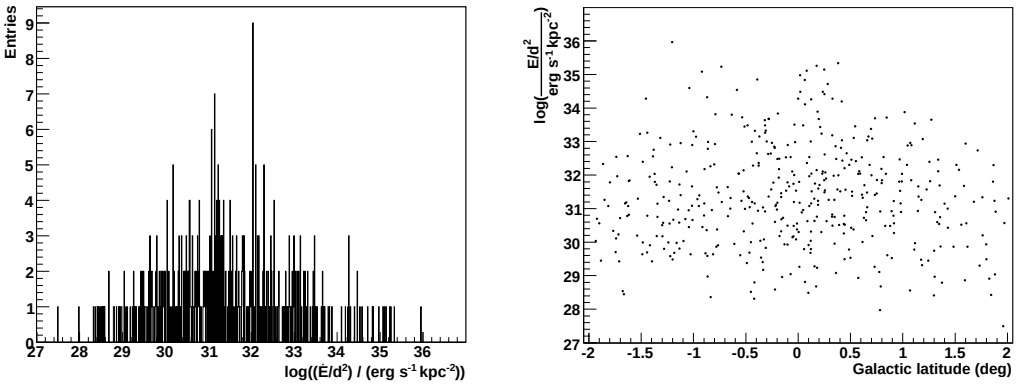

FIGURE 4.6: *Left:* Distribution of the spin-down energy fluxes $\dot{E}/d^2$ of the search pulsar sample. *Right:* $\dot{E}/d^2$ versus Galactic latitude.

Figure 4.7 displays the distribution of spin-down energy fluxes $\dot{E}/d^2$ versus characteristic ages of the pulsars; as expected, older pulsars have in general lower spin-down energy fluxes.

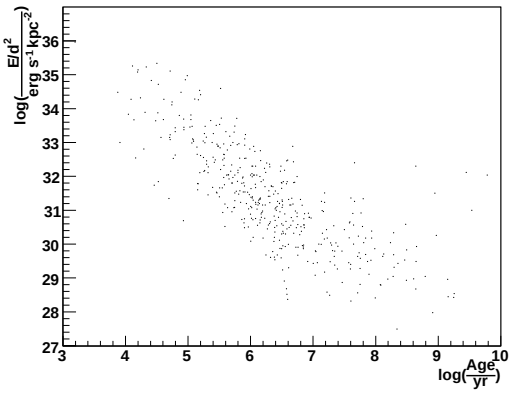

FIGURE 4.7: Distribution of the spin-down energy fluxes $\dot{E}/d^2$ versus the characteristic ages of the search pulsar sample.

The distances of the pulsars range between (1 – 30) kpc. The distances used in this work, in the following denoted as D_{1993}, result from Taylor and Cordes (1993). To check if a more recent estimate for the distances of the pulsars from Cordes and Lazio (2002), in the following denoted as D_{2002}, would have a significant influence on the results of the search, Figure 4.8 compares the two distance estimates and the respective values derived for the spin-down energy fluxes $\dot{E}/d^2$ of the 435 pulsars in the PMPS search sample. In the left panel, the D_{2002} dis-

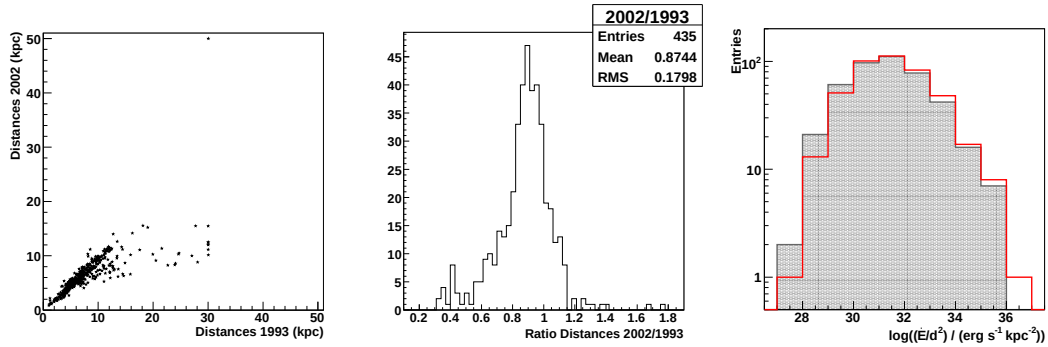

FIGURE 4.8: Comparison of two distance estimates, D_{1993} from Taylor and Cordes (1993) and D_{2002} from Cordes and Lazio (2002), and the respective values derived for the spin-down energy fluxes $\dot{E}/d^2$ of the 435 pulsars in the PMPS search sample. *Left:* D_{2002} distances versus D_{1993} distances. Most of the values are in good agreement, however, for D_{1993} distances above 15 kpc, the D_{2002} estimates give shorter distances. *Middle:* Ratio of the two estimates. The distribution has a mean of 0.87 and an RMS of 0.18, indicating a general trend to lower estimates for the distances. *Right:* Distribution of the resulting $\dot{E}/d^2$ for D_{1993} (grey filled histogram) and D_{2002} (red line).

tances are plotted against the D_{1993} distances. Most of the values are in good agreement, however, for D_{1993} distances above 15 kpc, the D_{2002} estimates give shorter distances. To quantify this, the ratio of the two estimates is given in the middle panel. The distribution has a mean of 0.87 and an RMS of 0.18, indicating a general trend to lower estimates for the distances. To demonstrate what influence the more recent distance estimates would have on the distribution of the spin-down energy fluxes $\dot{E}/d^2$, in the right panel the two respective $\dot{E}/d^2$ distributions are shown, grouped into 10 bands of $\log(\dot{E}/d^2)$ from $\log(\dot{E}/d^2) = 27$ to $\log(\dot{E}/d^2) = 37$. The $\dot{E}/d^2$ distribution for D_{1993} distances is shown as a grey filled histogram, while the $\dot{E}/d^2$ distribution for D_{2002} distances is shown as a red line. As expected from the ratio distribution, for the more recent distance estimates a slight shift in the $\dot{E}/d^2$ distribution to higher values of $\dot{E}/d^2$ can be seen. This would in principle lead to slightly lower statistical significances for the detection of emission from high-power pulsars, however, performing a cross-check by repeating the analysis described in Chapter 7 by using the distance estimates from Cordes and Lazio (2002), it was found that the different distance estimates do not significantly change the results of the search.

The knowledge of the transverse velocity of pulsars coinciding with VHE γ-ray emission would be of great interest, as for pulsars that are offset from the centre of the VHE γ-ray emission, a matching transverse velocity would strengthen the association of the pulsar, respectively its nebula, with the VHE γ-ray emission. However, only for three pulsars out of the 435 pulsars in the PMPS search sample

an estimate of the transverse velocity (and proper motion) is given in the ATNF catalogue, and at none of their positions significant VHE γ-ray emission is found. Currently, an estimate of the transverse velocity exists only for 212 of the pulsars listed in the ATNF catalogue.
The sketch in Figure 4.9 shows the search pulsar sample drawn on top of the H.E.S.S. significance and exposure map.

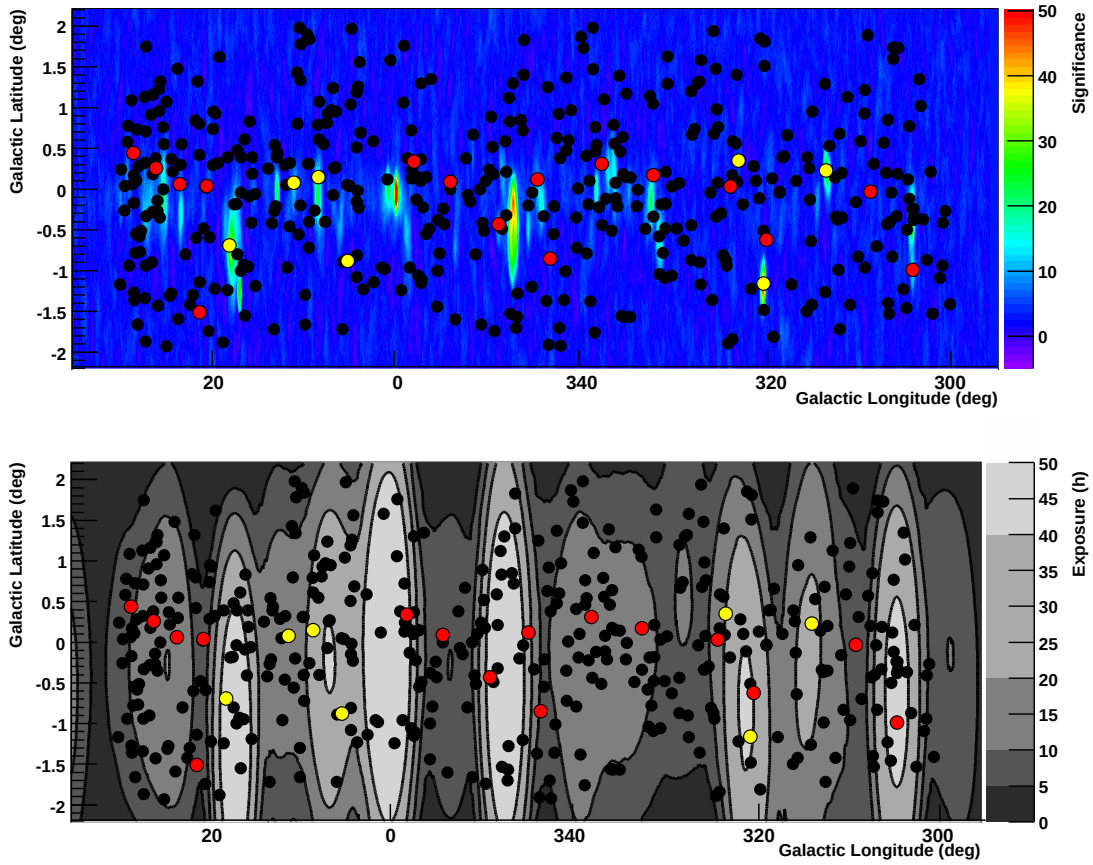

FIGURE 4.9: The selected sample of PMPS pulsars in the search region, drawn on top of the H.E.S.S. significance map (*top*) and the H.E.S.S. exposure map (*bottom*). Pulsars with an $\dot{E}/d^2 > 10^{35}$ erg s^{-1}kpc^{-2} are marked as yellow filled circles, pulsars with an $\dot{E}/d^2$ between $(10^{34} - 10^{35})$ erg s^{-1}kpc^{-2} as red filled circles and pulsars with an $\dot{E}/d^2 < 10^{34}$ erg s^{-1}kpc^{-2} as black filled circles. Note that the circles are of arbitrary size and do not represent the integration region around each pulsar.

4.3 First Results

Of the 435 pulsars, 30 are found with significant γ-ray emission at the pulsar location; the list of the detection significances can be found in Section 7.1. Not all of these associations are necessarily genuine and for plausible values of the ratio between the γ-ray luminosity and the pulsar spin-down luminosity, $L_\gamma/\dot{E}$, no detectable emission would be expected from pulsars with $\dot{E}/d^2 < 10^{33}$ erg s^{-1}kpc^{-2}. To evaluate the significance of the detection of VHE γ-ray emission from pulsars with high $\dot{E}/d^2$, an estimate of the chance coincidences between VHE γ-ray sources and pulsars is essential (see Chapter 7).

Table 4.3 lists for the most powerful PMPS pulsars, above $\dot{E}/d^2 > 3 \times 10^{34}$ erg s^{-1}kpc^{-2}, the pulsar properties relevant for this study along with the VHE γ-ray flux between (1 – 10) TeV (or the upper limit on the energy flux between (1 –10) TeV in case of a non-detection), the ratio of the γ-ray luminosity to the spin-down luminosity, $L_\gamma/\dot{E}$, the size of the γ-ray source and its displacement from the pulsar position.

Most of the listed γ-ray sources are already known (Aharonian et al., 2006e). However, at the position of two energetic pulsars, two sources – HESS J1718−385, associated with PSR J1718−3825, and HESS J1809−193, associated with PSR J1809−1917 – were discovered as a result of this search. Details about these sources will be presented in the next two chapters, followed by the description of the systematic study of a connection between pulsars and VHE γ-ray sources.

PSR	l	b	$\dot{E}$	d	$\dot{E}/d^2$	Age	VHE flux 1 – 10 TeV	$L_\gamma/\dot{E}$	Size	Offset
	(°)	(°)	(erg s^{-1})	(kpc)	(erg s^{-1}kpc^{-2})	(kyr)	(erg s^{-1}cm^{-2})	(%)	(arcmin)	(arcmin)
B1259−63	304.18	−0.99	8.2×10^{35}	4.6	3.9×10^{34}	332.0	1.1×10^{-12}	0.3	0.6	0.0
J1420−6048	313.54	0.23	1.0×10^{37}	7.7	1.8×10^{35}	13.0	4.2×10^{-11}	3.0	4.2	2.4
J1509−5850	319.97	−0.62	5.1×10^{35}	3.8	3.5×10^{34}	154.0	$< 3.0 \times 10^{-12}$	< 1.0	-	-
B1509−58	320.32	−1.16	1.8×10^{37}	4.4	9.2×10^{35}	1.6	2.0×10^{-11}	0.3	7.8×4.8	1.8
J1524−5625	323.00	0.35	3.2×10^{36}	3.8	2.2×10^{35}	31.8	$< 1.8 \times 10^{-12}$	< 0.1	-	-
J1531−5610	323.90	0.03	9.1×10^{35}	3.1	9.5×10^{34}	97.1	$< 1.7 \times 10^{-12}$	< 0.2	-	-
B1610−50	332.21	0.17	1.6×10^{36}	7.2	3.0×10^{34}	7.4	2.1×10^{-11}	8.4	11.4	22.8
J1718−3825*	348.95	−0.43	1.3×10^{36}	4.2	7.0×10^{34}	89.5	2.9×10^{-12}	0.5	9.0×4.2	8.4
B1727−33	354.13	0.09	1.2×10^{36}	4.2	6.8×10^{34}	26.0	$< 4.7 \times 10^{-12}$	< 0.8	-	-
B1757−24	5.25	−0.88	2.6×10^{36}	4.6	1.2×10^{35}	15.5	$< 9.3 \times 10^{-13}$	< 0.1	-	-
B1800−21	8.40	0.15	2.2×10^{36}	3.9	1.4×10^{35}	15.8	9.2×10^{-12}	0.8	13.8	12.5
J1809−1917*	11.09	0.08	1.8×10^{36}	3.7	1.3×10^{35}	51.3	1.3×10^{-11}	1.2	32.4×15.0	12.0
B1823−13	18.00	−0.69	2.8×10^{36}	4.1	1.7×10^{35}	21.4	4.4×10^{-11}	3.3	18.0	19.8
J1828−1101	20.49	0.04	1.6×10^{36}	7.3	3.0×10^{34}	77.1	$< 3.3 \times 10^{-12}$	< 1.3	-	-
J1837−0604	25.96	0.26	2.0×10^{36}	6.2	5.2×10^{34}	33.8	$< 4.8 \times 10^{-12}$	< 1.1	-	-

TABLE 4.1: PMPS pulsars with an $\dot{E}/d^2 > 3 \times 10^{34}$ erg s^{-1}kpc^{-2} in the search region, taken from Manchester et al. (2005). Name, Galactic coordinates (l, b), spin-down power $\dot{E}$, distance d (resulting from Taylor and Cordes (1993)), spin-down energy flux $\dot{E}/d^2$, age, VHE γ-ray flux between (1 – 10) TeV (for non-detections the energy flux limit between (1 – 10) TeV, at 99% confidence level), the ratio between the (1 – 10) TeV γ-ray luminosity and the pulsar spin-down luminosity $L_\gamma/\dot{E}$, the size of the VHE emission region (i.e. the fitted widths of a two-dimensional Gaussian after unfolding the H.E.S.S. point-spread function) and the offset of the center of the VHE emission region from the pulsar position are listed. The observed $L_\gamma/\dot{E}$ implies a much larger conversion efficiency to leptons in the PWN, given the competition from synchrotron radiation, the relative amount of energy lost to IC radiation and the fact that only a small part of the total energy in electrons resides in the multi-TeV electrons responsible for the production of VHE γ-rays. The exact modelling thereof is beyond the scope of this work. The two new sources discovered in this search are marked by a star.

Chapter 5

HESS J1718 − 385

In the systematic study of a connection between pulsars and VHE γ-ray sources, significant VHE γ-ray emission was detected at the location of the energetic pulsar PSR J1718−3825. In this chapter the analysis of the new VHE γ-ray source HESS J1718−385 is presented and its possible association to PSR J1718−3825 is discussed.

5.1 Observations and Analysis

The data on HESS J1718−385 are composed primarily from dedicated observations of the SNR RX J1713.7−3946 (G347.3−0.5), which is located at about 1.6 degrees South-West of HESS J1718−385 (Koyama et al., 1997; Muraishi et al., 2000; Aharonian et al., 2006b). In Figure 5.1 an image of the VHE γ-ray excess counts of the field of view around HESS J1718−385 is displayed.

After applying the H.E.S.S. standard data-quality criteria based on hardware and weather conditions, the data set for HESS J1718−385 has a total live time of ∼82 hours (see Table 5.1 for observation and analysis properties). These data come from H.E.S.S. observations whose centre positions are less than 3 degrees offset from the respective best-fit source position. Since most of the observations were not specifically targeted at HESS J1718−385, the mean offset from the pointing position is larger than for dedicated observations (which are typically offset by ≤ 1.0 degrees).

The standard H.E.S.S. analysis scheme (see Section 3.4 and Aharonian et al. (2006c)) is applied to the data, including optical efficiency corrections. To produce a sky map, *hard cuts* are applied, which include a rather tight cut on the shower image brightness of ≥200 photo-electrons and are suitable for extended, hard-spectrum sources such as PWN. The background at each test position in the sky is derived from a ring surrounding this position with a mean radius of 1 degree and a width scaled to provide a background area that is about 7 times larger than the area of the on-source region.

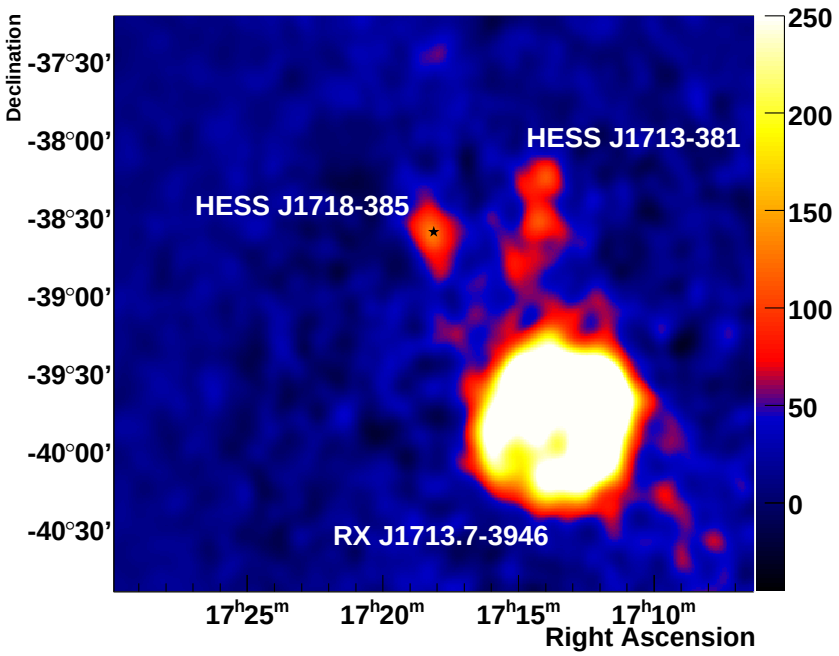

FIGURE 5.1: An image of the VHE γ-ray excess counts of the field of view around HESS J1718−385, smoothed with a Gaussian of width 0.06 deg. The strong source RX J1713.7−3946 can be seen to the South-West of HESS J1718−385, and another extended HESS source, HESS J1713−381, can be seen to the West.

HESS J1718−385											
Sky Map						Spectrum					
θ_M (deg)	Cuts	t_{live} (hrs)	$\langle ZA \rangle$ (deg)	ϕ (deg)	E_{thr} (GeV)	θ_S (deg)	Cuts	t_{live} (hrs)	$\langle ZA \rangle$ (deg)	ϕ (deg)	E_{thr} (GeV)
0.11	hard	82	33.9	1.6	450	0.2	hard	73	32.5	1.1	450

TABLE 5.1: Data properties and analysis parameters for HESS J1718−385: here, θ_M and θ_S is the on-source integration radius for the sky map and the spectral analysis, respectively, t_{live} is the live time, $\langle ZA \rangle$ is the mean zenith angle, ϕ is the mean offset of the observation position from the target position, and E_{thr} is the analysis threshold energy.

The detection significance from the search for VHE γ-ray emission within 0.22 degrees of the location of PSR J1718−3825 is 7.9σ. A very conservative estimate of the number of trials involved (similar to Aharonian et al., 2006e) leads to a corrected significance of 6.2σ.

Figure 5.2 shows the excess count map of the 1 deg × 1 deg region around

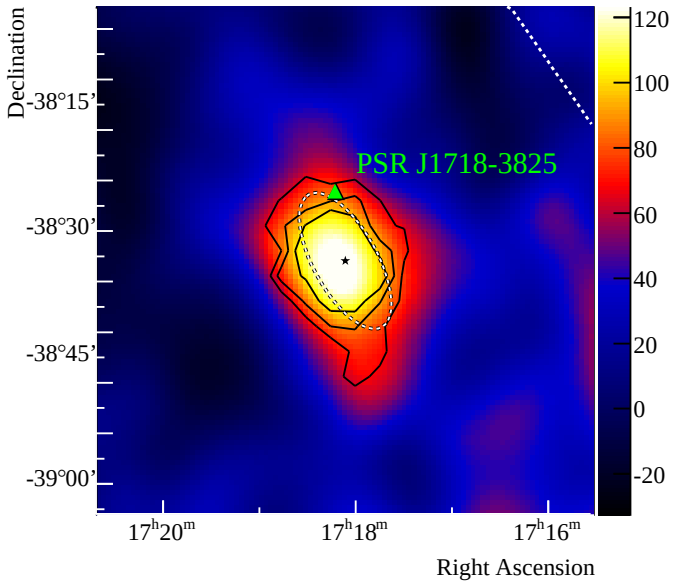

FIGURE 5.2: An image of the VHE γ-ray excess counts of HESS J1718−385, smoothed with a Gaussian of width 0.06 deg. The colour scale is set such that the blue/red transition occurs at approximately the 3σ significance level. The black contours are the 4, 5 and 6σ significance contours. For this significance calculation, events were correlated with a top hat function with an RMS chosen to match that of the Gaussian smoothing (and thus an integration radius $\theta_{\mathrm{M}} = 0.11$ deg). The position of the pulsar PSR J1718−3825 is marked with a green triangle and the Galactic plane is shown as a white dotted line. The best-fit position for the γ-ray source is marked with a black star and the fit ellipse with a dashed line.

HESS J1718−385, smoothed with a Gaussian of width 0.06 degrees chosen to reduce statistical fluctuations while retaining source features. A two-dimensional Gaussian brightness profile, folded with the H.E.S.S. point-spread function, is fit to the distribution before smoothing. Its parameters are the width in two dimensions and the orientation angle, defined counter-clockwise from North. The intrinsic widths (with the effect of the point-spread function removed) for the fit are $9' \pm 2'$ and $4' \pm 1'$ and the orientation angle is $\sim 33°$. The best-fit position for the centre of the excess is RA $= 17^{\mathrm{h}}18^{\mathrm{m}}7^{\mathrm{s}} \pm 5^{s}$, Dec $= -38°33' \pm 2'$ (epoch J2000). H.E.S.S. has a systematic pointing error of $\sim 20''$.

For spectral studies, only observations in which the camera centre is offset by less than 2 degrees from the best-fit source position were used to reduce systematic effects due to reconstructed γ-ray directions falling close to edge of the field of view. The remaining live time of the data sample is $\sim$73 hours. The spectral significance is calculated by counting events within a circle of radius

$\theta_S = 0.2$ deg from the best-fit position. The integration radius was chosen to enclose the whole emission region while reducing systematic effects arising from morphology assumptions. For deriving the energy spectrum, *hard cuts* are retained as these cuts also improve the angular resolution and therefore suppress contamination from the nearby SNR RX J1713.7−3946. It is vital to exclude this source generously, as it shows emission out to one degree of its centre (see Berge (2006) for a detailed study). In Figure 5.3, a slice through HESS J1718−385 and RX J1713.7−3946 is shown, indicated as the box in the upper panel. In the lower panel, excess counts over the length of the box are displayed. An indication for some excess - besides the small peak for HESS J1718−385 (around −1) and the large peak for RX J1713.7−3946 (around +0.5) - can be seen between the sources and to the South-West of RX J1713.7−3946. To the North-East of HESS J1718−385 there is no indication for an excess.

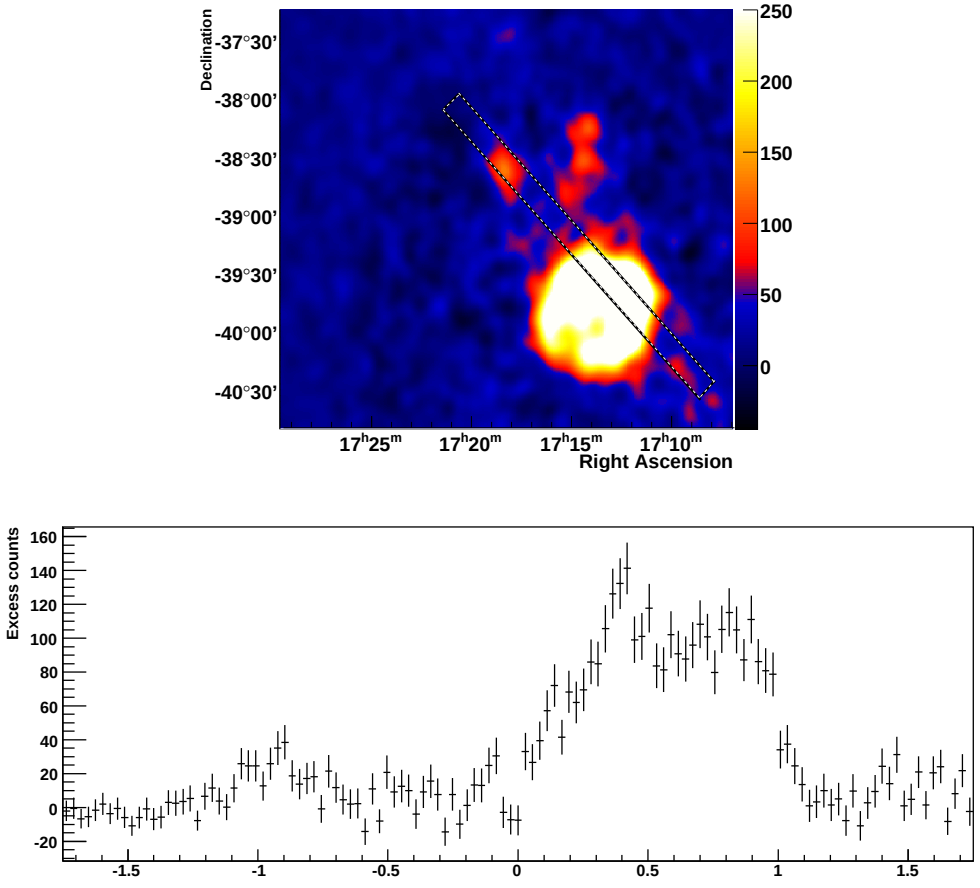

FIGURE 5.3: Slice through HESS J1718−385and RX J1713.7−3946. *Upper panel:* The slice is indicated as the box on top of the map from Figure 5.1. *Lower panel:* Excess counts over the range of the box.

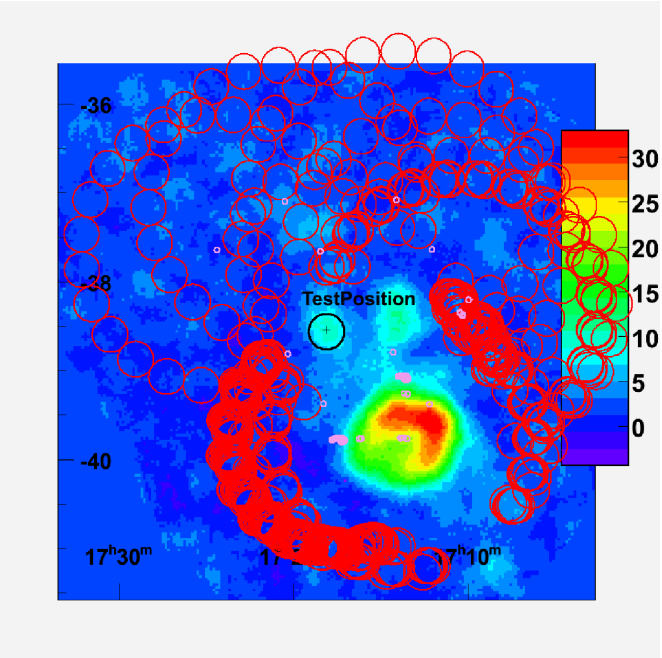

FIGURE 5.4: Background regions from the *reflected background* method. The *on* region is marked with a black circle, observation positions with pink circles and background regions with red circles. A clustering of background regions to the South-East and West of the *on* region can be seen.

The proximity of this strong source and other sources in the field of view makes it advisable to choose the background data from off-source observations (matched to the zenith angle and offset distribution of the on-source data) instead of from areas in the same field of view. As can be seen in Figure 5.4, using the *reflected background* method in this field of view leads to a clustering of background regions to the South and West of the *on* region. The reason for this is that most of the observations were taken specifically for RX J1713.7−3946, the strong extended source seen South-West to the *on* region. Figure 5.3 indicates that in regions close to RX J1713.7−3946, the background might be contaminated by some signal, giving the main reason for taking background data from off-source observations. Further influence on the energy spectrum could have a systematically different zenith angle distribution for the background in comparison to the zenith angle distribution for the *on* region, caused by the clustering of the background regions. However, comparing the zenith angle distributions for the *on/off background* method and the *reflected background* method in Figure 5.5, no crucial difference can be seen. As can be seen in Figure 5.6, the offset distributions for both methods (comparing *on* and background regions) agree reasonably well. Note that in all cases the *on* distributions between the two methods differ, as for

some runs in the *reflected background* method no matching background regions could be found.

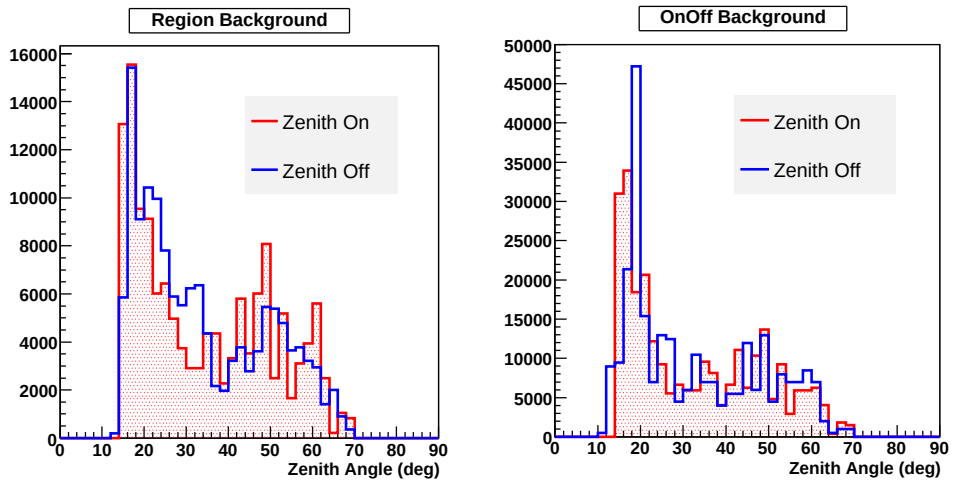

FIGURE 5.5: Zenith distributions for *reflected background* (*left*) and *on/off background* (*right*) method. For both methods the *on* and background (*off*) distributions match reasonably well. The distributions are filled for each event.

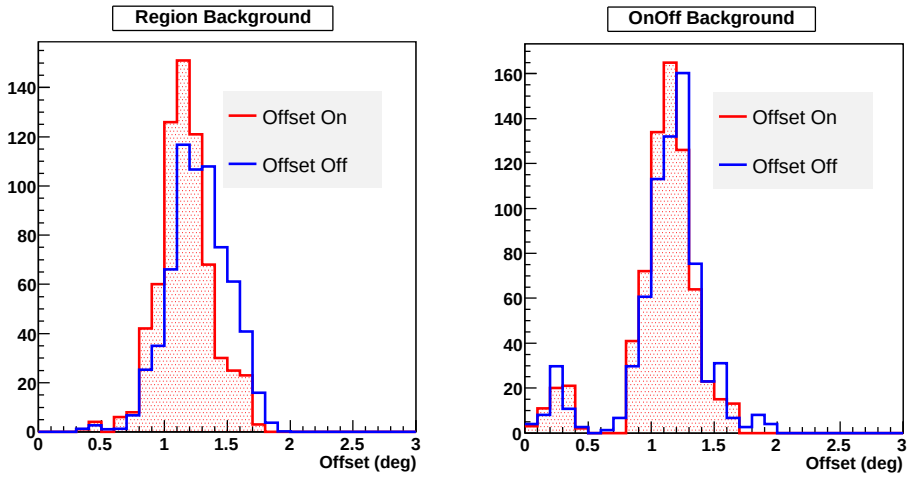

FIGURE 5.6: Offset distributions for *reflected background* (*left*) and *on/off background* (*right*) method. For both methods the distribution match reasonably well. The distributions are filled for each event with the offset of the event's reconstructed sky position from the best-fit source position.

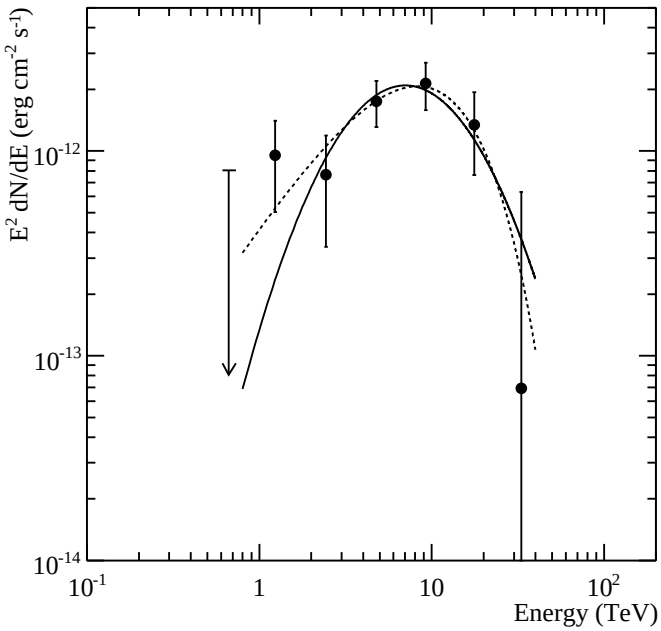

FIGURE 5.7: The energy spectrum of HESS J1718−385, which is fit by a curved profile (solid line). Alternatively, the fit of an exponentially cut-off power law is shown (dashed line, refer to the text for details on both fits). The first point in the spectrum lacks statistics due to lower exposure at small zenith angles and is plotted as 95% c.l. upper limit

For the spectral analysis, a statistical significance of 6.8σ (with 343 excess counts) is derived. Figure 5.7 shows the measured spectral energy distribution for HESS J1718−385 (in $E^2\,dN/dE$ representation). The fit of a pure power law ($dN/dE = N_0(E/E_0)^{-\Gamma}$) to the spectrum gives a $\chi^2/d.o.f.$ of 11.1/4 and a spectral index of $\Gamma = 2.1 \pm 0.1_{\rm stat} \pm 0.2_{\rm sys}$.

The spectrum is fit by a curved profile (shown as the solid line):

$$\frac{dN}{dE} = N_0 \left(\frac{E_{\rm peak}}{1\,{\rm TeV}}\right)^{-2.0} \left(\frac{E}{E_{\rm peak}}\right)^{(\beta \cdot \ln E/E_{\rm peak})-2.0} \tag{5.1}$$

The peak energy $E_{\rm peak}$ is $(7 \pm 1_{\rm stat} \pm 1_{\rm sys})$ TeV, the differential flux normalisation $N_0 = (1.3 \pm 0.3_{\rm stat} \pm 0.5_{\rm sys}) \times 10^{-12}\,{\rm TeV}^{-1}\,{\rm cm}^{-2}\,{\rm s}^{-1}$ and $\beta = -0.7 \pm 0.3_{\rm stat} \pm 0.4_{\rm sys}$. This fit has a $\chi^2/d.o.f.$ of 3.2/3. The integral flux between $1 - 10$ TeV is about 2 % of the flux of the Crab nebula in the same energy range (Aharonian et al., 2006c). This spectral fit is used to derive the energy flux used in Table 5.2.

Alternatively, fitting the spectrum by an exponentially cut-off power law

$$\frac{dN}{dE} = N_0 \left(\frac{E}{1\,\mathrm{TeV}} \right)^{-\Gamma} e^{-(E/E_{\mathrm{cut}})} \tag{5.2}$$

gives $N_0 = (3.0 \pm 1.9_{\mathrm{stat}} \pm 0.9_{\mathrm{sys}}) \times 10^{-13}\,\mathrm{TeV}^{-1}\,\mathrm{cm}^{-2}\,\mathrm{s}^{-1}$, photon index $\Gamma = 0.7 \pm 0.6_{\mathrm{stat}} \pm 0.2_{\mathrm{sys}}$ and a cut-off in the spectrum at an energy of $E_{\mathrm{cut}} = (6 \pm 3_{\mathrm{stat}} \pm 1_{\mathrm{sys}})\,\mathrm{TeV}$. This fit, which is shown as a dashed line in Figure 5.7, has a $\chi^2/d.o.f.$ of 1.6/3. The integral flux between $1 - 10$ TeV is about 2 % of the flux of the Crab nebula in the same energy range (Aharonian et al., 2006c).

It should be noted that the systematic errors, especially on the flux normalisation, are larger than normally quoted in H.E.S.S. publications, as an independent cross-check performed with an independent calibration and analysis chain did not agree as well as usual.

Both the curved and exponentially cut-off power law profiles fit the data well; the former has the advantage of showing explicitely the peak energy of the spectrum, which has to date only been resolved in one other VHE γ-ray source, Vela X (Aharonian et al., 2006f).

5.2 Possible Associations

PSR J1718−3825 appears to be a Vela-like pulsar, as it is of comparable age and has a similar spin period, 75 ms. Compared with the general sample used in the systematic search, the associated VHE γ-ray emission seems to fit into the emerging picture of γ-ray PWNe, as implied by sources like Vela X, HESS J1825-137 and the two PWN candidates in the Kookaburra complex. The offset of the VHE γ-ray emission from the pulsar position is not atypical compared with other probable PWNe associations. Such offset PWNe can be explained by either the proper motion of the pulsar, or by interaction with non-uniform regions in the interstellar medium (Blondin et al., 2001).

The γ-ray source HESS J1718−385 is located ∼0.14 degrees south of the pulsar PSR J1718−3825 (shown as a green triangle in Figure 5.2 and as a red triangle in Figure 5.8). With a distance of ∼4 kpc and a spin-down flux $\dot{E}/d^2$ on the order of $10^{35}\,\mathrm{erg\,kpc^{-2}\,s^{-1}}$, the pulsar is energetic enough to power HESS J1718−385, with an implied efficiency of conversion into (1 – 10) TeV γ-rays of $\epsilon_\gamma \equiv L_\gamma/\dot{E} = 0.5\,\%$ (see Table 5.2).

As can be seen in Figure 5.8, no obvious X-ray counterpart is visible for HESS J1718−385. There is diffuse extended radio emission, which is partially coincident with the VHE γ-ray emission. However, this emission seems to be correlated with thermal dust emission visible in the IRAS Sky Survey Atlas (Neugebauer et al., 1984), suggesting that the radio emission is thermal and is thus not likely associated with a possible PWN. The brightest part of this diffuse feature is catalogued as PMN J1717−3846 (Wright et al., 1994). From the point

PSR J1718−3825 – HESS J1718−385						
Spin-down luminosity (erg s^{-1})	Spin-down age (kyr)	Distance (kpc)	1−10 TeV Flux (erg $cm^{-2}s^{-1}$)	Size (pc)	Offset (pc)	$L_\gamma/\dot{E}$ ((1−10) TeV)
1.3×10^{36}	90	4.2 (3.6)	2.9×10^{-12}	11	10	0.5 %

TABLE 5.2: HESS J1718−385 as a PWN and some properties of the possibly associated pulsar PSR J1718−3825, taken from Manchester et al. (2005). The spin-down age, defined as $P/2\dot{P}$ (where P is the period of the pulsar), provides an age estimate for a pulsar if the birth period of the pulsar was short in comparison to the current period and assuming a braking index $n = 3$ (Kramer et al., 2003). The pulsar distances result from Taylor and Cordes (1993); a more recent estimate for the distances of the pulsars from Cordes and Lazio (2002) (given in parentheses) does not significantly change the estimates for size, offset and efficiency. The size refers to the larger intrinsic width from the respective fits, and the offset refers to the distance of the pulsar from the best-fit position of the VHE γ-ray emission region. $L_\gamma/\dot{E}$ is the ratio of the γ-ray luminosity of the VHE γ-ray source to the spin-down power of the pulsar.

of view of positional coincidence, energetics, and lack of other counterparts, the association of HESS J1718−385 with PSR J1718−3825 seems likely. To confirm this, additional evidence from spectral and morphological studies in VHE γ-rays and from data at other wavelengths is needed.

PSR J1718−3825 has so far no associated PWN detected in radio to X-ray wavelengths. Since the VHE γ-ray emission is assumed to come from IC scattering of high-energy electrons off the cosmic microwave background radiation, the VHE γ-ray spectrum predicts the electron spectrum and one would expect to see X-ray synchrotron emission from this object. Under the assumption of a magnetic field in the range of a few μG, the expected peak synchrotron flux is $\sim 10^{-12}(B/5\mu\mathrm{G})^2\,\mathrm{erg\,cm^{-2}\,s^{-1}}$. It should be possible for instruments such as XMM-Newton to reveal an X-ray counterpart. However, with the cut-off seen at $\sim 10\,\mathrm{TeV}$ in VHE γ-rays, the X-ray flux may peak below the XMM-Newton range.

HESS J1718−385 may well represent the first VHE γ-ray PWN found in a systematic search for pulsar associations, despite the present lack of a PWN detection in other wavebands. The remarkable similarity between HESS J1718−385 and other known VHE γ-ray PWNe, together with the lack of other probable counterparts, gives additional confidence. The detection of an X-ray PWN would provide confirmation.

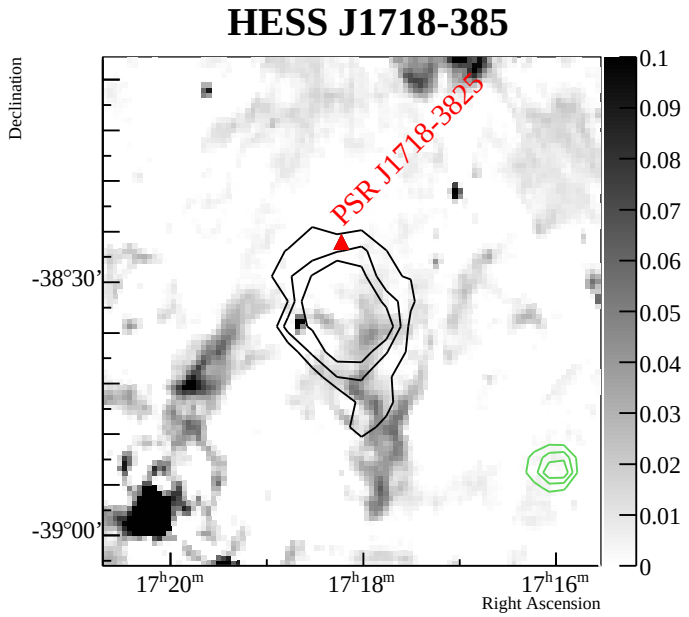

FIGURE 5.8: Radio image from the Molonglo Galactic Plane Survey at 843 MHz (Green et al., 1999) (in Jy/beam). The H.E.S.S. significance contours are overlaid in black and the pulsar position is marked with a red triangle. Adaptively smoothed ROSAT hard-band X-ray contours are shown in green (Voges et al., 2001).

Chapter 6

HESS J1809 – 193

The second detection of significant VHE γ-ray emission in the systematic study of a connection between pulsars and VHE γ-ray sources was made at the location of the energetic pulsar PSR J1809−1917. The analysis of the new VHE γ-ray source HESS J1809−193 is presented in this chapter, alongside with its possible associations with PSR J1809−1917 and other objects seen in radio and X-ray wavelengths.

6.1 Observations and Analysis

The first H.E.S.S. observations of the region around HESS J1809−193 were taken as part of the systematic survey of the inner Galaxy from May to June 2004 (Aharonian et al., 2005b, 2006e). As there was a marginally significant VHE γ-ray signal, re-observations of HESS J1809−193 were taken in 2004 and 2005. After passing the H.E.S.S. standard data-quality criteria (Aharonian et al., 2006c) based on hardware and weather conditions, the data set for HESS J1809−193 has a total live time of ∼25 hours (see Table 6.1 for observation and analysis properties). Like for HESS J1718−385, the data come from observations whose centre positions are less than 3 degrees offset from the respective best-fit source position. Again, most of the observations were not specifically targeted at this source, leading to larger offsets from the pointing positions than for dedicated observations.

The standard H.E.S.S. analysis scheme (see Section 3.4 and Aharonian et al. (2006c)) is applied to the data, including optical efficiency corrections. To produce sky maps, the same procedure as for HESS J1718−385 is applied, using *hard cuts* and a ring with a mean radius of 1 degree to derive the background.

The detection significance from the search for VHE γ-ray emission within 0.22 deg of the location of PSR J1718−3825 is 6.8σ (4.7σ post trials). Figure 6.1 displays the uncorrelated excess count map of the 1.5 deg × 1.5 deg region around HESS J1809−193, smoothed with a Gaussian of width 0.11 deg, again chosen to

HESS J1809−193											
Sky Map						Spectrum					
θ_M (°)	Cuts	t_{live} (hrs)	$\langle ZA \rangle$ (°)	ϕ (°)	E_{thresh} (GeV)	θ_S (°)	Cuts	t_{live} (hrs)	$\langle ZA \rangle$ (°)	ϕ (°)	E_{thresh} (GeV)
0.19	hard	25	20.4	1.7	350	0.5	standard	9	26.5	1.0	250

TABLE 6.1: Data properties and analysis parameters for HESS J1809−193: θ_M and θ_S is the on-source integration radius for the sky map and the spectral analysis, respectively, t_{live} is the live time, $\langle ZA \rangle$ is the mean zenith angle, ϕ is the mean offset of the observation position from the target position, and E_{thresh} is the analysis threshold energy.

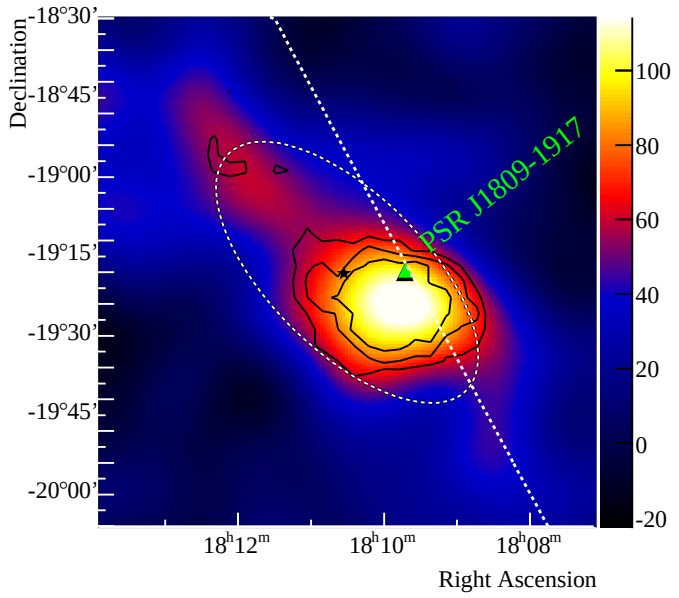

FIGURE 6.1: An image of the VHE γ-ray excess counts of HESS J1809−193, smoothed with a Gaussian of width 0.11 deg. See caption of Figure 5.2 for details on the colour scale and the (black) significance contours (here correlated with an integration radius $\theta_M = 0.19$ deg). PSR J1809−1917 is marked with a green triangle, the Galactic plane is shown as a white dotted line. The best fit position for the γ-ray source is marked with a black star and the fit ellipse with a dashed line.

reduce statistical fluctuations while retaining source features. Assuming a two-dimensional Gaussian brightness profile folded with the H.E.S.S. point-spread function for this clearly extended source, the intrinsic widths of the fit ellipse are $32' \pm 4'$ and $15' \pm 2'$, and the orientation angle is $\sim 50°$. The best fit position for the centre of the excess is RA $= 18^h10^m31^s \pm 12^s$, Dec $= -19°18' \pm 2'$ (epoch

J2000).

In Figure 6.2, a slice through HESS J1809−193 is shown, indicated as the box in the upper panel. In the lower panel, excess counts over the length of the box are displayed. From this plot it cannot be decided whether the single peaks that seem to show up could belong to (unresolved) single sources.

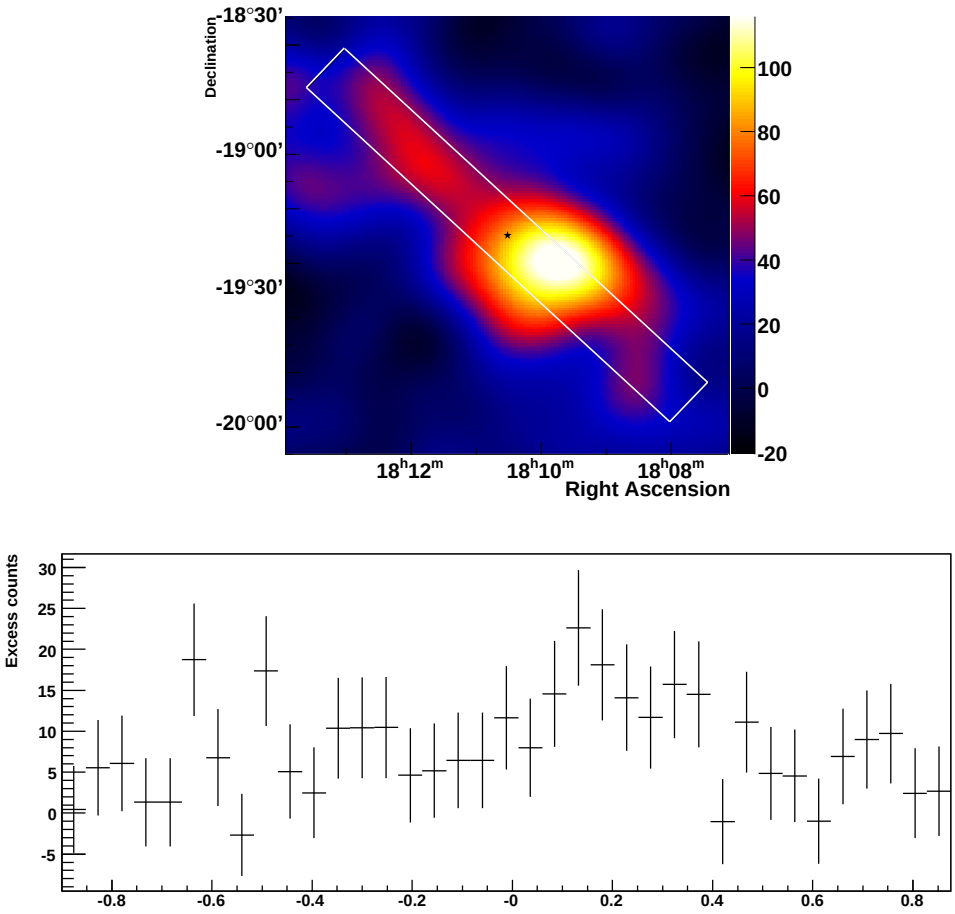

FIGURE 6.2: Slice through HESS J1809−193. *Upper panel:* The slice is indicated as the box on top of the map from Figure 6.1. *Lower panel:* Excess counts over the range of the box.

For spectral studies, also only observations in which the camera centre is offset by less than 2 degrees from the best-fit source position are used. The remaining live time of the data sample is ∼9 hours. The spectral significance is calculated by counting events within a circle of radius $\theta_S = 0.5$ deg from the best fit position. The integration radius was again chosen to enclose essentially the whole emission region for HESS J1809−193. Contrary to HESS J1718−385, for the spectral analysis of HESS J1809−193 *standard cuts* on the image parameters are applied,

loosening the minimum image brightness to 80 photo-electrons to extend the energy spectrum down to ∼250 GeV (at the expense of a reduced signal-to-noise ratio). The background is estimated from regions with equal offset from the centre of the field of view to minimise spectral systematic uncertainties.

For the spectral analysis, a statistical significance of 7.6σ (with 875 excess counts) is derived. Figure 6.3 shows the measured spectral energy distribution for HESS J1809−193 (in $E^2\,dN/dE$ representation). The spectrum is well fit by a power law ($dN/dE = N_0(E/E_0)^{-\Gamma}$) with photon index $\Gamma = 2.2 \pm 0.1_{\rm stat} \pm 0.2_{\rm sys}$ and differential flux normalisation at 1 TeV $N_0 = (4.6 \pm 0.6_{\rm stat} \pm 0.9_{\rm sys}) \times 10^{-12}\,{\rm TeV}^{-1}\,{\rm cm}^{-2}\,{\rm s}^{-1}$ and gives a $\chi^2/d.o.f. = 6.9/5$. Its integral flux between $(1 - 10)$ TeV is about 14 % of the flux of the Crab nebula in the same energy range.

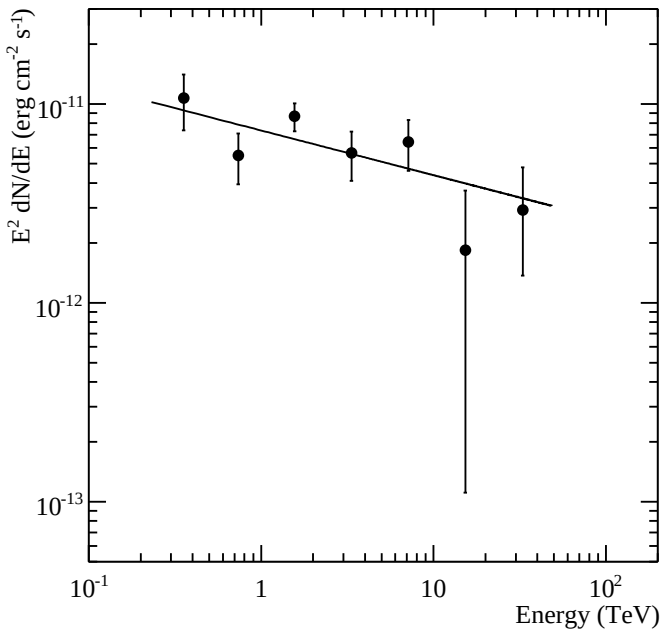

FIGURE 6.3: The energy spectrum of HESS J1809−193, which is fit by a power law with slope $\Gamma = 2.2 \pm 0.1_{\rm stat} \pm 0.2_{\rm sys}$.

6.2 Possible Associations

Like PSR J1718−3825, PSR J1809−1917 appears to be a Vela-like pulsar, as it is also of comparable age and has a similar spin period, 83 ms. As mentioned

before, the offset of the VHE γ-ray emission from the pulsar position is not atypical compared with other probable PWNe associations.

The best fit position of HESS J1809−193 is located at a distance of ∼0.2 deg east of the pulsar PSR J1809−1917, while the peak of the VHE γ-ray emission is at ∼0.2 deg to the south of the pulsar. Its spin-down flux $\dot{E}/d^2$, on the order of 10^{35} erg kpc^{-2} s^{-1}, implies an efficiency of $\epsilon_\gamma \equiv L_\gamma/\dot{E} = 1.2\,\%$, assuming it powers the whole emission from HESS J1809−193 (see Table 6.2).

PSR J1809−1917 – HESS J1809−193						
Spin-down luminosity (erg s^{-1})	Spin-down age (kyr)	Distance (kpc)	1−10 TeV Flux (erg cm^{-2}s^{-1})	Size (pc)	Offset (pc)	$L_\gamma/\dot{E}$ ((1−10) TeV)
1.8×10^{36}	51	3.7 (3.5)	1.3×10^{-11}	35	13	1.2 %

TABLE 6.2: HESS J1809−193 as a PWN and some of the properties of the possibly associated pulsar PSR J1809−1917, taken from Manchester et al. (2005). See Table 5.2 for details on the presented parameters.

The multi-wavelength picture for HESS J1809−193 is very complicated. Figure 6.4 shows the diffuse ASCA source G11.0+0.0
(Bamba et al., 2003; Brogan et al., 2004, 2006) coinciding with the peak of the VHE γ-ray emission, which makes it a possible X-ray counterpart to
HESS J1809−193. The flux of this X-ray source is $\sim 3.8 \times 10^{-12}$ erg cm^{-2} s^{-1} and its photon index ~ 1.6 in the energy range (0.7 – 10) keV. Based on its X-ray spectrum, it was suggested that this source could be a plerionic SNR. The source distance is estimated to be 2.6 kpc, while PSR J1809−1917 is estimated to be 3.5 kpc away, however, this does not rule out the association between the ASCA source and PSR J1809−1917 as both distance estimates suffer from large systematic uncertainties. A further hint for the VHE γ-ray emission coming from a PWN is found in public Chandra data. There appears to be a PWN visible coincident with PSR J1809−1917, that apparently shows a cometary "tail" structure near the position of the pulsar, on a much smaller scale than the γ-ray emission (Sanwal et al., 2005). Future X-ray observations should give more insight into its morphology.

The most prominent source in the ROSAT data is the SNR G11.2−0.3, which lies just outside the significant VHE γ-ray emission region and surrounds the X-ray emitting pulsar PSR J1811−1925 (marked with a red triangle). As the pulsar is associated with G11.2−0.3, which is estimated to be at a distance of $\sim$ 4.4 kpc, it is powerful enough to emit VHE γ-rays, as its spin-down flux is then 3.3×10^{35} erg kpc^{-2} s^{-1}. However, in this case, an association with the H.E.S.S. source is highly unlikely. As Chandra has revealed, the pulsar is very

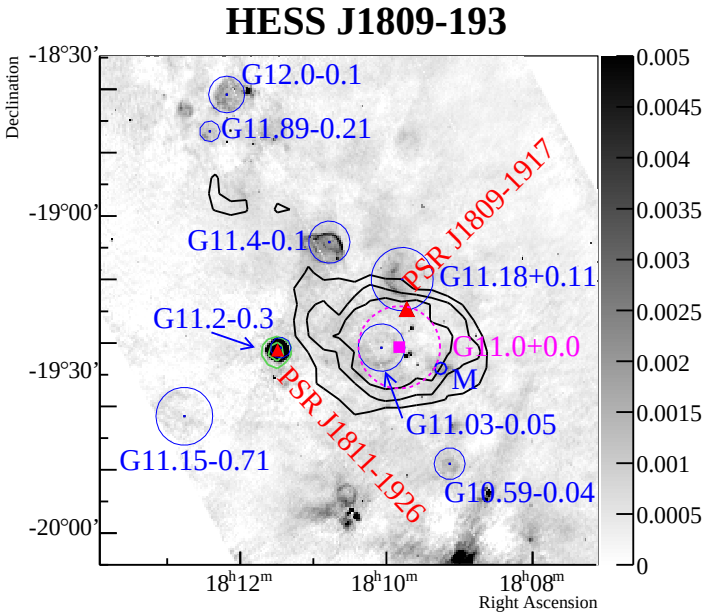

FIGURE 6.4: Radio image from the MAGPIS survey at 1.4 GHz (Helfand et al., 2006) (in Jy/beam). The H.E.S.S. significance contours are overlaid in black and pulsar positions are marked with red triangles. Adaptively smoothed ROSAT hard-band X-ray contours are shown in green (Voges et al., 2001). Blue circles indicate catalogued positions and sizes of nearby SNRs (Green, 2004) and SNR candidates (Brogan et al., 2006). The position of the ASCA source G11.0+0.0 is marked with a magenta square and its size is indicated with a dashed magenta circle (Bamba et al., 2003). The most prominent source in the ROSAT data is the SNR G11.2−0.3, which surrounds the X-ray emitting pulsar PSR J1811−1925 (Kaspi et al., 2001). The MAGPIS SNR candidate 10.8750+0.0875 is labeled *M* (Helfand et al., 2006).

close ($\leq 8''$) to the geometric centre of the shell and its PWN is shown to lie within the SNR (Kaspi et al., 2001). Thus it seems improbable that PSR J1811−1925 could have produced an extremely offset VHE γ-ray PWN due to its motion, as it seems to not yet have left its SNR shell.

Finally, PSR J1809−1917 might also be associated with the SNR candidates G11.03−0.05, G11.18+0.11 (Brogan et al., 2004, 2006), or with the MAGPIS SNR candidate 10.8750+0.0875 (Helfand et al., 2006), which are all located within the VHE γ-ray emission region. Given the small angular sizes of these SNRs, none of them is likely to be responsible for the bulk of the VHE γ-ray emission.

To summarise, the multi-wavelength picture for HESS J1809−193 is very complicated. Though the bulk of the emission can be explained by a PWN powered by PSR J1809−1917, several SNRs as well as another PWN may contribute to

the observed VHE γ-ray emission. Deeper observations in both γ-ray and X-ray wavebands are needed to conclusively distinguish the origin of the signal.

Chapter 7

Systematic Search for the VHE γ-ray Emission of Pulsars

In this chapter a systematic search for VHE γ-ray sources associated with high spin-down energy loss rate pulsars is presented. It is investigated how the probability to detect in VHE γ-rays PWNe surrounding known pulsars varies with the spin-down energy loss rate of the pulsar, testing the plausible assumption that the VHE γ-ray output of a PWN correlates in some fashion with the power of the pulsar feeding it.

An estimate of the chance coincidences between radio pulsars and VHE γ-ray sources is given by the generation of random pulsar samples, which follow the distribution of the PMPS pulsars[1], and checking the H.E.S.S. data for significant VHE γ-ray emission at the random "pulsar" positions. This can be used to evaluate the statistical significance of the association.

As discussed in Section 4.1, taking into account the properties of known VHE γ-ray PWNe the search is optimized for slightly extended sources, allowing for small offsets from the pulsar positions. The sky map shown in Figure 4.1 is used to look up the significance of a VHE γ-ray excess at the position of the radio pulsars as well as for the randomly generated test positions. Each excess is determined by counting VHE γ-ray candidates within $\theta \leq 0.22$ deg of a given position and subtracting a background estimated from areas in the same field of view. An excess significance of at least 5 standard deviations above background is required as a signature of a VHE γ-ray signal. Given the modest number of trials - the 435 pulsar locations - the number of false detections is negligible with this requirement and in any case small compared to the probability for chance coincidences between radio pulsars and VHE γ-ray sources. The pulsars are ranked by their spin-down energy flux $\dot{E}/d^2$ and are grouped into 9 bands of $\log(\frac{\dot{E}/d^2}{\mathrm{erg\,s^{-1}\,kpc^{-2}}})$, ranging from[2] $\log(\dot{E}/d^2) = 27$ to $\log(\dot{E}/d^2) = 36$. To derive

[1] From here, "PMPS pulsars" refers to the sample of 435 pulsars in the search region.

[2] In the following, "$\log(\dot{E}/d^2)$" refers to $\log(\frac{\dot{E}/d^2}{\mathrm{erg\,s^{-1}\,kpc^{-2}}})$.

$\dot{E}/d^2$, the pulsar distances resulting from Taylor and Cordes (1993) were used. A comparison with pulsar distances updated according to Cordes and Lazio (2002) gives consistent results.

In Section 7.1, the results of the search for significant VHE γ-ray emission at the positions of the PMPS pulsars is summarised. The modelling of the parent population and the outcome of the simulation of random pulsar samples is presented in Section 7.2. The evaluation of the statistical significance of the PMPS pulsar associations with VHE γ-ray sources is shown in Section 7.3. Finally, in Section 7.4 a check to verify the stability of the results is presented.

7.1 PMPS Pulsars

As mentioned in Section 4.3, 30 out of the 435 PMPS pulsars are found with significant VHE γ-ray emission at the pulsar location[3]. Table 7.1 summarises the detection significances for all detected PMPS pulsars, ranked by $\dot{E}/d^2$.

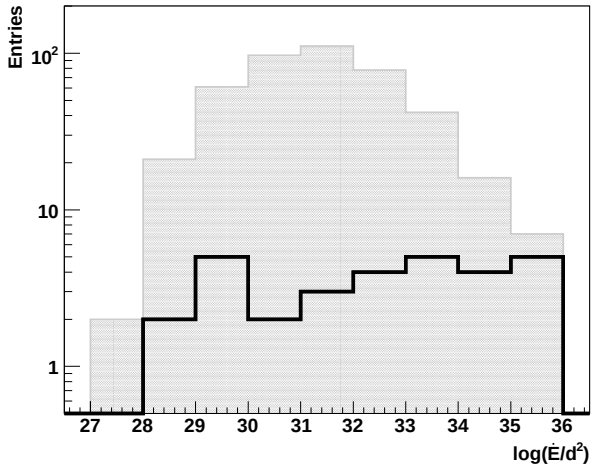

FIGURE 7.1: $\dot{E}/d^2$ distribution of all (grey histogram) and detected (black line) PMPS pulsars.

In Figure 7.1, the $\dot{E}/d^2$ distribution of all PMPS pulsars is shown as a grey histogram, while the distribution of the detected PMPS pulsars is marked with the black line. It can be seen that to higher values of $\dot{E}/d^2$ a larger fraction of pulsars gets detected. The fraction of detected pulsars is about 5% for pulsars with spin-down flux below 10^{33} erg s^{-1}kpc^{-2} and increases to about 70% for

[3]From now on, "pulsar with significant VHE γ-ray emission at the pulsar position" is substituted by "detected" pulsar. Note that this does not imply a firm association between the VHE γ-ray signal and the pulsar.

PSR	PSR	$\dot{E}/d^2$ (erg s^{-1} kpc^{-2})	Significance (σ)
J1747−2802	-	3.1×10^{28}	13.8
J1303−6305	-	3.8×10^{28}	28.0
J1837−0653	B1834−06	1.8×10^{29}	17.7
J1302−6313	-	3.5×10^{29}	28.0
J1702−4217	-	6.8×10^{29}	8.2
J1305−6256	-	8.5×10^{29}	8.2
J1614−5144	-	8.9×10^{29}	11.9
J1616−5109	-	1.2×10^{30}	10.4
J1824−1423	-	9.1×10^{30}	8.0
J1823−1347	-	1.3×10^{31}	9.4
J1633−4805	-	6.0×10^{31}	7.5
J1822−1400	B1820−14	6.0×10^{31}	8.1
J1625−4904	-	1.1×10^{32}	5.0
J1630−4733	B1626−47	1.1×10^{32}	6.0
J1613−5211	-	2.1×10^{32}	8.3
J1806−2125	-	4.3×10^{32}	5.9
J1632−4757	-	1.0×10^{33}	8.2
J1514−5925	-	1.7×10^{33}	15.7
J1301−6310	-	1.8×10^{33}	22.8
J1841−0524	-	4.4×10^{33}	7.9
J1301−6305	-	6.7×10^{33}	24.5
J1702−4128	-	1.3×10^{34}	6.2
J1614−5048	B1610−50	3.0×10^{34}	7.5
J1302−6350	B1259−63	3.9×10^{34}	9.5
J1718−3825	-	7.0×10^{34}	7.9
J1809−1917	-	1.3×10^{35}	6.8
J1803−2137	B1800−21	1.4×10^{35}	15.7
J1826−1334	B1823−13	1.7×10^{35}	20.9
J1420−6048	-	1.8×10^{35}	21.2
J1513−5908	B1509−58	9.2×10^{35}	44.8

TABLE 7.1: Detection significances of PMPS pulsars with significant γ-ray emission at the pulsar location (at least 5 standard deviations above the background), ranked by $\dot{E}/d^2$. Where existing, the pulsar name in coordinates of the B1950 epoch is given.

pulsars with $\dot{E}/d^2$ above 10^{35} erg s^{-1}kpc^{-2}. In the two highest bands, in the range of $\log(\dot{E}/d^2) = (34 - 36)$, 9 out of 23 pulsars are detected. In more detail, in the band $\log(\dot{E}/d^2) = (34 - 35)$, 4 out of 16 pulsars are detected and in the highest band of $\log(\dot{E}/d^2)$, 5 out of 7 pulsars are detected. This is an interesting

result, which indicates that the assumption that the VHE γ-ray output of a PWN correlates with the power of the pulsar feeding it is indeed plausible. Not all of these associations are necessarily genuine. To evaluate the significance of the detection of VHE γ-ray emission from pulsars with high $\dot{E}/d^2$, an estimate of the chance coincidences between VHE γ-ray sources and pulsars is essential.

7.2 Simulation

To estimate the rate of chance coincides between pulsars and VHE γ-ray sources, the PMPS sample has to be modelled with regard to the pulsar positions in Galactic coordinates and their $\dot{E}/d^2$. Figure 7.2 shows once more the distribution of the PMPS pulsars. In the left panel, their distribution in Galactic coordinates reveals no significant clustering at any specific Galactic longitude. As expected, the distribution is more dense closer to the Galactic plane. To account for the aforementioned wandering of the pulsars off the Galactic plane while getting older, their distribution in $\dot{E}/d^2$ versus Galactic latitude (right panel) has to be modelled as well.

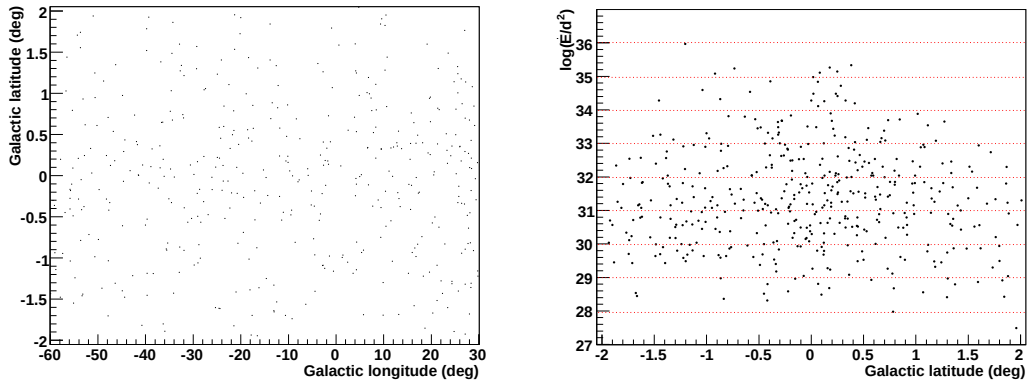

FIGURE 7.2: PMPS search sample: distribution in Galactic coordinates (*left*) and in $\dot{E}/d^2$ versus Galactic latitudes (*right*), where the bands in $\log(\dot{E}/d^2)$ are indicated in red dotted lines.

Therefore, the following ansatz is chosen for the density distribution of the Monte Carlo generated control sample:

$$\rho(\lambda, \beta, \dot{E}/d^2) = \rho(\lambda)\rho(\beta, \dot{E}/d^2), \tag{7.1}$$

where λ and β is the Galactic longitude and latitude, respectively.

To model the longitude distribution, a fourth order polynomial is fit to it, displayed in the left panel of Figure 7.3. The distribution along the Galactic plane is fairly flat over the search range, with a decrease towards smaller longitudes.

The error bars shown in this plot result from the assumption of Poisson statistics and thus amount to $\sqrt{\text{Entries}}$ in each bin of Galactic longitude. The simulation has been tested for different distributions in Galactic longitudes (e.g. a completely flat one) and it was found that this does not affect the results significantly.

For the $\dot{E}/d^2$ versus Galactic latitude distribution, a Gaussian is fit to the distribution of pulsars in each of the bands shown as red dotted lines in the right panel of Figure 7.2. The widths of these Gaussians are plotted against the corresponding $\dot{E}/d^2$, the result of which is presented in the right panel of Figure 7.3. The error bars in this plot are the errors on the widths from the respective Gaussian fits. However, if the error on the width is bigger than 2, the RMS (and the error on the RMS) is taken from the distribution itself, rather than the width of the Gaussian fit. This is the case in the first band, $\log(\dot{E}/d^2) = (27-28)$, as here the fit does not work properly due to low statistics. The error on the width in the last band, $\log(\dot{E}/d^2) = (35-36)$ is quite large, as the distribution of the 7 pulsars (expected to be distributed around 0 as for all $\log(\dot{E}/d^2)$ bands) is slightly asymmetrical and thus hard to fit. To account for possible systematic uncertainties, two different parametrisations of the distribution are used. As can be seen from Figure 7.3, a very conservative approach is taken by roughly following the upper and lower error bands. The fit of a first order polynomial to the distribution is drawn as a dotted line and indicates the expected decrease of the width of the Galactic latitude with increasing $\log(\dot{E}/d^2)$.

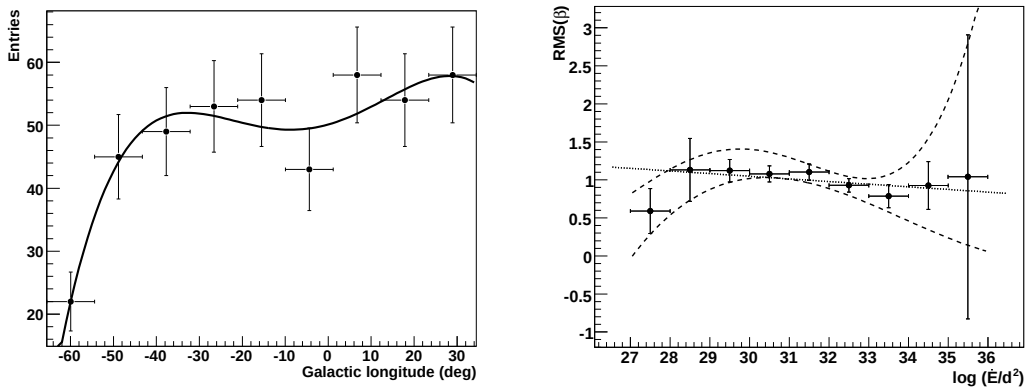

FIGURE 7.3: Modelling of the parent population: the distribution in Galactic longitudes with Poisson error bars (*left*) is fit by a fourth order polynomial. The distribution of the width(Galactic latitude) versus $\dot{E}/d^2$ (*right*) is represented in different simulations by one of the two parametrisations following roughly the upper and lower error bars (dashed lines), accounting for the uncertainty of the distribution. The dotted line shows the fit of a first order polynomial to the distribution. The error bars represent the errors on the widths of the Gaussian fits (refer to text for more details).

With the distributions shown in Figure 7.3 and the left panel of Figure 4.6, a sample of random "pulsars" can be generated. The value for the Galactic longitude is picked randomly from the fit to the distribution of Galactic longitudes. A random value for $\dot{E}/d^2$ is picked from the distribution in $\dot{E}/d^2$ (left panel of Figure 4.6), and the value for the corresponding Galactic latitude is looked up from the chosen parametrisation representing the width(Galactic latitude) versus $\dot{E}/d^2$ distribution.

Following this procedure, 10^6 realisations of random pulsar samples are generated, each sample consisting on average of 435 "pulsars" (implemented by picking a number for the sample size from a Gaussian distribution with mean 435 and width $\sqrt{435}$), and the rate of chance coincidences between VHE γ-ray sources and the PMPS pulsars is estimated. Looking up the significances for a VHE γ-ray excess in the sky map shown in Figure 4.1 at these random positions, the distribution in $\dot{E}/d^2$ of the chance detections is compared to the one for the PMPS pulsars, as shown in Figure 7.4.

7.3 Significance of PMPS Pulsar Associations with VHE γ-ray Sources

Figure 7.4 shows the distribution in $\dot{E}/d^2$ of the chance detections (dark grey histogram) and of the detected PMPS pulsars (black line) on top of the distribution for all PMPS pulsars (light grey histogram). It is obvious that towards

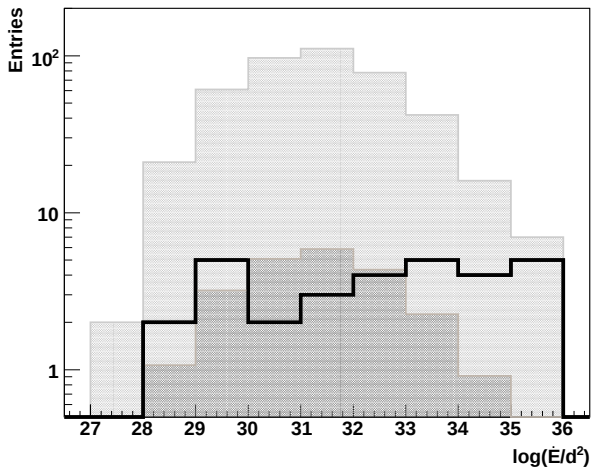

FIGURE 7.4: $\dot{E}/d^2$ distribution of all (light grey histogram) and detected (black line) PMPS pulsars, as well as of the chance coincidences, i.e. the detections from simulated "pulsars" (dark grey histogram).

larger values of $\dot{E}/d^2$ the detections from the PMPS sample cannot be explained by chance coincidences.

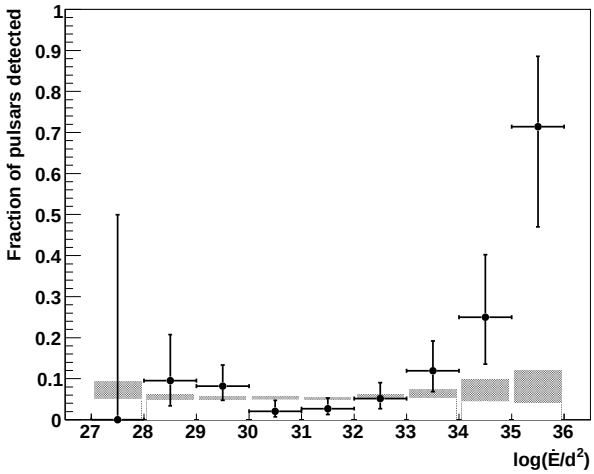

FIGURE 7.5: The black dots show the fraction of PMPS pulsars with significant VHE γ-ray excess at the pulsar position, as a function of $\log(\dot{E}/d^2)$. The two-sided binomial error bars give the 68% confidence range for the probability to find a VHE γ-ray source at the pulsar location. The shaded band represents the probability for a chance coincidence. The width of the band accounts for the uncertainty in the width of the latitude distribution of pulsars indicated by the two different parametrisations in the right panel of Figure 7.3.

In Figure 7.5 the black dots represent the fraction of PMPS pulsars with significant VHE γ-ray excess at the pulsar position in each $\log(\dot{E}/d^2)$ band. The two-sided binomial error bars give the 68% confidence range for the probability to find a VHE γ-ray source at the pulsar location (after Clopper and Pearson (1934)). The upper and lower boundary of the confidence interval are calculated as following:
Given a total of N pulsars of which n get detected in VHE γ-rays, the percentage p of pulsars to emit VHE γ-rays are searched for. The distribution of detectable pulsars is given by the binomial distribution:

$$b(n, N, p) = \binom{N}{n} p^n (1-p)^{N-n}. \tag{7.2}$$

For a confidence interval $c \in]0, 1[$ the lower boundary p_- and the upper boundary p_+ are given as:

$$\mathbf{n = 0:} \quad p_- = 0 \quad p_+ = 1 - \left(\frac{1-c}{2}\right)^{\frac{1}{N}} \tag{7.3}$$

$$\mathbf{n = N:} \quad p_- = \left(\frac{1-c}{2}\right)^{\frac{1}{N}} \quad p_+ = 1 \tag{7.4}$$

$\mathbf{0 < n < N:}$

here, p_- and p_+ are derived from the solutions of the equations:

$$f_-(p_-) = \frac{1+c}{2} \quad f_+(p_+) = \frac{1+c}{2}, \tag{7.5}$$

with

$$f_-(p_-) = \sum_{i=0}^{n-1} b(i, N, p_-) = 1 - \sum_{i=n}^{N} b(i, N, p_-) \tag{7.6}$$

$$f_+(p_+) = \sum_{i=n+1}^{N} b(i, N, p_+) = 1 - \sum_{i=0}^{n} b(i, N, p_+) \tag{7.7}$$

In Equations 7.6 and 7.7, the sum with less numbers of summands should be used for efficiency and numerical stability. Technically, solving these equations can be done using a binary search.

The expected fraction of chance coincidences is shown as dark shaded bands in Figure 7.5 and varies between 4% to 12%. The widths of the bands account for the uncertainty in the width of the latitude distribution of pulsars and were evaluated by repeating the analysis for the two different parametrisations in the right panel of Figure 7.3. All associations with pulsars with $\dot{E}/d^2 < 10^{34}$ erg s^{-1} kpc^{-2} are within statistical errors consistent with chance coincidences. Indeed for plausible values of the ratio between the γ-ray luminosity and the pulsar spin-down energy loss, $L_\gamma/\dot{E}$, no detectable emission would be expected from such pulsars. However, the detection of emission from high-power pulsars is statistically significant. The probability that the detection of VHE γ-ray sources coincident with 9 or more of the total of 23 pulsars above $\dot{E}/d^2 > 10^{34}$ erg s^{-1} kpc^{-2} results from a statistical fluctuation is $\sim 3.4 \times 10^{-4}$. For the last band, $\log(\dot{E}/d^2) = (35 - 36)$, the chance probability to detect 5 or more of the total of 7 pulsars is $\sim 4.2 \times 10^{-4}$.

These results demonstrate for the first time that a large fraction of high-luminosity pulsars correlate with sources of VHE γ-rays, emitting with a VHE γ-ray luminosity of order 1% of the pulsar spin-down power (see Table 4.3). The positive correlation does not necessarily imply that the pulsar or PWN itself is responsible for the VHE γ-ray flux. It could also result from some other mechanism correlated with the pulsar or its creation, such as a supernova shock wave. However, the correlation found between VHE γ-ray detectability and spin-down flux $\dot{E}/d^2$ argues in favour of a pulsar-related origin of the VHE γ-ray signal. On the other hand, for the PMPS pulsar sample, $\dot{E}/d^2$ also correlates closely with the spin-down age T of the pulsar (as shown in Figure 4.7), $\dot{E}/d^2 \sim T^{-3/2}$, and

obviously with distance d, both parameters relevant for determining the VHE γ-ray flux from shock wave driven supernova remnants.

The exact relation between pulsar parameters and VHE γ-ray luminosity is an interesting issue. Variations in exposure and hence in detection threshold over the survey range, as well as the uncertainty in pulsar distance will smear out the turn-on curve of detectability versus $\dot{E}/d^2$ shown in Figure 7.5, but cannot fully account for the rather slow turn-on over a range of more than one order of magnitude in $\dot{E}/d^2$, combined with a detection probability below unity for even the highest-power pulsars. This indicates that $\dot{E}/d^2$ cannot be the only parameter relevant for the VHE γ-ray flux.

The same conclusion is obtained from the observed variation of the ratio of the γ-ray luminosity to the spin-down luminosity, $L_\gamma/\dot{E}$, of about an order of magnitude among the detected pulsars (see Table 4.3). With the selected most energetic pulsars from the PMPS sample, which were presented in Table 4.3 in Section 4.3, the possible correlation of the VHE γ-ray emission with the spin-down energy flux of the pulsar as well as the possible correlation of some pulsar parameters can be examined. In Figure 7.6, the VHE γ-ray flux is shown as a function of the spin-down energy flux $\dot{E}/d^2$. For detections, the VHE γ-ray fluxes between (1 – 10) TeV are marked in red, while for non-detections the energy flux limits between (1 – 10) TeV (at 99% confidence level) are marked in black. No clear correlation can be seen. The sub-sample of detections seems to show an indication for a rise in the flux with higher $\dot{E}/d^2$, however, the outliers weigh heavily on these small statistics.

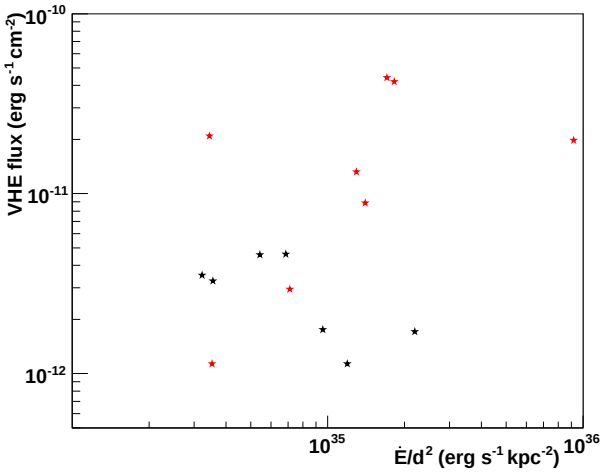

FIGURE 7.6: VHE γ-ray flux versus spin-down energy flux $\dot{E}/d^2$. For detections, the VHE γ-ray fluxes between (1 – 10) TeV are marked in red, while for non-detections the energy flux limits between (1 – 10) TeV (at 99% confidence level) are marked in black.

Expecting the size of the PWN to increase during the lifetime of the pulsar, plotting the size of the VHE γ-ray emission over the age of the pulsar should result in a positive correlation. However, in Figure 7.7 no unambiguous correlation can be found. This could be due to different ambient media restricting the evolution and thus the size of the PWN.

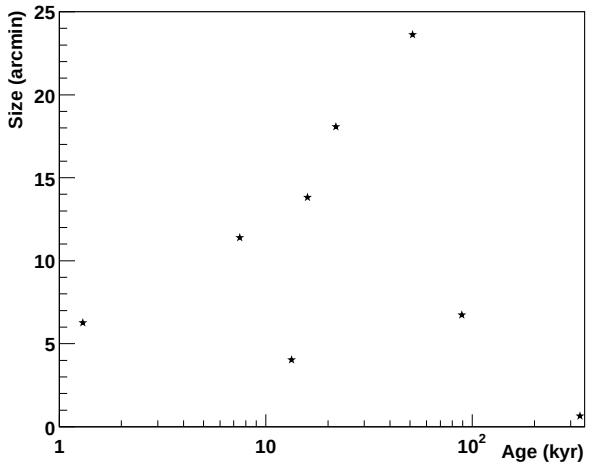

FIGURE 7.7: Size of the VHE γ-ray emission versus the age of the pulsar.

As it is expected that pulsars receive a certain kick velocity at birth and thus to move away from their original position, the offset of the pulsar from the best-fit position of the VHE γ-ray emission should increase with the age of the pulsar. However, as can be seen in Figure 7.8, no positive correlation becomes obvious.

For completeness, in Figure 7.9 the offset of the pulsar from the best-fit position of the VHE γ-ray emission versus the size of the VHE γ-ray emission is plotted. Here, an indication for a positive correlation seems to show up, as would be expected for pulsars born with a certain kick velocity as they would move towards the edge of their PWN during their lifetime.

These results show that this present pulsar sample is too small to properly investigate the dependence of L_γ on multiple pulsar parameters. However, to improve the systematic study, not only more data in VHE γ-rays are needed, but also the precision of crucial pulsar parameters like the distance has to increase and a better understanding of the pulsar as a system with the variables spin-down luminosity, age, distance and influence of the ambient medium has to be achieved.

Apart from this, a constant $L_\gamma/\dot{E}$ is not necessarily expected. For a given age, the integral energy fed by the pulsar into the PWN increases with $\dot{E}$. Apart from expansion losses, pulsar spin-down power is shared between particle energy and

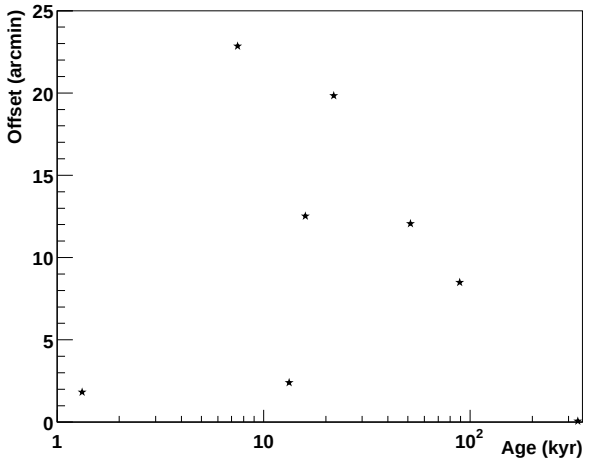

FIGURE 7.8: Offset of the pulsar from the best-fit position of the VHE γ-ray emission versus the age of the pulsar.

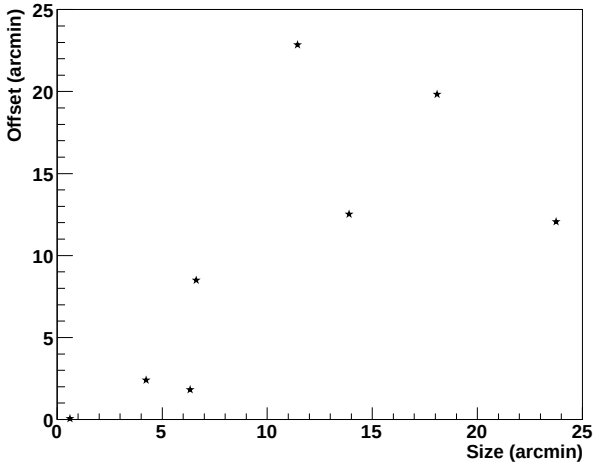

FIGURE 7.9: Offset of the pulsar from the best-fit position of the VHE γ-ray emission versus the size of the VHE γ-ray emission.

magnetic field energy. Assuming equipartition between the two energy densities (Reynolds and Chevalier, 1984; Rees and Gunn, 1974), the magnetic field in the PWN will increase with $\dot{E}$ and hence the energy loss by synchrotron radiation will increase relative to and at the expense of IC γ-ray production. Indeed, unpulsed X-ray luminosity of pulsars is observed to increase faster than $\dot{E}$, with

$L_X \propto \dot{E}^{1.4\pm0.1}$ (Cheng et al., 2004). In such scenarios, magnetic field values and therefore the balance between X-ray and VHE γ-ray emission will also depend on volume, i.e. on the expansion speed of the nebula and hence on the ambient medium. In addition, the current spin-down luminosity $\dot{E}$ may not be the only relevant scale; if the pulsar age is shorter than or comparable to the electron cooling time, relic electrons injected in early epochs with higher spin-down power will still contribute and may enhance L_γ significantly compared to the quasi-steady state achieved for old pulsars.

7.4 Check of the Simulation: additional Selection of Pulsars

In this section an slightly different method of evaluating pulsar detection probabilities is presented, which serves mainly to demonstrate that the experimental results shown in Figure 7.5 are stable and do not depend on details of the statistical procedure. Given the high density of pulsars compared to the angular resolution of H.E.S.S., a single VHE γ-ray source may even coincide with more than a single pulsar, and thus appear more than once amongst the "detections" in Figures 7.4 & 7.5. To verify that multiple counting – which is properly accounted for by the simulation – has indeed no influence on the result, an angular separation of pulsars is introduced here. Pulsars located within twice the integration radius (0.44 degrees) of a pulsar with higher $\dot{E}/d^2$ are excluded, since the emission from the two objects cannot be separated and a significant signal is likely to be associated with the stronger pulsar. Pulsars located within a known non-pulsar-related VHE γ-ray source, Sgr A, RX J1713.7−3946 and extended diffuse emission in the Galactic ridge, are also excluded, taking their 5-standard-deviations significance contours as the source extension. By design, these exclusions mainly remove low-luminosity pulsars. They guarantee that any detection of a pulsar in a given $\dot{E}/d^2$ band cannot be caused by a nearby higher-luminosity pulsar or a known non-pulsar source. The selection does introduce a bias in the sense that detections are preferentially attributed to highest-luminosity pulsars, but this bias is again accounted for in the simulated pulsar samples and in the chance probabilities derived from these samples. From the 435 pulsars, 283 are left after this selection. Their distribution in $\dot{E}/d^2$ is shown as a light grey histogram in Figure 7.10, along with the detections in this reduced sample (black line) and the distribution of the detections from the simulated "pulsars" (dark grey histogram).

The resulting probability for VHE γ-ray emission at the pulsar positions is shown in Figure 7.11 and confirms the result in Figure 7.5. For the remaining isolated low-luminosity pulsars the probability for an association with a VHE γ-ray source is further reduced, and is well explained by chance coincidences. Of

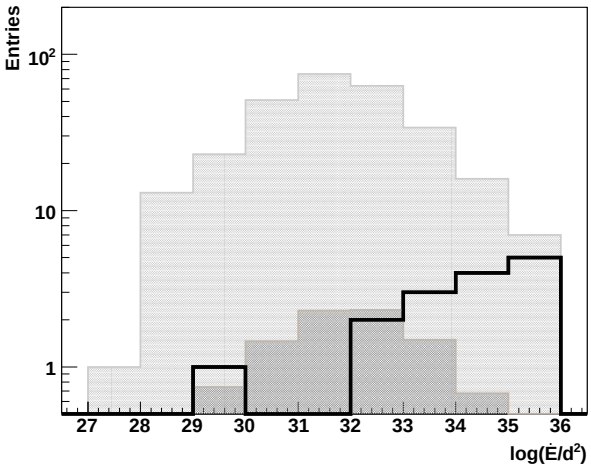

FIGURE 7.10: $\dot{E}/d^2$ distribution of all (light grey histogram) and detected (black line) PMPS pulsars, as well as of the chance coincidences, i.e. the detections from simulated "pulsars" (dark grey histogram), after rejecting faint pulsars overlapping with stronger pulsars, or pulsars coinciding with known non-pulsar-related VHE γ-ray sources.

the strong pulsars with $\dot{E}/d^2 > 10^{34}$ erg s^{-1} kpc^{-2}, none is rejected and the result is unchanged. For this selection of pulsars, the probability that the detection of VHE γ-ray sources coincident with 9 or more of the total of 23 pulsars above $\dot{E}/d^2 > 10^{34}$ erg s^{-1} kpc^{-2} results from a statistical fluctuation is $\sim 5.1 \times 10^{-5}$. For detection of 5 or more of the total of 7 pulsars above 10^{35} erg s^{-1}kpc^{-2}, the chance probability is $\sim 1.1 \times 10^{-4}$.

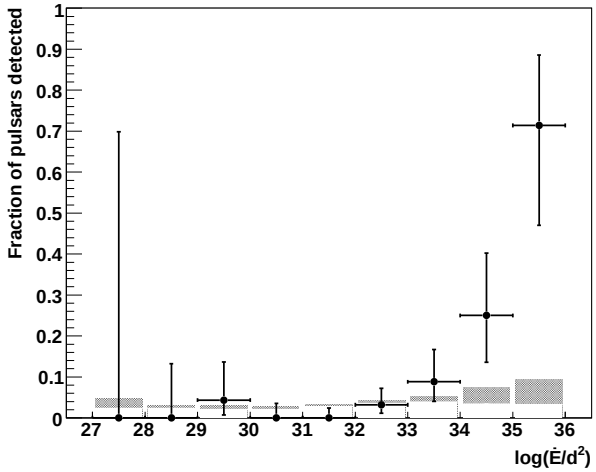

FIGURE 7.11: Having rejected faint pulsars overlapping with stronger pulsars, or pulsars coinciding with known non-pulsar-related VHE γ-ray sources: the black dots show the fraction of PMPS pulsars with significant VHE γ-ray excess at the pulsar position and the shaded bands represent the probability for a chance coincidence. See the caption of Figure 7.5 for more details.

Conclusion

A systematic study of a connection between high-power pulsars and VHE γ-ray sources is presented in this work, based on a deep survey of the inner Galactic plane conducted with the H.E.S.S. telescopes. Due to its large field of view in combination with its unprecedented sensitivity, H.E.S.S. is the first instrument to allow for such surveys in VHE γ-rays. The motivation for this study is that though a significant quantity of new VHE γ-ray sources can be identified as PWNe, details of the energy conversion mechanisms in the vicinity of pulsars are not well understood and is it not known if all pulsars drive PWNe and produce VHE γ-ray radiation. Therefore it is investigated how the probability to detect in VHE γ-rays PWNe surrounding known pulsars varies with the spin-down energy loss of the pulsar, testing the plausible assumption that the γ-ray output of a PWN correlates in some fashion with the power of the pulsar feeding it.

It is shown that pulsars with large spin-down energy flux are indeed with high probability associated with VHE γ-ray sources. This implies that these pulsars emit on the order of 1% of their spin-down energy in TeV γ-rays. Extrapolated over the full energy range, our observations prove the existence of an efficient mechanism by which a large fraction of the pulsar spin-down power is converted into kinetic energy of particles. The positive correlation could also result from some other mechanism correlated with the pulsar or its creation, such as a supernova shock wave. However, the correlation found between VHE γ-ray detectability and spin-down flux $\dot{E}/d^2$ argues in favour of a pulsar-related origin of the VHE γ-ray signal.

The search for VHE γ-ray emission close to pulsars with large spin-down energy flux led to the discovery of two VHE γ-ray sources, HESS J1718−385, associated with the pulsar PSR J1718−3825, and HESS J1809−193, associated with the pulsar PSR J1809−1917. The morphology and the energy spectra of both new sources are examined and details of the H.E.S.S. analysis are exemplarily demonstrated, such as different techniques for the evaluation of the background in the case of HESS J1718−385. The probable associations of the VHE γ-ray sources with their respective pulsars are investigated by evaluating broad-band information around the objects. Compared with the general sample used in the systematic study, the associated VHE γ-ray emission of both new sources seems to fit into the emerging picture of γ-ray PWNe. However, the multi-wavelength

picture for HESS J1809−193 is very complicated. Though the bulk of the emission can be explained by a PWN powered by PSR J1809−1917, several SNRs as well as another PWN may contribute to the observed VHE γ-ray emission. Deeper observations in both γ-ray and X-ray wavebands are needed to conclusively distinguish the origin of the signal. HESS J1718−385 on the other hand may well represent the first VHE γ-ray PWN found in a systematic search for pulsar associations, despite the present lack of a PWN detection in other wavebands. The remarkable similarity between HESS J1718−385 and other known VHE γ-ray PWNe, together with the lack of other probable counterparts, gives additional confidence.

The results from the systematic study suggest it to be very likely that future more sensitive γ-ray instruments will detect a rapidly increasing number of lower-luminosity PWNe. The expected increase in the number of detections of VHE γ-ray PWNe will not only help in the search for the emission mechanisms in pulsars, but possibly show that VHE γ-rays are a useful tool for discovering more of these types of objects. To improve the systematic study, not only more data in VHE γ-rays are needed but also the precision of crucial pulsar parameters like the distance has to increase and a better understanding of the pulsar as a system with the variables spin-down luminosity, age, distance and the influence of different environments has to be achieved.

Appendix A

The Smart Pixel Camera

The next generation of Imaging Atmospheric Cherenkov Telescopes (IACTs) will aim for lower energy thresholds on the order of a few GeV and an increase in sensitivity up to energies of about 100 TeV. These telescopes will have large mirrors (with areas of ~ 500 m^2), cameras with several thousand pixels and a field of view of $5^\circ - 10^\circ$. The increased mirror size will lead to significantly higher trigger rates and thus the amount of data to be processed will be much larger than for the current systems. As H.E.S.S. has shown the stereoscopic reconstruction of Cherenkov showers to be a very successful approach, it is likely that future IACT systems will consist of several telescopes. Therefore cameras for these systems have to be designed with regard to reduction of costs and easy maintenance.

VHE γ-rays induce Cherenkov showers, of which each a few hundred photons can reach the camera within a few nanoseconds. With respect to high performance and low costs, to date photomultiplier tubes (PMTs) are the best devices to record such short, weak signals. Therefore the cameras are divided into coarse pixels on the order of 0.1° (depending on the focal length). The PMT signals have to be integrated over a very short time interval ($\sim 10\,\text{ns} - 15\,\text{ns}$) to suppress contamination of the shower signal by coincident photons from the night sky background (NSB). An efficient trigger is needed to distinguish between shower events and the dominating background.

The Smart Pixel Camera (SPC) owes its name to the fact that all the main functions of the camera are situated on the pixel, like signal integration, trigger logic, time measurement and monitoring. In the scope of this work, parts of the driver and analysis software for the prototype were developed and tested and first tests of the functionality of the prototype were performed to establish a basis for more detailed testing. The driver software is designed to be *multi-threaded*, as to allow for continuous monitoring of the status of the system while performing operations. For easy maintenance, the software is divided into several modules, which are running in parallel and exchange data objects via the network. The analysis software is based on C++ and ROOT.

Following the paper by Hauser et al. (2007), in Section A.1 the design of

the SPC hardware and electronics is discussed, the results from detailed test measurements on the prototype are presented in Section A.2 and a brief summary of the results is given in Section A.3.

A.1 Layout of the Smart Pixel Camera

The Smart Pixel (Figure A.1) is the key component of the SPC. It consists of a PMT and the Smart Pixel Electronics (SPE). The SPE comprises a simple cluster trigger, signal integration, arrival time measurement, rate measurement and monitoring channels. All output channels are provided as analog voltage levels.

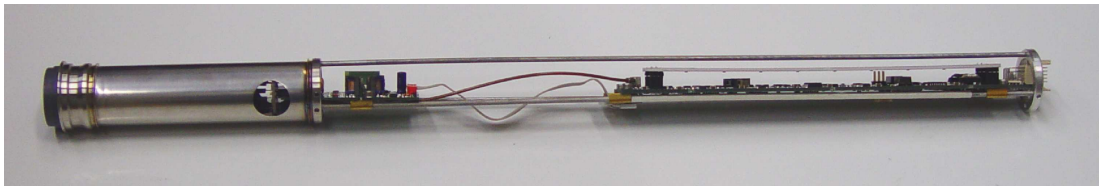

FIGURE A.1: Smart Pixel with the PMT (left), the high voltage supply (middle) and the Smart Pixel Electronics (right).

A segmented backplane provides the power supply as well as the signal lines to the rest of the camera, including an analog signal line, a serial command bus and trigger lines from the neighbouring pixels (see Figure A.2). 16 pixels form a segment, which itself is a logic unit for the programming and the readout and which is controlled by a segment controller. The segment controllers are linked via serial command bus to the camera controller, which controls the programming and the timing of the readout.

The multiplexed analog signals from the pixels are digitised by flash analog digital converters (ADCs) running in multiplexing mode. To decouple the digitisation itself from the reading of the digitised information into the CPU memory, the ADCs are equipped with two separate memory banks which are readout asynchronously. In the prototype the connection between the CPU, the camera controller and the ADCs is implemented by a VME-based system. The whole electronics is hosted by a self-supporting aluminum structure. The connection of the camera to the rest of the system consists of the power supply (in the prototype 220 V), a network cable and trigger connection for the stereoscopic mode in a telescope array.

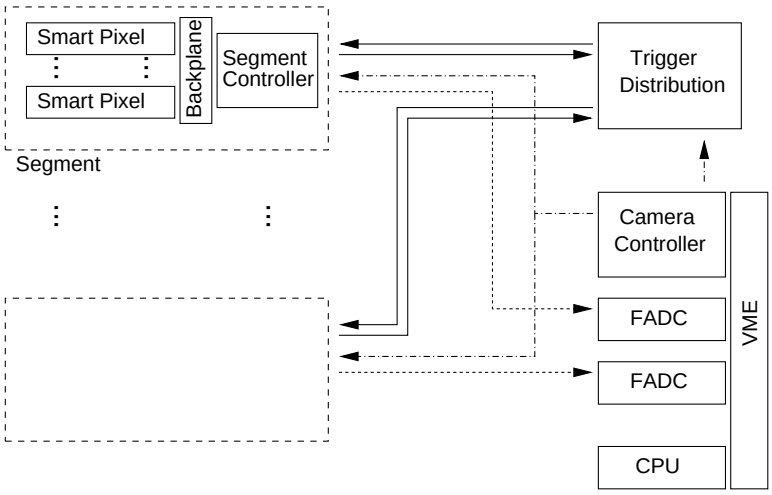

FIGURE A.2: Schematic of the SPC.

Trigger Generation

Due to the huge rate of background events an efficient trigger is needed. The NSB is suppressed by triggering on coincident signals (within a few nanoseconds) in a combination of spatially connected pixels. The trigger of the SPC is implemented on the pixels. To provide both a path for the generation of the trigger and for the signal integration (see below), the signal from the PMT is split into two.

The camera readout is triggered when a required minimum number of neighbouring pixels trigger simultaneously, i.e. when the PMT signal exceeds the discriminator threshold in these pixels. The generation and the distribution of the camera trigger signal takes ∼90 ns. It is very important to ensure that the transit times of the trigger signals from different pixels are as equal as possible, so that the trigger time does not depend on the pixel generating the trigger. See Hauser et al. (2007) for a more detailed description of the trigger generation.

Besides the NSB photons there are also Cherenkov photons from hadron-induced showers (with rates on the order of kHz) as background for IACTs. The hadronic background is excluded offline like in the standard H.E.S.S. analysis (see Chapter 3.4).

Signal Integration

Figure A.3 shows the circuit diagram of the signal integration part of the SPE.

The signal from the PMT has to be delayed for approximately 90 ns, which is the time needed for the generation of the camera trigger signal. This is realised by a delay line implemented as a 12-layer printed circuit board, which consists

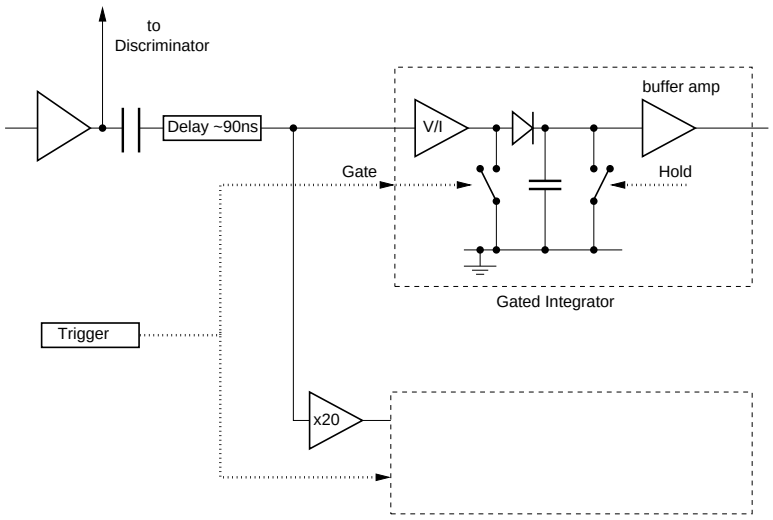

FIGURE A.3: Circuit diagram of the signal integration part of the SPE.

of a meandering electric line with ground lines and ground layers and which is designed to counterfeit a quasi-coaxial structure. The delayed signal is split into a low and a high gain channel (with an amplification ratio of 1:20) in each of which a V/I converter converts the PMT signal to a current that is fed to a gated integrator (see Figure A.3). The incoming charge gets accumulated on the capacitor as long as the Gate switch is open. The gate is opened by the camera trigger. It has a programmable width of 10 ns – 25 ns and can be delayed in single-nanosecond steps to account for different transit times in the PMTs, to ensure that the PMT signal fits optimally into the integration gate. The delay for each pixel is fixed after calibration. The capacitor gets discharged by closing the Hold switch. The resulting integrated signal is an analog voltage level.

Measurement of the signal arrival time can be used in the analysis to correct for lower amplitudes caused by a displacement of the signal with respect to the optimal position in the gate, e.g. due to a delay between the trigger and PMT signal because of time gradients in the shower (see next section).

Arrival Time Information

As hadronic showers are assumed to have different time profiles in comparison to VHE γ-ray showers, the knowledge of the arrival time of the Cherenkov photons at the pixels helps to further suppress the hadronic background as well as improve the image cleaning done offline (see Chapter 3.4). As mentioned above, in the SPC the time information is also used to calibrate the gates for an optimal integration of the PMT signals.

A time to amplitude converter (TAC) measures the time between the camera trigger and the generation of the discriminator signal (i.e. an event above the pixel discriminator threshold occurred) for each pixel. The TAC is started by the camera trigger and stopped by the delayed (by ~ 100 ns) discriminator signal – if the TAC does not get stopped, the pixel did not generate a discriminator signal. With this method the trigger threshold of every pixel can be determined in normal operation mode (see section "Trigger Performance"). Furthermore, the time measurement provides an estimate for the gate width in which chance coincidences in neighbouring pixels lead to a camera trigger.

Monitoring

The SPE provides several monitoring channels which can be read out during normal operation mode:

- PMT anode current: provides information about the NSB and therefore about the discriminator threshold below which the readout is dominated by triggers from chance coincidences. It is measured using an integrator with a time constant of $\sim 700\,\mu$s.
- Discriminator rate / coincidence rate: measured on every pixel by an integrator accumulating a defined signal for every discriminator event / coincidence event (for a given multiplicity).
- Temperature: two temperature sensors are implemented on the SPE to monitor the temperature-critical parts of the electronics.
- Internal voltage levels: the different operation voltage levels ($\pm$3, 5, 12 V) can be read out.

Control/Programming

Each pixel is given a unique address, which is composed of the address of the segment, and the position of the pixel on the segment and can be programmed individually. The time required to program all pixels simultaneously in the broadcast mode is 3.2 μs. The most important functions to be programmed on the pixels are the gate width of the gated integrator, the multiplicity required for the coincidence trigger, delays to fit the PMT pulse optimal into the gate and the voltage on the PMT.

Multiplexing and Digitisation Scheme

The digitisation scheme is controlled and synchronised by the camera controller by several clock and strobe signals.

Multiplexing Scheme

Each pixel provides 14 channels with event and monitoring information: amplitude (high and low gain), TAC, PMT anode current, discriminator / coincidence rate, temperature and further monitoring parameters (e.g. operating voltages, HV status of the PMT). The output of all channels is given as analog voltage levels, which are multiplexed (by a multiplexer on the SPE) onto one line leading to the segment controller. On the segment controller, the signals from its 16 pixels are again multiplexed (by the segment multiplexer) onto one line leading to the ADC. This multiplexing scheme is controlled by the camera controller via a clock signal. The clock frequency is programmable and currently set to 10 MHz. With every clock cycle the segment multiplexer switches to the next pixel and the multiplexer on the previous readout pixel switches to the next channel. The start and stop channel of the pixel multiplexer is programmable. This approach has an advantage in that the many pixel multiplexers can be slow and thus low-priced, and only on the few segment controllers fast, more expensive multiplexers are required, which reduces the costs per pixel drastically.

Digitisation Scheme

The digitisation is done by ADCs (in the prototype SIS3300 from Struck) at the back-end of the camera, controlled by the camera controller. Due to the multiplexing scheme one ADC is needed for every segment. The camera controller provides the clock signal which initiates the digitisation just before the segment multiplexer switches to the next pixel (to ensure that the multiplexer has reached the full charge level of the channel). After readout the gated integrators get discharged and the camera is ready for the next trigger. For each readout channel a time of 1.6 μs is required (16 pixel per ADC at 10 MHz). In addition, a maximum time of 2 μs is required each before and after the readout for the load and the unload of the capacitors. Therefore the readout of, e.g., the two amplitude channels and the time information of an event causes a dead time of 8.8 μs *independent of the number of pixels in the camera*. However, this only takes into account the front-end of the camera – the time that is needed to write the digitised information over the network to the storage has to be considered as well. The comparison of these two dead times is done in section "Dead Time".

A.2 Testing the Prototype

Most components of the SPC were designed at the MPIK in Heidelberg, from electronics to supporting structure. The following results were received with the complete prototype with 128 pixels, which is the minimal configuration to test the interaction of all elements of the prototype. Figure A.4 shows a picture of the prototype.

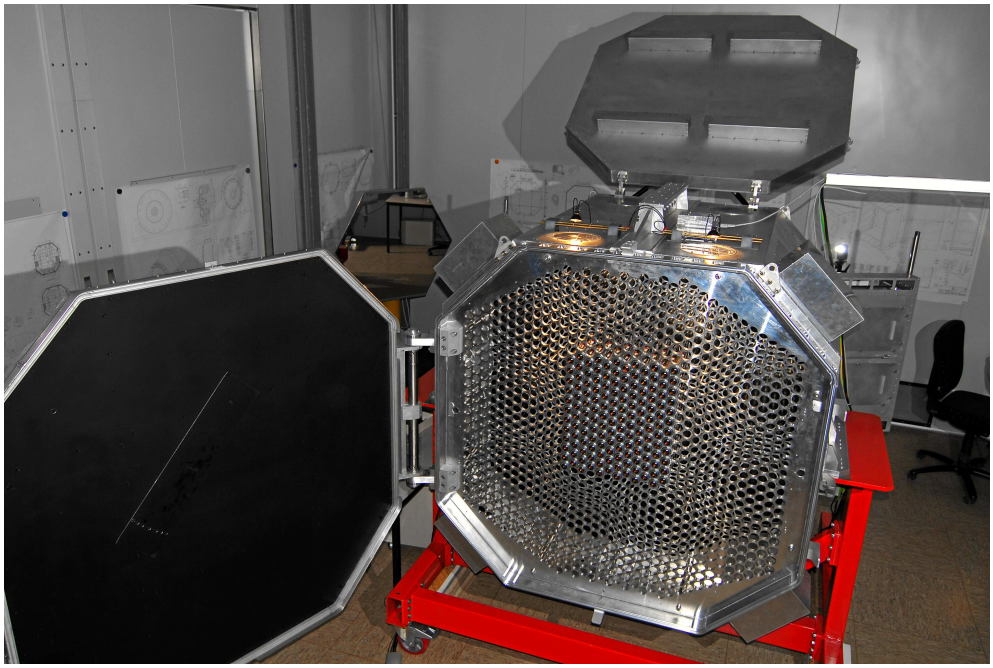

FIGURE A.4: The SPC prototype.

Amplitude

The amplitudes of the pixels detecting Cherenkov photons from the VHE γ-ray shower are used to reconstruct the energy and the original direction of the primary photon by comparing the camera pictures with Monte Carlo simulations (see Chapter 3.4). Therefore, a precise resolution of the amplitude measurement is crucial for a good resolution in the energy reconstruction.

Amplitude Calibration

The measurement of the charge content of the PMT signal (high gain) is calibrated using single photo electron spectra. These are amplitude distributions of events where on average one photo electron (p.e.) is emitted at the cathode of the PMT. At least two peaks in the single-p.e. spectrum have to be identified and fit: the pedestal peak, resulting from readout sequences where no p.e. was emitted (electronic noise), and the single-p.e. peak where exactly one p.e. was emitted. The number of ADC channels between the pedestal peak and the single-p.e. peak is the conversion factor from p.e. to ADC units. The width of the single-p.e. peak results from the combination of electronic noise and the Poisson distribution of the number of electrons in the amplification process in the PMT. Figure A.5 shows an example of a single-p.e. spectrum alongside with the fit used to obtain

the positions and widths of the pedestal and single-p.e. peak (solid line). As can be seen, the amplitude resolution of the Smart Pixel is perfectly suitable for the calibration with single-p.e. spectra.

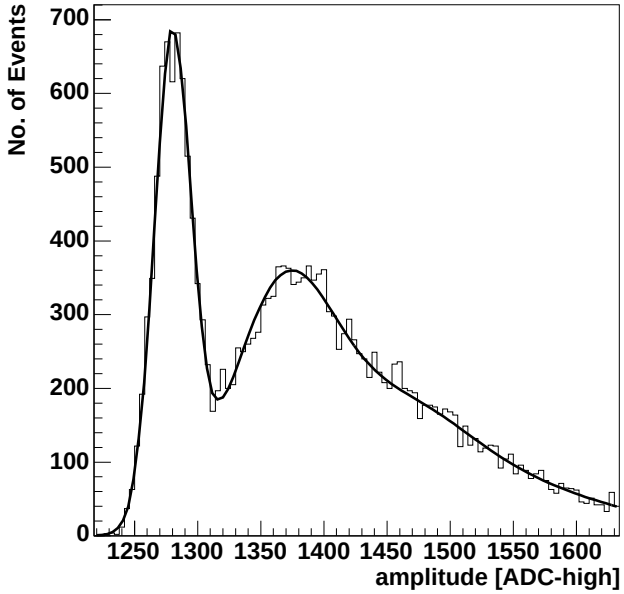

FIGURE A.5: Single-p.e. spectrum of a typical pixel. The first peak is the pedestal peak, resulting from electronic noise, and the second peak the single-p.e. peak, where exactly one p.e. was emitted. At an amplitude of ∼1500 ADC channels, an indication of a "shoulder" associated with the emission of exactly two p.e. can be seen.

Amplitude Resolution

Figure A.6 shows the measured relative resolution as a function of the amplitude in the high gain channel (black dots). The expectation from the Poisson distribution of the number of electrons in the amplification is drawn as a solid line. The resolution is slightly worse than expected, caused by the width of the single-p.e. peak (see above). Taking the width into account when calculating the expected resolution, the measured resolution matches the expectations (dashed line), showing that the amplitude measurement of the Smart Pixel reaches the best resolution possible using PMTs as photon detectors (with a given single-p.e. width).

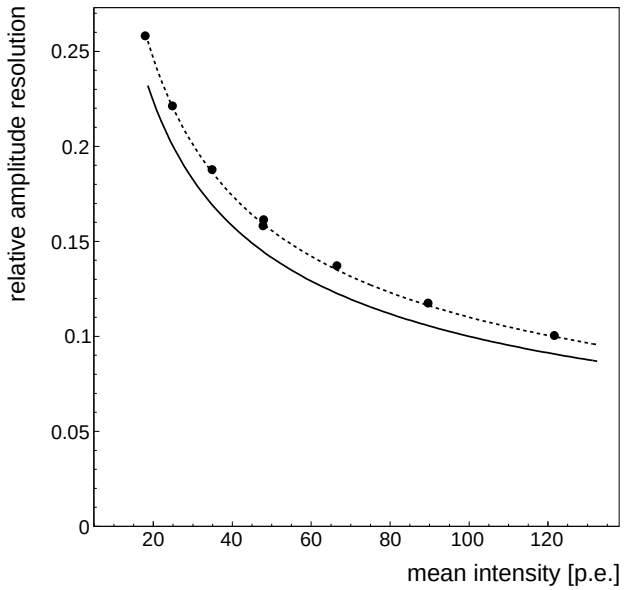

FIGURE A.6: Relative resolution of the high gain channel for different signal amplitudes. The black dots are the data points while the lines represent the expectation with (dashed) and without (solid) taking the width of the single-p.e. peak into account.

Noise

With increasing NSB the width of the pedestal peak of the single-p.e. spectrum increases. The NSB photons arrive statistically distributed in time (with a rate of $\sim$ 10^{12} $\mathrm{sr}^{-1}\,\mathrm{s}^{-1}\,\mathrm{m}^{-2}$) at the PMTs and contribute to the integration of the Cherenkov events. Therefore, measuring the pedestal width as a function of the p.e. rate gives an estimate of the gate width for photons from the NSB. The width (RMS) of the pedestal originates from statistical variations (Poisson statistics) in the number of p.e. emitted at the cathode, $RMS = \sqrt{N_{\mathrm{p.e.}}}$, while the gate is open for integration. For a given p.e. rate $r_{\mathrm{p.e.}}$ and a gate width of T, $N_{\mathrm{p.e.}}$ is $r_{\mathrm{p.e.}} \cdot T$ (assuming the NSB signals to be either completely in the gate or not at all).

In Figure A.7 the measured squared pedestal width is plotted as a function of the p.e. rate. The expected linear dependency can be seen. The slope of a linear fit to the points gives the integration gate for photons from the NSB. This estimation of the NSB gate width provides a method to cross-check the width of the programmed gate. Comparisons of the programmed gate widths to the measured NSB gate widths show a good agreement, which gives confidence that the integration is working as expected.

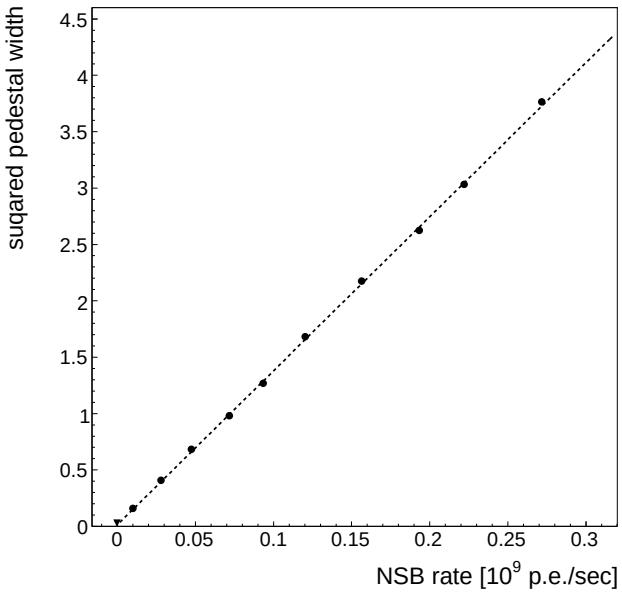

FIGURE A.7: Square of the pedestal width as a function of the number of p.e. emitted at the cathode per second for a programmed gate width of 19 ns. The measured gate width is the slope (∼18.4 ns).

Arrival Time Information

As the time window of Cherenkov light from an electromagnetic shower is approximately 5 ns, the time resolution of the SPC has to be in the sub-nanosecond regime to resolve the time distribution of the Cherenkov light.

The time measurement on the SPE is calibrated using a programmable delay (256 steps of each 2 ns) for the camera trigger, which is calibrated by using an oscilloscope. Figure A.8 shows the resolution of the time measurement as a function of the amplitude in the high gain channel for a typical pixel. It can be seen that the time resolution of the SPC is good enough to resolve the time gradient of shower pictures.

Trigger Performance

Pixel Threshold

The trigger threshold of each pixel must be well calibrated and a homogeneous trigger threshold over the whole camera is of great importance, as otherwise the response of the camera could be dominated by individual pixels. In the SPC this calibration is done by calibrating the threshold in every single pixel.

The calibration of the threshold can be done in normal operation mode. The

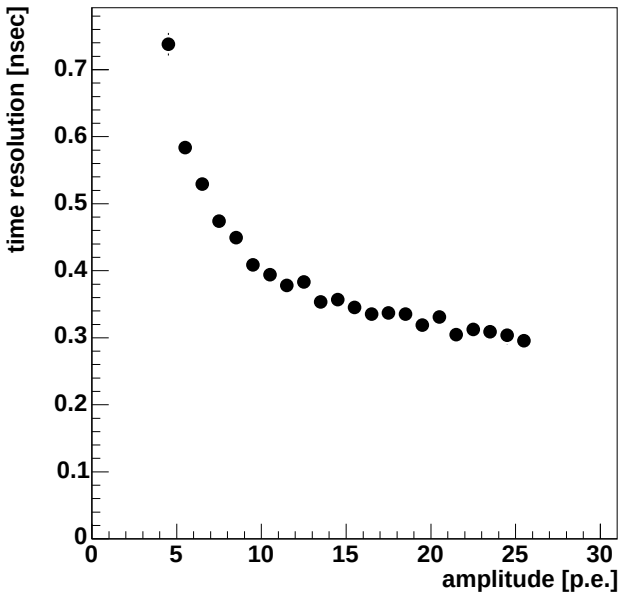

FIGURE A.8: Resolution of the arrival time measurement as a function of the amplitude in the high gain channel.

information needed is the amplitude of an arriving light pulse and if the pulse was above the discriminator threshold. The comparison of the amplitude distribution of all events to that of the events where the pixel discriminator generated a trigger signal allows the evaluation of the threshold. Figure A.9 shows the distribution of all events (dash-dotted line) in comparison with the events where the signal exceeded the threshold (solid line) in the main panel. The inset demonstrates how the threshold is determined. The ratio of the events where the pixel discriminator generated a trigger and the amplitude distribution of all events gives the shape of the threshold (see dashed fit). The threshold is defined as the amplitude where 50% of the events are registered by the pixel discriminator. The width of the threshold is defined as the difference in the amplitudes of 10% and 90% of the events causing a discriminator signal. For typical thresholds of $4-6$ p.e. the width is on the order of $1.0-1.5$ p.e., which is sufficient to guarantee a homogeneous trigger threshold over the whole camera.

Rate

The calibration of the rate measurement is realised with an event counter on the camera controller. For this, each pixel is separately activated for the generation of a discriminator signal and illuminated by an un-pulsed light source. The measured rate is compared to the number of trigger signals the pixel sent to

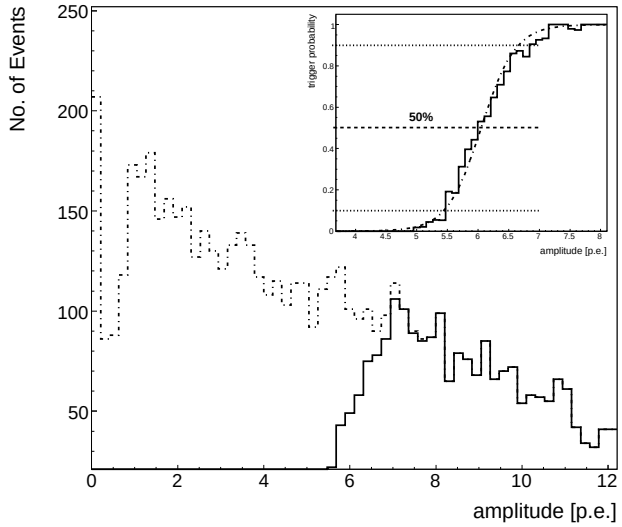

FIGURE A.9: *Main panel:* amplitude distribution of all events (dash-dotted line) and of events exceeding the pixel discriminator threshold (solid line). *Inset:* determination of the threshold. The ratio of the amplitude distribution of the events exceeding the pixel threshold and the amplitude distribution of all events is shown. By definition the threshold is the amplitude where 50% of the events generated a trigger (dash-dotted line). In addition, the 10% and the 90% level are plotted; these define the width of the threshold.

the camera trigger. This is done for different pixel thresholds and illumination strengths.

Calculated versus Measured Rate

Chance coincidences of NSB in neighbouring pixels produce disturbing triggers. Since coincidences of three of more neighbouring pixels are rather rare, only the case of a required coincidence of two pixels is discussed here. If the discriminator rates of two neighbouring pixels (r_i, r_j) and the chance coincidence window for the trigger generation ($T_{i,j}$) are known, the expected trigger rate for this pixel pair can be calculated to $R_{i,j} = r_i \cdot r_j \cdot T_{i,j}$. For the whole camera, the trigger rate due to chance coincidences is the sum of $R_{i,j}$ over all two pixel neighbour combinations (i, j). Therefore, the rate measurement on the pixels allows to calculate an estimate of the trigger rate originating from NSB. The difference between the calculated trigger rate and the trigger rate measured by counting the number of camera triggers per time for different discriminator thresholds is shown to be within a few percent down to a threshold of 4 p.e. This demonstrates that the trigger generation of the Smart Pixel works as expected.

Dead Time

To be able to write to disk already digitised data while digitising new data, the ADCs of the prototype are each equipped with two memory banks that can be accessed asynchronously. This leads to two different regimes for the dead time of the camera readout. For low rates, the dead time is dominated by the multiplexing and digitisation. At higher rates, the readout of the digitised data from the ADC (via the VME bus) dominates the dead time. To find an estimate of the expected dead time of an SPC with 1020 pixels, the dead time of the prototype with 128 pixels was measured and implemented in a simple dead-time model (see Glück (2006)). Figure A.10 shows the relative dead time as a function of the camera trigger rate. The two curves result from calculations for an SPC with 1020 pixels with one (dashed line, left) and two (dash-dotted line, right) VME systems. As can be seen, the use of two VME systems shifts the regime in which the dead time is dominated by the readout to higher rates. The solid line displays the dead time caused by the multiplexing and digitisation. At 5 kHz, a realistic rate for next-generation IACTs, the dead time is ∼4%.

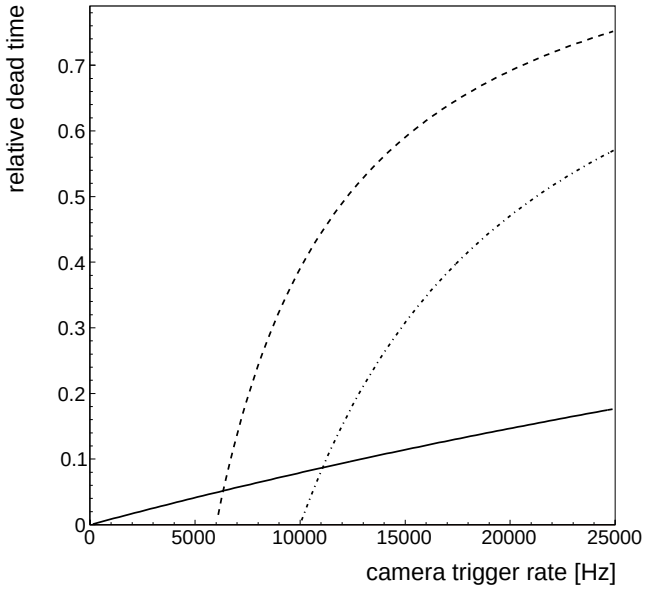

FIGURE A.10: Calculated relative dead time as a function of the trigger rate for an SPC with 1020 pixels (dashed line). In the case of two VME systems, the regime in which the dead time is dominated by the readout is shifted to higher rates (dash-dotted line). The dead time for the multiplexing and digitisation is shown as a solid line.

A.3 Summary

The SPC provides a fast readout and easy calibration methods, most of which – like the trigger threshold calibration – working during normal operation. The resolution of the signal integration is very good and all tests show that the signal integration on the pixel is well understood. The time resolution is sufficient to record time profiles of Cherenkov showers. An estimate of the relative dead time for a complete camera with 1020 pixels gives 4% at 5 kHz. The tests on the prototype of the SPC demonstrate that the SPC concept is appropriate for the next generation of IACT systems.

Bibliography

A. Achterberg, Y. A. Gallant, J. G. Kirk, and A. W. Guthmann. Particle acceleration by ultrarelativistic shocks: theory and simulations. *MNRAS*, 328: 393–408, December 2001.

F. A. Aharonian. *Very high energy cosmic gamma radiation : a crucial window on the extreme Universe*. River Edge, NJ: World Scientific Publishing, 2004.

F. A. Aharonian, A. M. Atoyan, and T. Kifune. Inverse Compton gamma radiation of faint synchrotron X-ray nebulae around pulsars. *MNRAS*, 291:162–176, October 1997.

F. Aharonian et al. The Crab Nebula and Pulsar between 500 GeV and 80 TeV: Observations with the HEGRA Stereoscopic Air Cerenkov Telescopes. *ApJ*, 614:897–913, October 2004a.

F. Aharonian et al. Energy dependent γ-ray morphology in the pulsar wind nebula HESS J1825-137. *Astronomy and Astrophysics*, 460:365–374, December 2006a.

F. Aharonian et al. Discovery of extended VHE gamma-ray emission from the asymmetric pulsar wind nebula in MSH 15-52 with HESS. *Astronomy and Astrophysics*, 435:L17–L20, May 2005a.

F. Aharonian et al. A detailed spectral and morphological study of the gamma-ray supernova remnant RX J1713.7-3946 with HESS. *Astronomy and Astrophysics*, 449:223–242, April 2006b.

F. Aharonian et al. Calibration of cameras of the H.E.S.S. detector. *Astroparticle Physics*, 22:109–125, November 2004b.

F. Aharonian et al. Observations of the Crab nebula with HESS. *Astronomy and Astrophysics*, 457:899–915, October 2006c.

F. Aharonian et al. Discovery of the two "wings" of the Kookaburra complex in VHE γ-rays with HESS. *Astronomy and Astrophysics*, 456:245–251, September 2006d.

F. Aharonian et al. A New Population of Very High Energy Gamma-Ray Sources in the Milky Way. *Science*, 307:1938–1942, March 2005b.

F. Aharonian et al. The H.E.S.S. Survey of the Inner Galaxy in Very High Energy Gamma Rays. *ApJ*, 636:777–797, January 2006e.

F. Aharonian et al. First detection of a VHE gamma-ray spectral maximum from a cosmic source: HESS discovery of the Vela X nebula. *Astronomy and Astrophysics*, 448:L43–L47, March 2006f.

F. A. Aharonian et al. A possible association of the new VHE γ-ray source HESS J1825 137 with the pulsar wind nebula G 18.0 0.7. *Astronomy and Astrophysics*, 442:L25–L29, November 2005c.

W. Baade and F. Zwicky. Cosmic Rays from Super-novae. *Proceedings of the National Academy of Science*, 20:259–263, 1934.

D. C. Backer, S. R. Kulkarni, C. Heiles, M. M. Davis, and W. M. Goss. A millisecond pulsar. *Nature*, 300:615–618, December 1982.

A. Bamba, M. Ueno, K. Koyama, and S. Yamauchi. Diffuse Hard X-Ray Sources Discovered with the ASCA Galactic Plane Survey. *ApJ*, 589:253–260, May 2003.

D. Berge. *PhD thesis*. PhD thesis, Ruperto-Carola University of Heidelberg, 2006.

D. Berge, S. Funk, and J. Hinton. Background modelling in very-high-energy γ-ray astronomy. *Astronomy and Astrophysics*, 466:1219–1229, May 2007.

J. M. Blondin, R. A. Chevalier, and D. M. Frierson. Pulsar Wind Nebulae in Evolved Supernova Remnants. *ApJ*, 563:806–815, December 2001.

O. Bolz. *PhD thesis*. PhD thesis, Ruperto-Carola University of Heidelberg, 2004.

H. Bradt et al. X-Ray and Optical Observations of the Pulsar NP 0532 in the Crab Nebula. *Nature*, 222:728, 1969.

C. L. Brogan, K. E. Devine, T. J. Lazio, N. E. Kassim, C. R. Tam, W. F. Brisken, K. K. Dyer, and M. S. E. Roberts. A Low-Frequency Survey of the Galactic Plane Near l=11 deg: Discovery of Three New Supernova Remnants. *AJ*, 127: 355–367, January 2004.

C. L. Brogan, J. D. Gelfand, B. M. Gaensler, N. E. Kassim, and T. J. W. Lazio. Discovery of 35 New Supernova Remnants in the Inner Galaxy. *ApJL*, 639: L25–L29, March 2006.

N. Bucciantini, J. M. Blondin, L. Del Zanna, and E. Amato. Spherically symmetric relativistic MHD simulations of pulsar wind nebulae in supernova remnants. *Astronomy and Astrophysics*, 405:617–626, July 2003.

K. S. Cheng, R. E. Taam, and W. Wang. Pulsar Wind Nebulae and the X-Ray Emission of Nonaccreting Neutron Stars. *ApJ*, 617:480–489, December 2004. doi: 10.1086/425295.

C. J. Clopper and E. S. Pearson. The use of the confidence or fiducial limits illustrated in the case of the binomial. *Biometrika*, 26:404–413, 1934.

W. J. Cocke, M. J. Disney, and D. J. Taylor. Discovery of Optical Signals from Pulsar NP 0532. *Nature*, 221:525, 1969.

J. M. Cordes and T. J. W. Lazio. NE2001.I. A New Model for the Galactic Distribution of Free Electrons and its Fluctuations. *ArXiv Astrophysics e-prints, astro-ph/0207156*, July 2002.

J. M. Davies and E. S. Cotton. . *Journal of Solar Energy*, 1:16–22, 1957.

E. Fermi. *Phys. Rev.*, 75:1169, 1949.

G. Fritz, R. C. Henry, J. F. Meekins, T. A. Chubb, and H. Friedman. X-ray Pulsar in the Crab Nebula. *Science*, 164:709–712, May 1969.

S. Funk. *PhD thesis*. PhD thesis, Ruperto-Carola University of Heidelberg, 2005.

S. Funk et al. The Trigger System of the H.E.S.S. Telescope Array. *Astroparticle Physics*, 22:285–296, November 2004.

B. M. Gaensler, J. Arons, V. M. Kaspi, M. J. Pivovaroff, N. Kawai, and K. Tamura. Chandra Imaging of the X-Ray Nebula Powered by Pulsar B1509-58. *ApJ*, 569:878–893, April 2002.

B. M. Gaensler, N. S. Schulz, V. M. Kaspi, M. J. Pivovaroff, and W. E. Becker. XMM-Newton Observations of PSR B1823-13: An Asymmetric Synchrotron Nebula around a Vela-like Pulsar. *ApJ*, 588:441–451, May 2003.

Bryan M. Gaensler and Patrick O. Slane. The evolution and structure of pulsar wind nebulae. *Annual Review of Astronomy and Astrophysics*, 44:17, 2006.

B. Glück. Test und Inbetriebnahme einer Kamera für Cherenkov Teleskope, 2006.

T. Gold. Rotating Neutron Stars as the Origin of the Pulsating Radio Sources. *Nature*, 218:731, 1968.

T. Gold. Rotating Neutron Stars and the Nature of Pulsars. *Nature*, 221:25, 1969.

P. Goldreich and W. H. Julian. Pulsar Electrodynamics. *ApJ*, 157:869, August 1969.

A. J. Green, L. E. Cram, M. I. Large, and T. Ye. The Molonglo Galactic Plane Survey. I. Overview and Images. *ApJS*, 122:207–219, May 1999.

D. A. Green. Galactic supernova remnants: an updated catalogue and some statistics. *Bulletin of the Astronomical Society of India*, 32:335–370, December 2004.

A. K. Harding. In *Gamma-ray Pulsars: Models and Predictions*, page 115, 2001.

D. Hauser et al. *Smart Pixel Camera for Imaging Atmospheric Cherenkov Telescopes*. In preparation, 2007.

W. Heitler. *Quantum theory of radiation*. International Series of Monographs on Physics, Oxford: Clarendon, 1954, 3rd ed., 1954.

D. J. Helfand, E. V. Gotthelf, and J. P. Halpern. Vela Pulsar and Its Synchrotron Nebula. *ApJ*, 556:380–391, July 2001.

D. J. Helfand, R. H. Becker, R. L. White, A. Fallon, and S. Tuttle. MAGPIS: A Multi-Array Galactic Plane Imaging Survey. *AJ*, 131:2525–2537, May 2006.

A. Hewish, S. J. Bell, J. D. Pilkington, P. F. Scott, and R. A. Collins. Observation of a Rapidly Pulsating Radio Source. *Nature*, 217:709, 1968.

A. M. Hillas. Cerenkov light images of EAS produced by primary gamma. In F. C. Jones, editor, *International Cosmic Ray Conference*, pages 445–448, August 1985.

A. M. Hillas et al. The Spectrum of TeV Gamma Rays from the Crab Nebula. *ApJ*, 503:744, August 1998.

J. A. Hinton. The status of the HESS project. *New Astronomy Review*, 48: 331–337, April 2004.

G. Hobbs et al. The Parkes multibeam pulsar survey - IV. Discovery of 180 pulsars and parameters for 281 previously known pulsars. *MNRAS*, 352:1439–1472, August 2004.

R. A. Hulse and J. H. Taylor. Discovery of a pulsar in a binary system. *ApJL*, 195:L51–L53, January 1975.

V. M. Kaspi, M. S. E. Roberts, and A. K. Harding. Isolated Neutron Stars. *ArXiv Astrophysics e-prints*, February 2004.

V. M. Kaspi et al. Chandra X-Ray Observations of G11.2-0.3: Implications for Pulsar Ages. *ApJ*, 560:371–377, October 2001.

K. Koyama et al. Discovery of Non-Thermal X-Rays from the Northwest Shell of the New SNR RX J1713.7-3946: The Second SN 1006? *PASJ*, 49:L7–L11, June 1997.

M. Kramer. Pulsars. In L. I. Gurvits, S. Frey, and S. Rawlings, editors, *EAS Publications Series*, volume 15 of *EAS Publications Series*, pages 219–241, 2005.

M. Kramer et al. The Proper Motion, Age, and Initial Spin Period of PSR J0538+2817 in S147. *ApJL*, 593:L31–L34, August 2003.

M. I. Large, A. E. Vaughan, and B. Y. Mills. A Pulsar Supernova Association? *Nature*, 220:340, 1968.

T.-P. Li and Y.-Q. Ma. Analysis methods for results in gamma-ray astronomy. *ApJ*, 272:317–324, September 1983.

Y. E. Lyubarsky. The termination shock in a striped pulsar wind. *MNRAS*, 345: 153–160, October 2003.

R. N. Manchester, G. B. Hobbs, A. Teoh, and M. Hobbs. The Australia Telescope National Facility Pulsar Catalogue. *AJ*, 129:1993–2006, April 2005.

R. N. Manchester et al. The Parkes multi-beam pulsar survey - I. Observing and data analysis systems, discovery and timing of 100 pulsars. *MNRAS*, 328: 17–35, November 2001.

C. B. Markwardt and H. Ogelman. An X-Ray Jet from the VELA Pulsar. *Nature*, 375:40, May 1995.

H. Muraishi et al. Evidence for TeV gamma-ray emission from the shell type SNR RX J1713.7-3946. *Astronomy and Astrophysics*, 354:L57–L61, February 2000.

G. Neugebauer et al. The Infrared Astronomical Satellite (IRAS) mission. *ApJL*, 278:L1–L6, March 1984.

C.-Y. Ng, M. S. E. Roberts, and R. W. Romani. Two Pulsar Wind Nebulae: Chandra/XMM-Newton Imaging of GeV J1417-6100. *ApJ*, 627:904–909, July 2005.

F. Pacini. Rotating Neutron Stars, Pulsars and Supernova Remnants. *Nature*, 219:145, 1968.

M. J. Rees and J. E. Gunn. The origin of the magnetic field and relativistic particles in the Crab Nebula. *MNRAS*, 167:1–12, April 1974.

S. P. Reynolds and R. A. Chevalier. Evolution of pulsar-driven supernova remnants. *ApJ*, 278:630–648, March 1984.

D. Sanwal, G. G. Pavlov, and G. P. Garmire. Chandra Observations of X-ray Tails Behind Pulsars. *Bulletin of the American Astronomical Society*, 37:497, May 2005.

D. H. Staelin and E. C. Reifenstein. Pulsating radio sources near the Crab Nebula. *Science*, 162:1481–1483, 1968.

T. Tanimori et al. Detection of Gamma Rays of up to 50 TeV from the Crab Nebula. *ApJL*, 492:L33, January 1998.

J. H. Taylor and J. M. Cordes. Pulsar distances and the galactic distribution of free electrons. *ApJ*, 411:674–684, July 1993.

E. Trussoni, S. Massaglia, S. Caucino, W. Brinkmann, and B. Aschenbach. ROSAT PSPC observations of the supernova remnant MSH 15-52. *Astronomy and Astrophysics*, 306:581, February 1996.

E. van der Swaluw, A. Achterberg, Y. A. Gallant, and G. Tóth. Pulsar wind nebulae in supernova remnants. Spherically symmetric hydrodynamical simulations. *Astronomy and Astrophysics*, 380:309–317, December 2001.

E. van der Swaluw, T. P. Downes, and R. Keegan. An evolutionary model for pulsar-driven supernova remnants. A hydrodynamical model. *Astronomy and Astrophysics*, 420:937–944, June 2004.

P. Vincent et al. Performance of the H.E.S.S. Cameras. In *International Cosmic Ray Conference*, page 2887, July 2003.

W. Voges, T. Boller, J. Englhauser, M. Freyberg, and R. Supper. The ROSAT X-ray Database from All-Sky Survey and Pointed Observations. In R. J. Brunner, S. G. Djorgovski, and A. S. Szalay, editors, *ASP Conf. Ser. 225: Virtual Observatories of the Future*, page 234, 2001.

Fridolin Weber. *Pulsars as Astrophysical Laboratories for Nuclear and Particle Physics*. Institute of Physics Publishing, London, 1999.

A. E. Wright, M. R. Griffith, B. F. Burke, and R. D. Ekers. The Parkes-MIT-NRAO (PMN) surveys. 2: Source catalog for the southern survey (delta greater than -87.5 deg and less than -37 deg). *ApJS*, 91:111–308, March 1994.

Danksagung

Hier möchte ich mich bei den vielen Menschen bedanken, die mich unterstützt haben und zum Gelingen dieser Arbeit beigetragen haben. Im Besonderen möchte ich mich bedanken bei:

* meinem Doktorvater Werner Hofmann dafür, daß er mir ermöglicht hat, bei H.E.S.S. mitzuarbeiten, Erfahrungen auf Konferenzen zu sammeln und vor allem für die interessante Aufgabenstellung. Ich habe in der Zusammenarbeit mit ihm viel gelernt.

* German Hermann für die Möglichkeit, an der Smart Pixel Kamera zu arbeiten und auch etwas "Handfestes" im Rahmen der Doktorarbeit zu tun. In diesem Zusammenhang möchte ich mich auch bei den Mitarbeitern der Mechanik- und Elektronikwerkstatt bedanken, mit denen die Zusammenarbeit viel Spaß gemacht hat, insbesondere bei Christian Föhr und Thomas Schwab.

* Thomas Lohse dafür, daß er das Koreferat übernommen hat, mir die wunderbare Welt der Statistik nähergebracht hat und für viele gute Gespräche.

* Christian Stegmann, der auszog mir beizubringen wie man Veröffentlichungen schreibt, dafür, daß er dies hartnäckig verfolgt hat, und für die vielen netten Telefonate.

* Olaf Reimer dafür, daß er mich mit seiner Begeisterung an Populationsstudien angesteckt hat und für seine ermunternden Emails aus dem immer sonnigen Kalifornien.

* Jim Hinton und Conor Masterson für all die vielen Diskussionen, Anregungen, Erklärungen und den Spaß dabei.

* Christopher van Eldik für die vielen Korrekturen, für die schwierigen Fragen, die ihm immer noch einfallen, und dafür, dass er letztendlich doch nie "Nein" sagen kann (obwohl er es versucht).

* Karl Kosack für die gemeinsame Arbeit und das Durchhalten am 2PWNe-Paper, für viele Diskussionen und seine wunderbaren Geburtstagsfeiern.

* Wystan Benbow für viele Erklärungen und für sehr gründliche und geduldige last-minute Korrekturen.

* der ganzen Heidelberger Gruppe für den Spaß bei der Arbeit, die Unterstützung und die Feiern, und ganz speziell
Kathrin Egberts, deren wunderbare Unterstützung mir in vielfacher Form zu teil wurde – nicht zuletzt in Form von Süßigkeiten.

* Dominik Hauser für seine Freundschaft und Unterstützung und vor allem für unser gemeinsames Durchhaltevermögen – ohne Dich hätte ich das alles nicht so viel Spaß gemacht, Mr. Thompson.

* meiner ganzen Familie dafür, daß sie mir das Gefühl geben, daß ich mit ihnen im Rücken alles schaffen kann. Oma möchte ich danken für nun schon beinahe 25 Jahre enthusiatischen Daumendrückens und meinen Eltern Hans und Barbara Klages dafür, daß ihr mich immer unterstützt und geliebt habt, auch wenn ich es euch manchmal sicher nicht einfach gemacht habe (siehe unten).

Finally I want to thank fate for bringing **Dan** into my life. Most definitely the best thing that ever happened to me.

WENN TÖCHTER MIST BAUEN